11-6-2014

Thermal Assessment of a Latent-Heat Energy Storage Module During Melting and Freezing for Solar Energy Applications

Antonio Miguel Ramos Archibold
University of South Florida, antonioramos@mail.usf.edu

Thermal Assessment of a Latent-Heat Energy Storage Module During Melting and Freezing for Solar Energy Applications

by

Antonio Ramos Archibold

A dissertation submitted in partial fulfillment
of the requirements for the degree of
Doctor of Philosophy
Department of Mechanical Engineering
College of Engineering
University of South Florida

Co-Major Professor: D. Yogi Goswami, Ph.D.
Co-Major Professor: Muhammad M. Rahman, Ph.D.
Elias Stefanakos, Ph.D.
Frank Pyrtle III, Ph.D.
Andres Tejada-Martinez, Ph.D.
José Gonzalez-Aguilar, Ph.D.

Date of Approval:
November 6, 2014

Keywords: Phase Change Material, Natural Convection, Radiant Energy, Spherical Capsule, Packed Bed Heat Exchangers

DEDICATION

Dedicated to my beloved wife Milena, wonderful daughters Paula, Mary and Natalia and admired parents Vicky (in loving memory) and Toño.

ACKNOWLEDGMENTS

The author would like to express his gratitude and most-sincere appreciation to professors Yogi Goswami, Muhammad Rahman and Elias Stefanakos, who supported and guided this investigation. However, most importantly the recognition for their integrity and critical way of thinking that has been an inspiration. Gratitude is also due to professors Frank Pyrtle, Andres Tejada-Martinez and Dr. José Gonzalez-Aguilar, who served on this advisory committee.

The author expresses his gratitude for the financial support received from the U.S. Department of Energy under the award numbers: DE-EE0003590 and DE-AR0000179, E.ON company and Universidad Autonoma del Caribe.

During the course of this research, the author has received tremendous support and help from the staff personnel and graduate students at the USF Clean Energy Research Center. Special gratitude to Mr. Charles Garretson (Chuck), Mrs. Barbara Graham, Philip, Mehdi, Jamie, Tanvir, Abhinav and Chatura.

Extremely valuable recognition is due to Drs. Ricardo Vasquez, Gokmen Demirkaya, Huijuan Chen and Chennan Li for their outstanding and high-level contributions during the early stages of this research.

The unconditional friendship and valuable support during every stage of this journey received from Saeb Besarati, Mario Juha and Ena Sierra, are gratefully acknowledged. Finally, the author wants to highlight all the patient, understanding, encouragement and support spontaneously received from his family (Milena, Paula, Mary, Natalia, Fabian, Shirley, Vicky (in loving memory) and Toño). Without them, this document would not be written.

TABLE OF CONTENTS

LIST OF TABLES

LIST OF FIGURES

ABSTRACT

Capital investment reduction, exergetic efficiency improvement and material compatibility issues have been identified as the primary techno-economic challenges associated, with the near-term development and deployment of thermal energy storage (TES) in commercial-scale concentrating solar power plants. Three TES techniques have gained attention in the solar energy research community as possible candidates to reduce the cost of solar-generated electricity, namely (1) sensible heat storage, (2) latent heat (tank filled with phase change materials (PCMs) or encapsulated PCMs packed in a vessel) and (3) thermochemical storage. Among these the PCM macro-encapsulation approach seems to be one of the most-promising methods because of its potential to develop more effective energy exchange, reduce the cost associated with the tank and increase the exergetic efficiency. However, the technological barriers to this approach arise from the encapsulation techniques used to create a durable capsule, as well as an assessment of the fundamental thermal energy transport mechanisms during the phase change.

A comprehensive study of the energy exchange interactions and induced fluid flow during melting and solidification of a confined storage medium is reported in this investigation from a theoretical perspective. Emphasis has been placed on the thermal characterization of a single constituent storage module rather than an entire storage system, in order to, precisely capture the energy exchange contributions of all the fundamental heat transfer mechanisms during the phase change processes. Two-dimensional, axisymmetric, transient equations for mass, momentum and energy conservation have been solved numerically by the finite volume scheme.

Initially, the interaction between conduction and natural convection energy transport modes, in the absence of thermal radiation, is investigated for solar power applications at temperatures ($300 - 400℃$). Later, participating thermal radiation within the storage medium has been included in order to extend the conventional natural convection-dominated model and to analyze its influence on the

melting and freezing dynamics at elevated temperatures ($800 - 850℃$). A parametric analysis has been performed in order to ascertain the effects of the controlling parameters on the melting/freezing rates and the total and radiative heat transfer rates at the inner surface of the shell. The results show that the presence of thermal radiation enhances the melting and solidification processes.

Finally, a simplified model of the packed bed heat exchanger with multiple spherical capsules filled with the storage medium and positioned in a vertical array inside a cylindrical container is analyzed and numerically solved. The influence of the inlet mass flow rate, inner shell surface emissivity and PCM attenuation coefficient on the melting dynamics of the PCM has been analyzed and quantified.

CHAPTER 1: INTRODUCTION

1.1. Discussion of the Problem

The urgent need of sustainable and clean energy sources to secure the future energy production as well as expand the existing electricity generation market has motivated the rapid growth of commercial-scale concentrating solar power (CSP) plants during recent years [1, 2, 3]. The potential integration of thermal energy storage (TES) in a CSP plant becomes extremely critical to dispatch power when solar irradiation is not available, allowing the plant to operate in a cost-effective fashion and consequently reduce the plant levelized electricity cost.

The current commercial TES option for CSP systems uses synthetic oil or molten nitrate salts as the storage media where energy is stored via sensible heat [4, 5]. In these systems, large amount of storage material is used and, therefore, large tanks are required, thus increasing the overall cost of the system. In addition to the economic drawback, technical barriers associated with the low exergetic efficiency and material compatibility issues for molten salts [6, 7] are key factors that necessitate the near-term development of advanced thermal energy storage concepts.

Numerous research and development initiatives have been directed towards single tank thermocline systems for sensible heat storage [8, 9, 10] in an effort to reduce the cost of the TES system; however the primary challenge is the temperature degradation within the system, which results in lower exergetic efficiency [6]. In that context, the use of phase change materials for latent heat energy storage is an excellent option, because of its high energy density which reduces the size of the storage tank, and its potential to increase the energy and exergy efficiency in conventional steam Rankine cycles [11, 12, 13].

Special attention has been devoted to develop low cost and industrially scalable encapsulation techniques to confine the PCMs in spherical or cylindrical capsules to be used in a packed bed or shell and tube heat exchangers [14, 15, 16, 17].

The technological barriers of this approach arise from (1) the material compatibilities between the PCM and the shell, as well as the shell and the heat transfer fluid (HTF), (2) the ability to produce durable capsules to withstand continuous thermal cycles at elevated temperatures, (3) the assessment of the fundamental thermal energy transport mechanisms during the phase change processes, (4) the low PCM thermal conductivity that limits the contribution of conduction, particularly during solidification [14, 15].

One of the challenging problems in thermal modeling of the storage tanks containing encapsulated PCMs, is the energy exchange process between the HTF and the PCM capsules, which is commonly modeled using an effective thermal conductivity or an overall heat transfer coefficient term in the energy equation [16, 17]. Depending on the accuracy of the model, this term may include heat transfer by forced convection between the HTF and the external surface of the shell, heat conduction through the shell wall and all the energy contributions within the PCM during the phase change process.

In general, the interaction of forced convection and shell conduction is estimated based on empirical correlations from the packed bed heat exchanger literature [18, 19] and the thermal resistance analysis. However, prediction of the energy interactions within the PCM are usually based on a pure conduction phase change model or pure natural convection correlations for enclosed fluids in the absence of phase change and thermal radiation. That may not accurately describe all the appropriate physics of the problem.

The objective of the present investigation is to develop and solve a comprehensive model that accurately predicts the melting and solidification processes of an encapsulated PCM in order to quantify and correlate the simultaneous contributions of all the fundamental energy transport modes.

1.2. Literature Survey

1.2.1. Melting of a Confined PCM by Conduction and Natural Convection

A number of studies have been reported in the literature associated with melting within spherical containers and can be classified based on the dominant heat transfer mechanism that drives the phase change process. A closed form analytical solution has been developed by Paterson [20], for the one-dimensional spherical melting problem, considering stagnant liquid phase, which means that, the transfer

of heat within the molten material is purely by conduction. A numerical solution of the aforementioned problem was presented by Grimado and Boley [21]. The absence of buoyancy induced natural convection in the melt layer and the assumption that the solid fraction of the PCM remains at the center of the sphere are the main drawbacks of this model.

Moore and Bayazitoglu [22] analyzed the unconstrained melting (vertical motion of the solid phase due to its higher density) of a low melting temperature PCM. The mathematical model was solved using a finite difference technique. Good agreement was found between the numerical results and the experimental data for Ste=0.05 and 0.1 with a maximum deviation of about 10 percent in the predicted interface position. Roy and Sengupta [23] examined the influence of gravity-induced convection in the melt of a PCM in a spherical enclosure and demonstrated the quasi-steady fluid flow in the upper part of the sphere. Bahrami [24] performed heat transfer experiments for the melting of a phase change medium in a Pyrex glass spherical capsule. The free expansion of the medium in the void space within the sphere was permitted. The PCM used in the study was 99% pure n-eicosane paraffin. The study concluded that the melting process was significantly affected by the movement of the solid toward the base of the sphere.

Fomin and Saitoh [25] presented numerical and analytical investigations of the melting process in a spherical capsule. N-octadecane was used as the PCM while an extension of the mathematical approach developed by Bareiss and Beer [26] was used to set up the numerical model. A sinusoidal temperature profile was employed as the boundary condition. The approximate analytical solution was found to be in good agreement with the numerical results. The discrepancy in the results was within 15%.

Khodadadi and Zhang [27] demonstrated that melting in the upper part of a PCM sphere is much faster than in the lower part due to buoyancy induced convection. They also noted that conduction is predominant only during the early melting process and highlighted the use of Rayleigh number to characterize convection in this problem. Regin et al. [28] analyzed numerically and experimentally the heat transfer inside a spherical capsule placed in a convective environment. A conduction-dominated mathematical model with an effective conductivity for the PCM that accounts for the natural convection effect was used for the numerical calculations.

The study concluded that the Stefan number and the radius of the capsule have significant effects on the total melting time.

Assis et al. [29] reported numerical and experimental analyses of melting in an open spherical enclosure. A combined PCM-air system was analyzed with the air space in the upper part of the shell to account for the volume expansion during the phase change process. The model took into account the density difference between the solid and liquid PCM, natural convection in the molten PCM and the air, and the vertical motion of the solid PCM. Observations from the numerical model were validated through experiments using a low melting point wax in a glass container, submerged in a water bath. The Nusselt number and melt fraction results were presented as a function of the Fourier, Stefan, and Grashof numbers.

Tan [30] reported an experimental comparison between the constrained and unconstrained melting processes of n-octadecane inside a glass container. Later, Tan et al. [31] performed numerical simulations and experiments on a vertically constrained paraffin wax sphere. They confirmed the quasi-steady behavior of the upper part of the sphere while observing the unstable melting pattern of the bottom of the sphere. In this region, a convective rising hot "jet" is reported as well as a chaotic convective behavior. The authors highlighted an underestimation of waviness at the bottom part of the sphere during experiments. They concluded that the influence of the support structure used to constrain the PCM is non-negligible. Hosseinizadeh et al. [32] reported a numerical investigation of melting of nano-enhanced phase change material in a spherical container.

The effect of different nano-particle volume fractions (0, 0.02 and 0.04) on the melting rate was analyzed. The computational domain was defined similar to that developed by Assis et al. [29]. Simulation results show a melting rate enhancement of the nano-enhanced phase change materials with respect to the conventional PCM due to higher thermal conductivity. A transient two-dimensional analysis of heat transfer during the melting process of encapsulated sodium nitrate in stainless steel cylindrical capsules has been reported by Zhao et al. [33].

Saitoh et al. [34, 35] analyzed the natural convection-dominated melting in a spherical capsule for n-octadecane and water, numerically and experimentally. The mathematical model was solved by a finite difference method employing the boundary fixing method to solve the motion of the solid-liquid interface. Hosseinizadeh et al. [36] presented a numerical analysis on the melting process of n-octadecane in an open spherical glass container. A uniform temperature boundary condition was imposed at the outer wall of the shell. The Computational findings were validated with the experimental results reported by Tan [30]. Good agreement was found between the numerically predicted results and the experimental data for the case where the solid phase motion was not restricted. Rizan et al. [37] reported an experimental investigation of n-octadecane melting inside a spherical shell subjected to a uniform heat flux at the outer surface of the shell. In this study, the effect of Stefan number on the melt fraction rate is highlighted.

The melting of Sodium Nitrate ($NaNO_3$) in a square cavity has been explored numerically by Wang et al [38] and a benchmark solution for the case of $Ra = 10^8$ and $Ste = 0.1$ has been presented. An alternate TES approach based on heat pipe technology has been proposed by Shabgard et al. [39] using KNO_3 as PCM. A thermal network model was used to predict the transient response of the system. Two different configurations were analyzed and the influence of the orientation on the thermal response of the system was evaluated.

In addition, a number of experimental and analytical investigations have been performed on heat transfer and buoyancy driven flow during melting of ice spheres. However, since the dynamics of the phase change process in ice is opposite in trend to most of the PCMs that are suitable for solar energy applications, a detailed description of these studies will not be included here. More information can be found in Dumore et al. [40], Vanier and Tien [41] and Hao and Tao [42].

1.2.2. Melting of a Confined PCM by Conduction and Radiation

The problem of heat transfer by radiation in a gray medium confined between two concentric black spheres has been widely reported in the heat transfer literature. A simplified analytical method, based on the diffusion approximation, for calculating radiation heat transfer in the aforementioned system has been presented by Konakov [43].

Sparrow et al. [44] have discussed the contribution of the absorption coefficient and the size of the container on the medium temperature distribution. In the model, an absorbing-emitting, gray gas was assumed as the participating medium while uniform and equal temperatures were imposed at the shell surfaces. A uniform internal heat generation rate per unit volume through the gas was also considered. Numerical predictions were reported, and the study concluded that the gas temperature variations are greater when the absorption coefficient increases for a fixed geometry.

An approximate solution of the previously described problem has been reported by Dennar and Sibulkin [45] and Chou and Tien [46] based on an extension of the Milne-Eddington approximation (moment method) originally developed for plane layers. Tong and Swathi [47] evaluated the accuracy of the spherical harmonic numerical method by solving the same problem. In their model, scattering of radiation within the medium was considered, and the influence of the differential approximation technique on the wall heat fluxes was presented.

Ryhming [48], Viskanta and Crosbie [49]. and Jia et al. [50] extended the analysis of Sparrow et al. [44] to include a uniform but different temperature at the bounded surfaces. It should be mentioned that in the results reported by [48] three values of the inner to outer wall temperature ratios T_1/T_2= 2, 5 and 25 were reported.

Viskanta and Merriam [51] performed a parametric investigation on the steady state conduction and radiation heating and cooling processes of an absorbing, emitting, scattering and gray medium enclosed in the space between two black, isothermal and concentric spheres. The influences of the Planck number, optical thickness, surface emissivities, inner to outer radius ratio, internal heat generation per unit volume and inner to outer wall temperature ratios were investigated. The study highlighted the strong influence of the surface emissivities on the local radiation heat transfer flux and reported an increase of the total heat flux at the inner surface of the system when the Planck number and the optical thickness decreases and increases respectively. The transient solution of the model reported by [51] has been obtained by Chu and Weng [52]. In their study, the equation of radiative transfer was numerically solved by the spherical harmonic method.

The transient cooling process of a stationary spherical gas mass by radiation was analyzed by Viskanta and Lall [53]. The energy transfer by conduction and convection was neglected, and a numerical solution of the energy equation was obtained by the method of moments. The effect of optical thickness of the gas on the local heat flux and temperature distribution was presented.

The Galerkin method was used by Thynell and Özisik [54] to solve the steady state condition of the problem reported by [53]. Tsai and Özisik [55] analyzed the transient combined conduction and radiation problem in an absorbing, emitting and isotropically scattering solid sphere subjected to a uniform temperature at the black boundary surface. The effects of the single scattering albedo and the radiation to conduction parameter on the temperature distribution and heat fluxes have been discussed.

Siewert and Thomas [56] reported a steady state solution of the problem formulated by [55]. In their study, a mathematical model was reduced based on a sphere to plane transformation technique, and the spherical harmonics method was employed to solve the reduced system numerically. Bayazitoglu and Suryanarayana [57] numerically analyzed the influence of the Planck number and the optical thickness on the transient cooling process of a solid sphere surrounded by a gray, emitting, absorbing and isotropically scattering gas. Thynell [58] considered the influence of anisotropic scattering on the combined conduction and radiation heat transfer on a spherical medium. Reported studies on the influence of thermal radiation in non-opaque media during phase change processes have been largely limited to the treatment of solidification in planar systems [59, 60, 61], because of its simplicity and the fact that the contribution of natural convection can be justifiably ignored in this process [62, 63].

1.2.3. Solidification of a Confined PCM by Conduction

An extensive literature review of the reported solutions of the PCM solidification problem reveals that the most commonly analyzed model assumes that the medium is initially at the phase change temperature. Therefore, no heat transfer is allowed across the liquid phase, and the heat only flows in the solid portion. This simplified model is known as the single phase Stefan problem. Closed-form, semi-analytical solutions of this problem were presented by a number of investigators [64, 65, 66, 67, 68, 69, 70, 71] based on the similarity variable approach, asymptotic theory and parameter-perturbation methods.

Tao [72] reported a numerical solution of the single phase Stefan problem. The formulation in which the presence of temperature gradients across the liquid phase is considered, has been termed the two phase Stefan problem and has been experimentally and numerically analyzed, during freezing in vertical tubes, by Sparrow and Broadbent [73] and Sparrow and Ohkubo [74] respectively. These studies conclude that an initial superheating of the liquid moderately diminishes the frozen mass and the associated latent energy extraction at small times, but has a small effect on these quantities at large times. Also good agreement was found between the numerical predictions and the experimental results.

An extension of the single phase Stefan problem has been presented by McCue et al. [75]. In their model the initial temperature of the system was above the phase change temperature. However, only heat conduction was taken into account through the liquid phase. The study concludes that for small Stefan number conditions, the temperature within the inner liquid phase rapidly decreases to the phase change temperature. Consequently, heat conduction within the liquid does not affect the solidification process.

Ismail and Henriquez [76] performed a parametric analysis on the single phase Stefan problem for water confined in a spherical shell. They discussed the influence of the capsule size, shell material, shell thickness and outer surface boundary condition on the PCM solidification rate. The study concludes that an increase of the Biot number at the external surface of the shell decreases the solidification time.

Freezing experiments of n-hexadecane encapsulated in spherical shells have been reported by Chan and Tan [77]. The evolution of the solidification phase via visualization front is presented for different outer surface and initial temperatures. Their study concludes that the solidification phase front progresses concentrically inwards from the colder outer surface of the sphere. Regin et al. [78] presented a numerical analysis of the solidification process of paraffin wax within a horizontal cylindrical capsule externally heated by a convection boundary condition.

The influence of the PCM volume reduction during solidification in a partially filled spherical shell has been studied by Assis et al. [79]. In their model, the domain was initially partially filled with liquid paraffin wax, with air in the remaining volume. Numerical results and experimental observations show that an upper void space is created inside the capsule due to PCM volume reduction during freezing.

The study also concludes that natural convection heat transfer in the liquid phase is negligible for Stefan numbers below 1. Diffusion-controlled freezing of a micro encapsulated PCM has been analyzed by Yang and Zhao [80].

The influence of thermal radiation on the single phase Stefan problem for non-opaque media have been largely limited to planar systems [81, 82, 83, 84] while the problem in the spherical media has received little attention; especially when all the fundamental heat transfer modes are simultaneously present.

1.2.4. Objective and Scope

As presented in the literature review, the available solutions for the phase change problem do not fully reflect the physical reality or may not be fully applicable to thermal energy storage in concentrating solar power plants. In this context, the primary objective of this study is to investigate the simultaneous interaction of all the fundamental energy transport modes during the melting and freezing of a phase change material confined in spherical and cylindrical shells.

The main differentiating aspects of this investigation with the previously reported studies include: (a) more realistic and detailed physical representation of the encapsulated cell considering a closed capsule and the simultaneous interaction of conduction, natural convection and participating thermal radiation, (b) analysis of the capsule internal pressure variation due to volumetric expansion during the phase change process, (c) development of correlations between heat transfer and melting fraction with dimensionless numbers at relatively high melting temperatures, (d) analysis of a simplified PCM encapsulated packed bed latent heat storage system that accounts for all the fundamental heat transfer modes within the capsule and includes a time and position dependent heat transfer coefficient and free stream temperature as a boundary condition at the outer shell wall.

Except for the studies reported by [85, 86] for the multi-mode heat transfer during melting in a square and a rectangular cavity respectively, no similar work has been reported in this field especially in curved media.

The primary motivation of this investigation is to provide additional information about the key elements in any phase change problem, i.e., solid-liquid interface position and phase distribution at a given time after the application of a thermal driving force, particularly under operating thermal conditions related to thermal energy storage for concentrating solar power plants.

The following specific tasks have been performed in order to accomplish the objectives of this study:

- Development of an analytical model capable of predicting simultaneous conduction and natural convection during melting of Sodium Nitrate confined in a spherical capsule. Two different solid PCM distributions inside the container have been investigated in this task for completely and partially filled capsule configurations. In the completely filled configuration, the solid storage material initially occupies all the capsule volume while, in the partially filled model, 90% of the capsule volume is initially filled with the solid PCM and the remaining volume is occupied by air. Schematics of the considered physical situations at the initial state are presented in Figure 1a and 1b. Effects of the main controlling parameters on the thermal performance of the capsules of various diameters (20, 30, 40 and 50 mm) are investigated, and the results are presented in chapter 2.

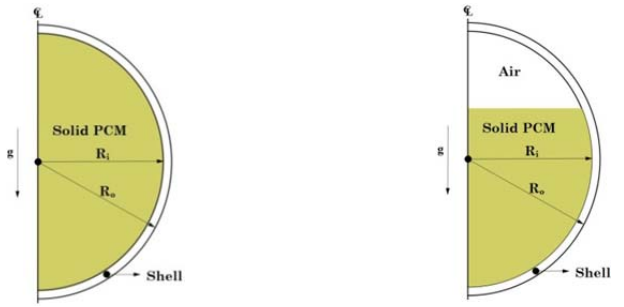

a) Completely filled capsule b) Partially filled capsule.

Figure 1 Schematic of the analyzed configurations

- Extension of the aforementioned mathematical model to include thermal radiation within the PCM during the solidification process of Sodium Nitrate.

Chapter 3 presents the results of the influence of simultaneous conduction, convection and thermal radiation on the freezing dynamics of a non-opaque media, with spectral dependence on its optical properties, encapsulated in a closed spherical shell at relatively high temperatures, in order to estimate the induced error in the solutions where participating thermal radiation within the PCM has been neglected.

- Development of a numerical methodology for predicting the energy exchange process during melting of Sodium Chloride encapsulated in a spherical capsule at elevated temperatures with enhanced radiative properties. It is presumed that at higher operating temperatures ($> 800°C$) radiative heat transfer becomes significant when compared to the other fundamental heat transfer modes. Consequently, the low thermal conductivity problem that penalizes the conduction energy transport during the melting and solidification processes can be overcome, particularly for transparent PCMs, by seeding the PCM with appropriate amounts of radiation absorbers. In this approach, an infra-red transparent PCM with tailored absorptance for enhanced radiative transfer is encapsulated in a spherical shell with a highly emissive coating on the inner surface. The results of a comprehensive parametric analysis are presented in Chapter 4.
- Development of a simplified model of the packed bed heat exchanger capable of predicting simultaneous energy exchange during melting of a non-opaque media in multiple spherical capsules positioned in a vertical array inside a cylindrical container. This model is an extension of the single capsule configuration presented in the previous chapters and also presents a valuable additional contribution to the knowledge of thermal modelling of packed bed heat exchangers. Chapter 5 presents the results of this simplified model.

Finally, conclusions about the study are summarized, and recommendations for further study in this area are also suggested in Chapter 6.

CHAPTER 2[1]: MELTING OF SODIUM NITRATE IN A SPHERICAL SHELL

In this chapter, a numerical model has been developed to simulate the heat transfer and fluid dynamics during the melting of sodium nitrate encapsulated in a metallic spherical shell and subjected to a constant temperature boundary condition at the outer wall of the shell. Although this chapter primarily focuses on $NaNO_3$, with a melting point of 306.8 ºC, the proposed numerical model will be extended in later chapters to predict the melting process of other PCMs with different encapsulation materials and under different boundary conditions.

2.1. Physical Situation and Mathematical Model Completely Filled Model

The considered system is schematically shown in a cross-sectional view in Figure 1a and consists of a spherical shell of inner and outer radius R_i and R_o respectively, under the gravitational field, which initially is completely filled with solid PCM at constant temperature T_o. For time t>0, a uniform temperature (T_w), which is greater than the melting temperature of the PCM (T_m), is imposed at the outer surface of the shell. The following assumptions are considered: (1) the PCM is continuous, homogeneous and isotropic; (2) the PCM liquid phase is a viscous Newtonian fluid; (3) the flow is laminar, has no viscous dissipation and can be modeled as axisymmetric; (4) the whole system is initially sub-cooled at 790.7℃ ; (5) the melting of $NaNO_3$ takes place in the interval between 306.3℃ and 306.8℃, where the density in this interval varies linearly from 2130 kg/m^3 at 306.3℃ to 1908 kg/m^3 at 306.8℃, (6) in this study the PCM volumetric expansion due to melting has been neglected for simplicity, even though it is well known that the PCM volume changes can exceed 22% in response to the density variations during the phase change process. A rigorous model of the problem may consider a spherical capsule that is partially filled with solid PCM while the remaining volume is occupied by air, (7) the thermal expansion

[1] The content of sections 2.1 to 2.4 was published in: A. R. Archibold, M. M. Rahman, D. Y. Goswami and E. K. Stefanakos, "Analysis of heat transfer and fluid flow during melting inside a spherical container for thermal energy storage," Applied Thermal Engineering, vol. 64, pp. 396-407, 2014. Permission is included in Appendix B.

of the shell material induced by the temperature differences has been neglected. According to [87], under the analyzed operating conditions the shell material experiences a volume change of 1.87%. The PCM thermo-physical properties [88, 89, 90, 91] used to estimate the dimensionless groups were calculated based on the reference temperature ($\bar{T}$) and are presented in the appendix. The wall thickness used in all the study cases was 0.5mm. Even though this chapter is mainly directed to evaluate the melting dynamics of Sodium Nitrate, another PCM (Rubitherm GmbH, RT27) has been included in the analysis for comparison purposes. The thermo-physical properties of the RT27 have been taken from [29]. Given the above assumptions, the conservation equations for mass, linear momentum and energy within the domain have been used to formulate this problem. The governing equations then become:

Continuity equation:

$$\frac{\partial \rho}{\partial t} + \frac{1}{r^2}\frac{\partial}{\partial r}(\rho v_r r^2) + \frac{1}{r sin\theta}\frac{\partial}{\partial \theta}(\rho v_\theta sin\theta) = 0 \tag{1}$$

Momentum equations in the radial and polar directions:

$$\rho\left(\frac{\partial v_r}{\partial t} + v_r\frac{\partial v_r}{\partial r} + \frac{v_\theta}{r}\frac{\partial v_r}{\partial \theta} - \frac{v_\theta^2}{r}\right) = -\frac{\partial P}{\partial r}$$

$$+\eta\left[\nabla^2 v_r - \frac{2v_r}{r^2} - \frac{2}{r^2 sin\theta}\frac{\partial(v_\theta sin\theta)}{\partial \theta} - \frac{2v_\theta cot\theta}{r^2}\right] - \rho g_r \beta(T - T_m) \tag{2}$$

$$\rho\left(\frac{\partial v_\theta}{\partial t} + v_r\frac{\partial v_\theta}{\partial r} + \frac{v_\theta}{r}\frac{\partial v_\theta}{\partial \theta} + \frac{v_r v_\theta}{r}\right) = -\frac{1}{r}\frac{\partial P}{\partial r} + \eta\left[\nabla^2 v_\theta + \frac{2}{r^2}\frac{\partial v_r}{\partial \theta} - \frac{v_\theta}{r^2 sin^2\theta}\right] - \rho g_\theta \beta(T - T_m) \tag{3}$$

where, ∇ is the Laplace operator and is defined as:

$$\nabla^2 = \frac{1}{r^2}\frac{\partial}{\partial r}\left(r^2\frac{\partial}{\partial r}\right) + \frac{1}{r^2 sin\theta}\frac{\partial}{\partial \theta}\left(sin\theta\frac{\partial}{\partial \theta}\right) \tag{4}$$

Energy equation:

$$\frac{\partial h}{\partial t} + \frac{1}{r^2}\frac{\partial}{\partial r}(r^2 v_r h) + \frac{1}{r sin\theta}\frac{\partial}{\partial \theta}(v_\theta sin\theta h) = \alpha\nabla^2 h$$

$$-\frac{1}{\rho c_p}\left(\frac{\partial \lambda}{\partial t} + \frac{1}{r^2}\frac{\partial}{\partial r}(r^2 v_r \lambda) + \frac{1}{r sin\theta}\frac{\partial}{\partial \theta}(v_\theta sin\theta\lambda)\right) \tag{5}$$

where h is the sensible enthalpy and λ the latent heat.

$$h = h_{ref} + \int_{T_{ref}}^{T} c_p dT \tag{6}$$

Here h_{ref} and T_{ref} are the reference sensible heat and temperature, respectively. The enthalpy-porosity technique, originally introduced by Voller and Prakash [92] and Brent et al. [93] was used to track the liquid-solid interface. In this method, the motion of the interface is not explicitly tracked. Instead it is determined via a linear relationship between the latent heat and the temperature, i.e., $\lambda = \phi L$ where (ϕ) is the liquid volume fraction of the computational cell where phase change is occurring $(0 < \lambda < L)$ and (L) is the latent heat of fusion. Liquid fraction is defined based on the following relations:

$$\begin{cases} \phi = 0; & T < T_s \\ \phi = \dfrac{T - T_s}{T_m - T_s}; & T_s < T < T_m \\ \phi = 1; & T > T_l \end{cases} \tag{7}$$

The aforementioned methodology introduces a damping term in each of the momentum equations in order to inhibit the velocity value arising from those equations on the solid phase. A Darcy damping term is used and is defined as:

$$S = C \frac{(1-\phi)^2}{(\phi^3 - \epsilon)} v_i \tag{8}$$

where i stands for the direction of the velocity components. In this study, v_r or v_θ depending on the case. ϵ is a small computational constant used to avoid division by zero $\epsilon = 0.001$. And C is a constant reflecting the morphology of the melt interface. In the present study a value of $C = 10^4\ kg/m^3\ s$ has been used.

2.2. Computational Procedure Completely Filled Model

The control volume technique was used to solve the governing equations in the system. An implicit scheme based on the SIMPLE (Semi-Implicit Method for Pressure-Linked Equations) algorithm proposed by Patankar [94], was employed to treat the coupling between pressure and momentum. A second order upwind scheme was employed to discretize the momentum equations while the PRESTO

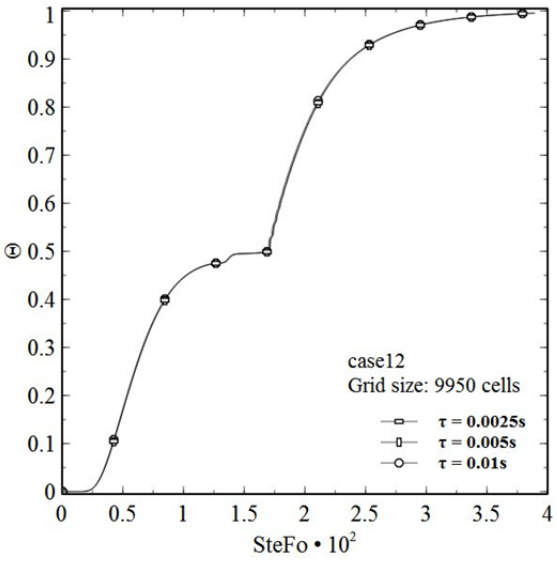

Figure 2 Time step influence on the center point dimensionless temperature for case 12

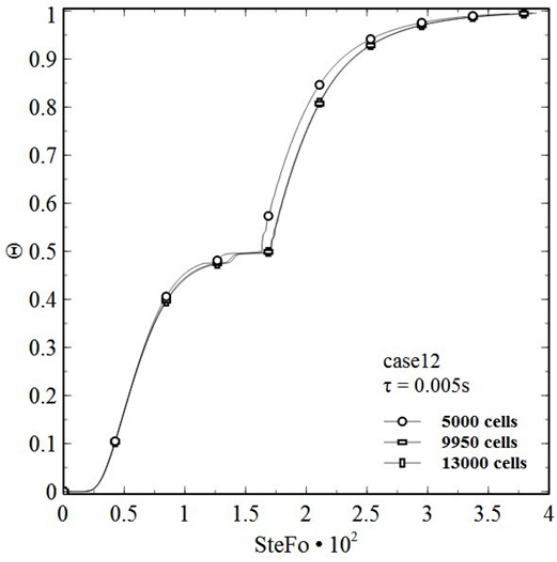

Figure 3 Grid size influence on the center point dimensionless temperature for case 12

(Pressure Staggering Option) scheme was adopted for pressure correction via the continuity equation. The under relaxation factors for pressure, momentum and energy were 0.3, 0.7, and 1.0, respectively. The solution of the problem has been checked for convergence at each time step.

Scaled absolute residuals of 10^{-4}, 10^{-3} and 10^{-6} were set as the convergence criteria for continuity, velocity components and energy, respectively. The number of iterations needed to achieve convergence varied between 10 and 20 for each time step. In order to provide a better resolution of the temperature and velocity gradient in the domain, and to capture the direct contact melting at the bottom of the container without any fictitious circulation flow in that region, a structured grid consisting of 9950 quadrilateral cells was used. Attention was paid to the grid parameters like maximum cell aspect ratio, cell orthogonal quality and cell skewness. The grid size and time step independence of the solution based on the melt fraction rate and the dimensionless temperature history at the center point were evaluated by using different grid densities and time steps. Figure 2 shows the dimensionless temperature history at the center point for a grid distribution with 9950 elements at different time step values. It can be observed that the predicted results are independent of the time step variations within the illustrated range. Based on that observation, the time step for all the calculations was set to 0.005sec.

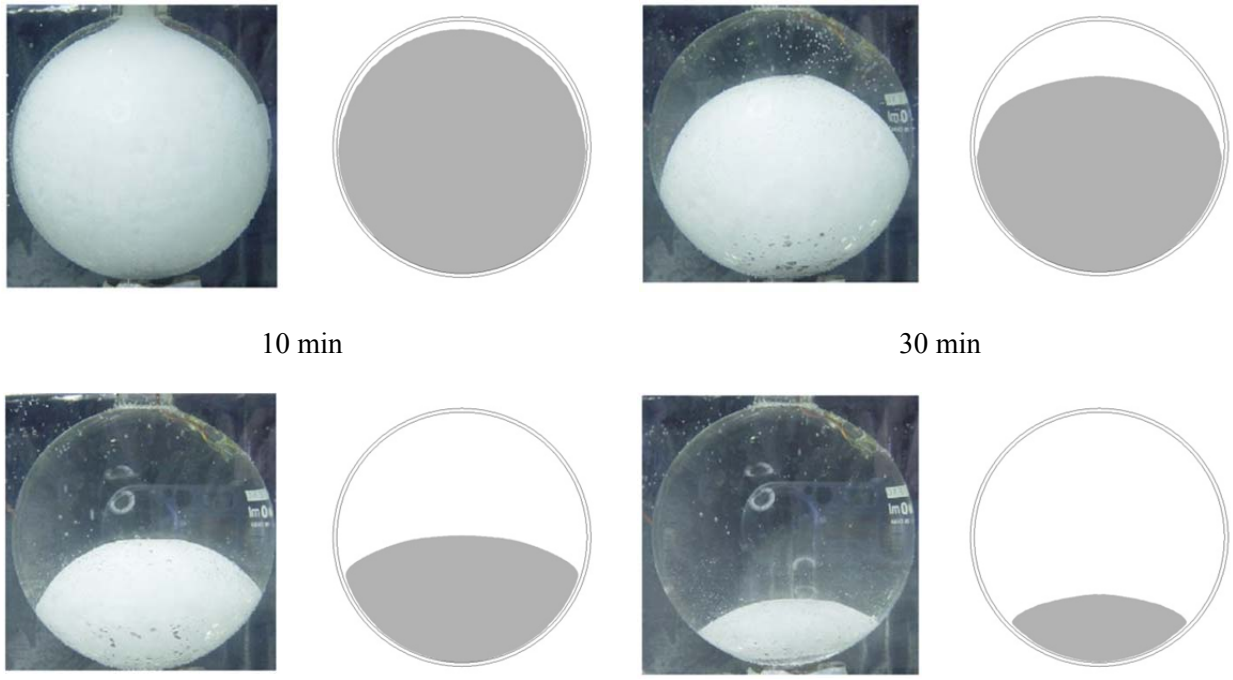

10 min 30 min

50 min 70 min

Figure 4 Experimental results of Tan [30] and numerical predictions of this study

The grid independence of the solution has been checked, and Figure 3 also presents the dimensionless temperature history at the center point for different grid sizes using the same time step value (0.005 sec). A slightly faster behavior is observed in the case with 5000 elements as compared to the case with 9950 and 13000 cells. Consequently, the grid size used to solve all the cases was 9950 cells. Experimental results reported by Tan [30] have been used to validate the developed numerical model. In the experiments, the melting process of n-octadecane inside a spherical glass capsule was visualized and reported. The spherical container of 50.83mm inner radius and 1.5mm wall thickness was initially maintained 1°C below the PCM melting temperature (28°C) and, for time t>0 the outer surface of the sphere was kept at 40°C. The solid fraction evolution for both experimental and numerical results obtained from our simulations for the same problem is shown in Figure 4. The numerically predicted melt fraction rate shows reasonably good agreement when compared to the results obtained in the experiments. Also, a quantitative comparison between the numerical prediction and the experimental measurements of

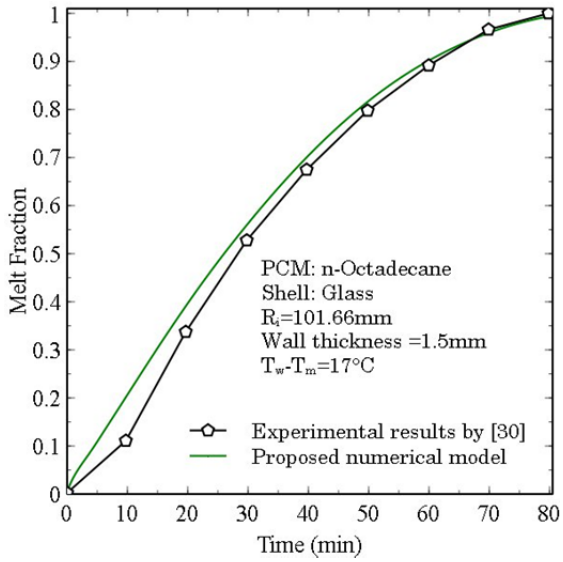

Figure 5 Melt fraction rate comparison

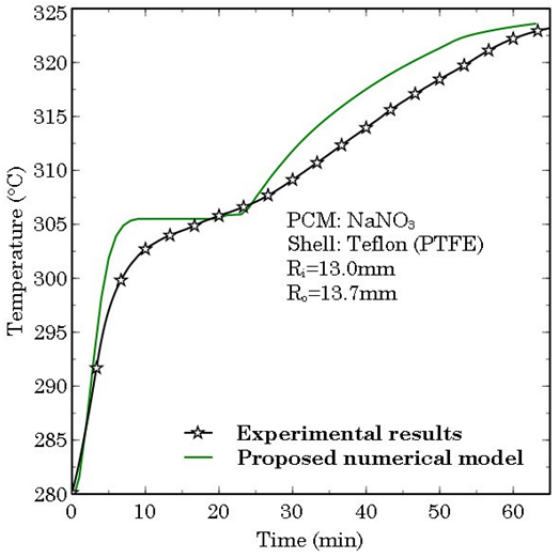

Figure 6 Capsule center point temperature history

the melt fraction rate is presented in Figure 5. Reasonably good agreement is achieved especially after 15 minutes of process time. Even though the melting of an encapsulated PCM at relatively high temperature has been explored in the present chapter, it should be mentioned that the values of the controlling parameters have been selected to be in the range of the low temperature melting case used for validation purposes, except for the Prandtl number (Pr) which in the present analysis is approximately equal to 9.0 and in the validation case is close to 60.

The influence of the Prandtl number on melting, in the absence of thermal radiation, was reported by Wang et al. [38] and Sparrow et al. [95] for a PCM confined in square and cylindrical containers. No significant difference in the melting dynamics was found. The increase of the Prandtl number accelerates the melting process but the physical events that describe the melting process of the PCM remain unchanged. Therefore, the validity of the comparison between the experimental data at low operating temperatures and the predicted numerical solution at relatively high operating temperatures seems to be appropriate. A separate validation case has been performed using $NaNO_3$ as a storage material and Figure 6 shows the comparison between the experimentally measured and the predicted temperature history at the center of the capsule. The details of the experimental procedure were described in [96] and reasonably good agreement is observed.

2.3. Results and Discussion Completely Filled Model

Thirteen configurations were analyzed in this section. All of them are summarized in Table 1. The effect of the outer wall temperature on the melting process for a constant capsule size is considered in cases 1 to 3. In cases 2, 4 and 5, the effect of the Stefan number is studied by keeping the Grashof number approximately unchanged. The effect of Grashof number on the melting process for a constant Stefan number, i.e. equal shell outer surface temperature (T_w= 316.8°C), is analyzed in cases 2 and 6 to 8. The effect of Prandtl number is analyzed by comparing the cases 6 and 9 for constant Stefan and Grashof numbers. Cases 7, 10 and 11 have been included in order to evaluate the influence of the shell material parameter χ ($\chi = 1 - \kappa_{pcm}/\kappa_{shell}$). The values of χ were selected for this study to lie between the limiting cases corresponding to the low and high thermal conductivity values. The selected materials are Nickel alloy, Silicon Dioxide and Zinc for cases 7, 10 and 11 respectively. The thermo-physical properties of the aforementioned materials have been taken from Incropera et al. In order to assess the effect of the initial temperature of the system on melting, cases 11 to 13 have been considered. A sub-cooling parameter ξ has been defined as $\xi = 1 - T_i/T_m$.

Table 1 Analyzed study cases

Case number	R_i (m)	$T_w - T_m$ (°C)	Gr_R	Pr	Ste	χ	ξ
1	0.010	5	$1.32x10^4$	8.98	0.048	0.966	0.00259
2		10	$2.69x10^4$	8.90	0.097		
3		15	$4.13x10^4$	8.81	0.145		
4	0.0092	12.6	$2.68x10^4$	8.84	0.122	0.966	0.00259
5	0.011	7.5	$2.66x10^4$	8.93	0.072		
6	0.015	10	$9.09x10^4$	8.90	0.097	0.966	0.00259
7	0.020		$2.15x10^5$				
8	0.025		$4.21x10^5$				
9	0.034	9.6	$9.09x10^4$	35	0.097	0.966	0.00259
10	0.02	10	$2.15x10^5$	8.90	0.097	0.6709	0.00259
11						0.9945	
12	0.02	10	$2.15x10^5$	8.90	0.097	0.6709	0.0172
13							0.0259

Table 2 Dimensionless groups

Group	Definition
Stefan number	$Ste = \frac{C_p(T_w - T_m)}{L}$
Grashof number	$Gr_R = \frac{g\beta(T_w - T_m)R_i^3}{\nu^2}$
Prandtl number	$Pr = \frac{\nu}{\alpha}$

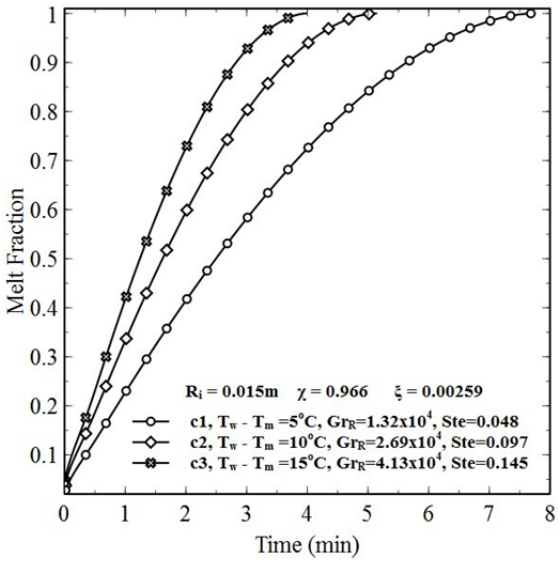

Figure 7 Effect of T_w on the melt fraction rate

The dimensionless parameters that are used to characterize the energy transport and fluid flow have been introduced in Table 2. It is appropriate to describe each parameter briefly before to start the discussion of the results. The Stefan number (Ste), defined as the ratio of the sensible heat and the latent heat of fusion. The Grashof number measures the ratio between the buoyancy and viscous forces. The Prandtl number, which describes the relationship between momentum diffusivity and thermal diffusivity. It is important to mention that the Grashof number values are based on the shell inner radius, on the temperature difference between the wall and melting temperatures and fluid properties evaluated at the reference temperature ($T_{ref} = (T_m + T_w)/2$).

The effect of the shell outer surface temperature was examined by analyzing cases 1 to 3. A 10 mm inner radii pellet was subjected to three different boundary condition values above the PCM melting temperature. The predicted liquid mass fraction for the aforementioned cases is depicted in Figure 7. Faster melting was achieved with higher values of the shell outer wall temperature. For a fixed capsule size, the melting time decreases 33.76% and 48.60% as the temperature difference $T_w - T_m$ increases from 5℃ to 10℃ and 15℃ respectively. However it should be noted that for the same PCM and capsule size both the Grashof and the Stefan numbers will vary with the temperature difference (T_w-T_m).

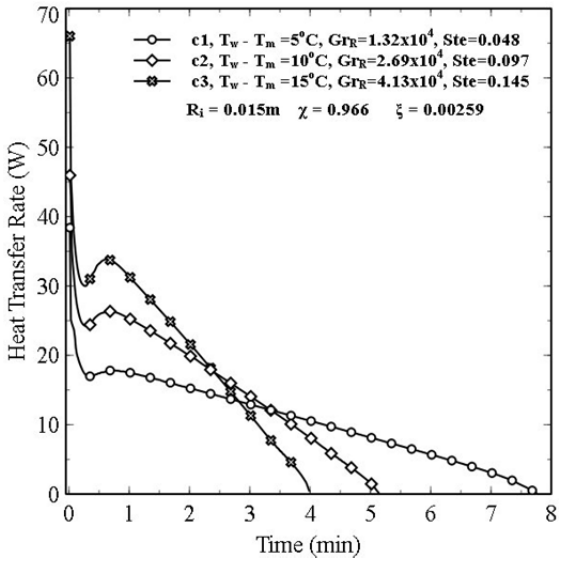

Figure 8 Effect of the outer wall temperature on the heat transfer rate

therefore, the previously discussed behavior can be associated with two different effects, the augmentation of the natural convection heat transfer and an increase in the sensible heat term of the Stefan number. Further in the discussion the effect of the Grashof number will be isolated, and a clear comparison will be presented.

In the discussion that follows, the influence of the outer wall temperature on the heat transfer rate at the inner surface of the shell is analyzed. However, before that, a description of the trend that each curve in Figure 8 follows is presented, in order to provide a better understanding of the physical meaning of the considered problem. Initially, the heat is transported mainly by conduction through the shell wall due to the temperature difference between the outer and inner wall temperatures. During this period, the inner wall temperature increases because of the energy transport and consequently the heat transfer flow through the wall decreases with time. This trend is clearly observed at the early stages of all the curves in Figure 8. Once the thermal condition at the vicinity of the inner surface reaches the PCM melting point, inward melting begins with the creation of the first layer of the molten PCM in that region. At this point, the density gradients within the melt layer induce the buoyancy-driven fluid motions that enable the natural convection heat transfer. During this time scale, the contribution from conduction to the net wall energy flux is very weak, and the energy exchange process is mainly due to free convection.

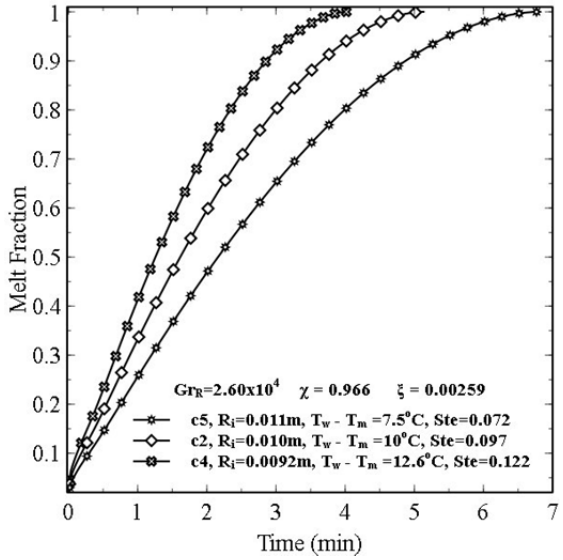

Figure 9 Effect of the Stefan number on the melt fraction

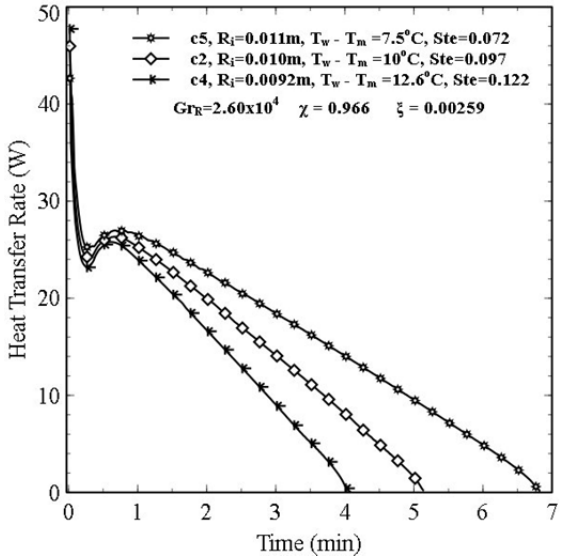

Figure 10 Effect of the Stefan number on the heat transfer rate

It may be seen that during this period, the total heat transfer increases with time and attains a maximum. After this period, all the curves present a slow decay trend with a progressive decrease toward the thermal equilibrium state of no energy transport. A similar trend has been reported and described by Sparrow et al. [95], Ho and Viskanta [97] and Jones et al. [98]. Attention is now turned to the role that the outer wall temperature plays on the previously described curves. During the period, $0 \leq t \leq 2.2$ min, the average heat transfer rate increases with an increase of the outer wall temperature. However after this interval all the curves cross each other, and an inverse trend is observed. The fact that thermal equilibrium will be reached sooner for the case with the higher wall and PCM melting temperature difference (higher Stefan and Grashof numbers) is a possible explanation for this trend.

The effect of Stefan number without a contribution of the Grashof number is illustrated in Figure 9 and Figure 10. Three cases under different wall temperature (7.5, 10 and 12.6°C) have been analyzed. The coupling between the Stefan and Grashof numbers is the temperature difference (T_w-T_m). In order to keep the Grashof number approximately constant and to attenuate the effect of the pellet size, the inner radius of the capsule has been carefully varied within the range between 9.2 to 11mm.

Figure 9, shows the predicted melt fraction rate as a function of process time for cases 2, 4 and 5. Faster melting is achieved when the Stefan number changes from 0.072 to 0.122. The heat transfer rate at the inner wall surface for cases 2, 4 and 5 is shown in Figure 10. During the diffusion-dominated melting, all the curves merged together in a single line. After that, because the Grashof number was kept constant, it is observed that the free convection heat transfer starts to influence the melting process at almost the same time. Later, all the curves show the slow decay trend until thermal equilibrium is attained. As discussed before in Figure 8, during this period the heat rate decreases when the Stefan number increases.

The predicted solid fraction, streamlines and isotherms contours for case 13 are presented in composite diagrams illustrated in Figure 11 at different times. The streamline contours are shown on the right half of each circle whereas the temperature contours are drawn on the left half, with the vertical axis of the sphere separating the two fields. The solid fraction at the given instant is shown in the gray region of each plot. At the early stages of melting, the thermal energy is transferred by conduction through the shell wall to the PCM. Accordingly the temperature distribution is close to the solution of the Laplace equation, i.e. the isotherms have a concentric ring shape, independent of the polar angle (see left hand side of Figure 11a). It is well known that, during the early periods of the process, the dominant transport phenomenon is heat conduction, and natural convection plays a small role. For times higher than $50s$, the isotherms begin to deviate from the concentric ring patterns indicating that natural convection starts to influence the melting process.

As the melting process proceeds, the recently formed liquid phase is heated by the inner wall of the shell, changing its density and generating a buoyancy-induced flow that drives the heated fluid upward. The ascending fluid transfer its heat to the adjacent cooler fluid located in the inward direction. It is cooled down and descends adjacent to the liquid-solid interface. Hence, an unsteady, counter-clockwise circulating flow is formed in the top portion of the capsule and is characterized by the streamline maps shown in the right side of Figure 11b through Figure 11d. A direct result of the circulation flow pattern is the faster melting that takes place on the top portion of the solid phase and causes a change in the original spherical shape of the solid core to an oblate spheroid. This can be observed in Figure 11e and Figure 11f.

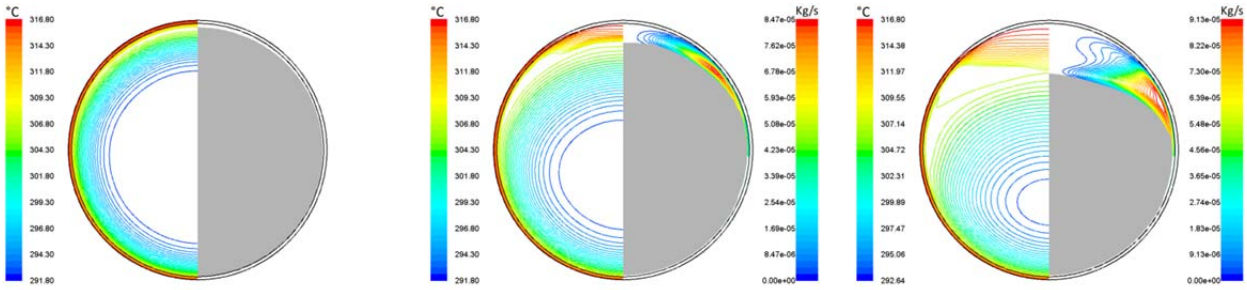

a) 20s b) 50s c) 110s

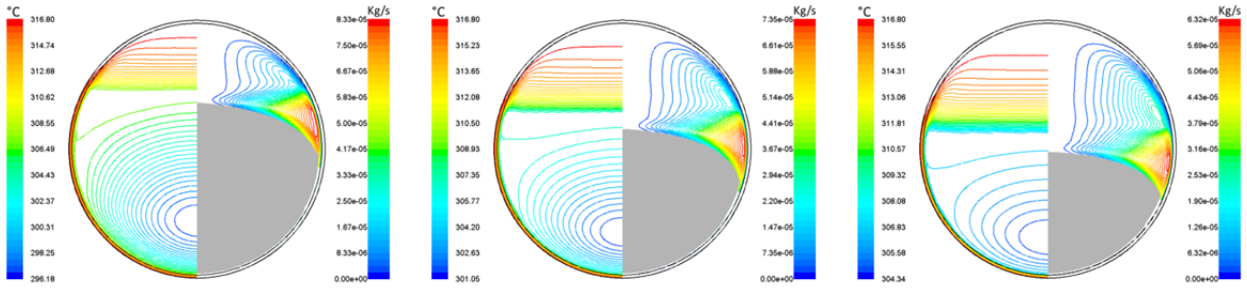

d) 180s e) 260s f) 340s

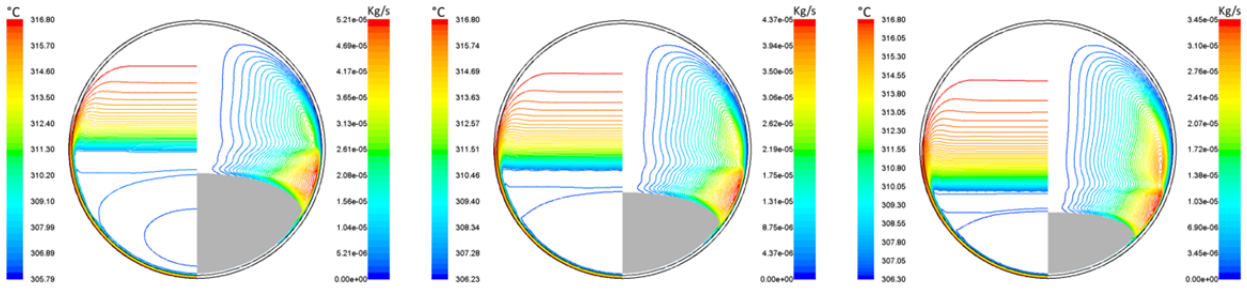

g) 420s h) 500s i) 590s

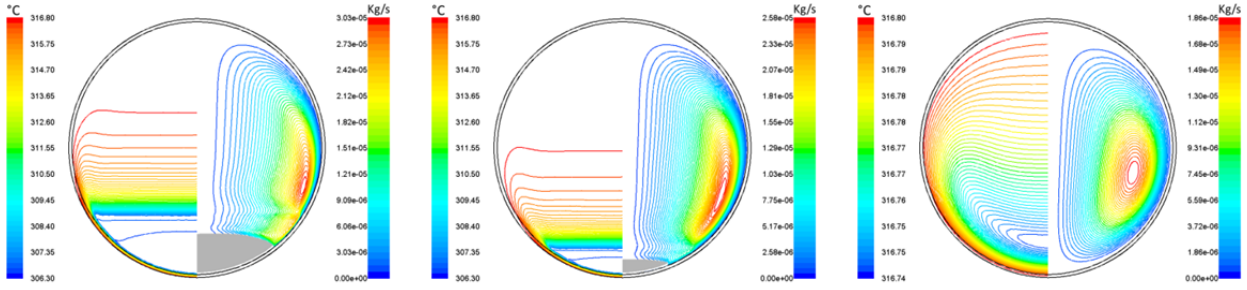

j) 700s k) 840s l) 1100s

Figure 11 Predicted process evolution for case 13.

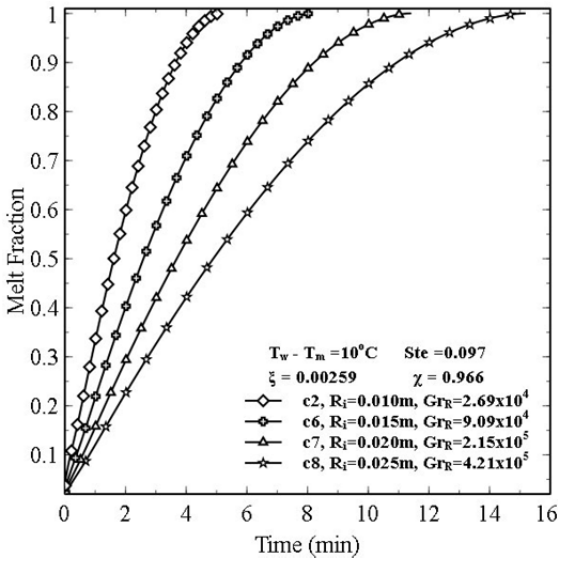

Figure 12 Effect of the size of the shell on the melt fraction

As the melting continues the circulating flow grows in physical extent, and the thermal energy is now transported from the inner shell wall to the liquid-solid interface primarily by natural convection. It may be seen from the left-hand side of Figure 11g and Figure 11i that large temperature gradients are developed in the PCM liquid portion located near the inner surface of the shell, while uniform temperature is observed across the thickness of the PCM liquid layer. A possible interpretation for these observations is that the boundary layer regime has been established in the fluid flow region adjacent to the inner shell wall. Similar findings were reported by Sparrow et al. [95].

As melting continues, the solid phase shrinks in size and the circulating flow grows in physical extent and starts to develop the crescent-shaped pattern (Figure 11j and Figure 11k). It should be noticed that the circulation speed of the convection cell decreases as the thermal equilibrium is attained. Figure 11l shows the temperature field (left) and the flow pattern (right) after the melting process is completed.

Special attention should be paid to the temperature range indicated in the color maps. A well-defined crescent shaped circulation flow pattern can be observed with the circulation center close to the capsule wall. On the temperature side, a stratified temperature field is observed with high-temperature gradients near the wall, especially in the lower part of the sphere.

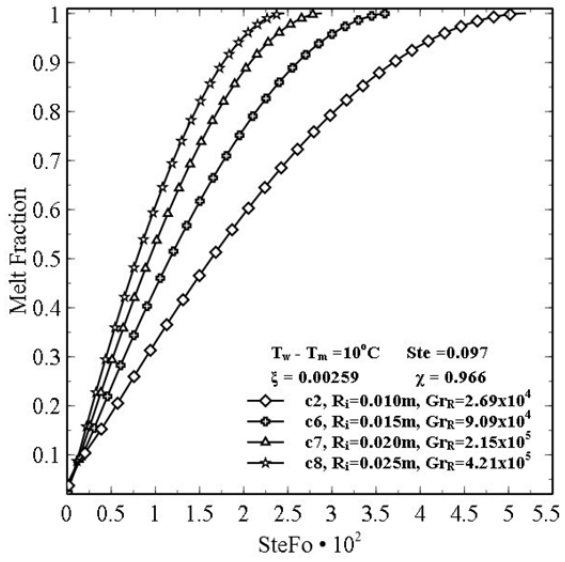

Figure 13 Effect of the Grashof number on the melt fraction

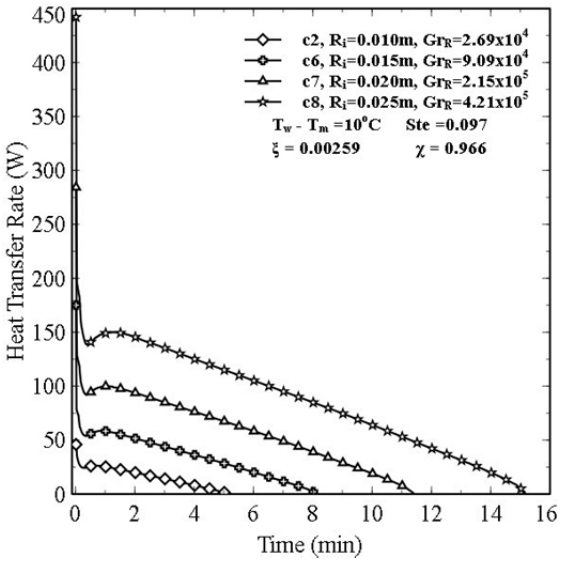

Figure 14 Effect of the size of the shell on the heat transfer rate

The results were found in good agreement with the experimental and numerical results on the natural convection inside a spherical enclosure reported by Chow and Akins [99] and Hutchins and Marschall [100]. The effect of the shell size on the melting rate for a constant Stefan number is presented in Figure 12. As expected, the larger the pellet size, the slower the pellet melts, with total melting times of 5.1, 8.1, 11.4 and 15.2 minutes for cases 2, 6, 7 and 8 respectively.

In order to isolate the effect of the size of the pellet and investigate the role that natural convection heat transfer plays in the melting process of Sodium Nitrate under a constant Stefan number, the results from Figure 12 have been plotted as a function of the dimensionless time ($SteFo$) that is defined as the product of the Stefan and Fourier numbers. It can be observed from Figure 13 that increasing the Grashof number from $2.69x10^4$ to $4.21x10^5$ enhances the melt fraction rate. A reversal of the trend is observed in this graph as compared with Figure 12 and is due to the fact that the Fourier number varies inversely as the square of the radius. Therefore for the same instance of time the Fourier number of a smaller radius case is higher than the value obtained for a higher radius case. Figure 14 shows the predicted average heat transfer rate at the inner surface of the shell for cases 2 and 6 to 8.

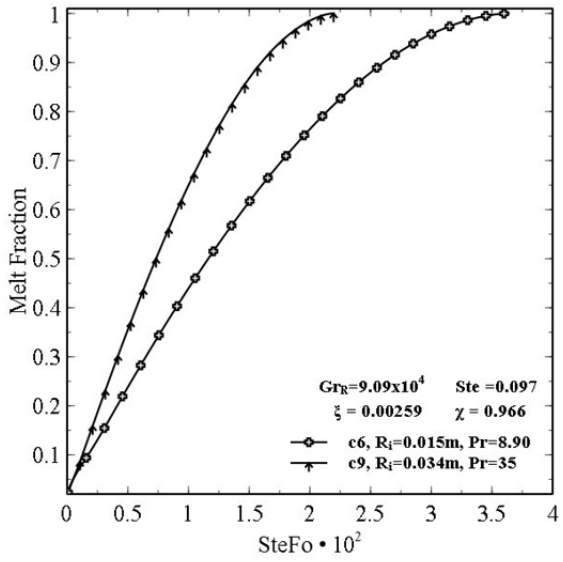

Figure 15 Effect of the Prandtl number on the melt fraction

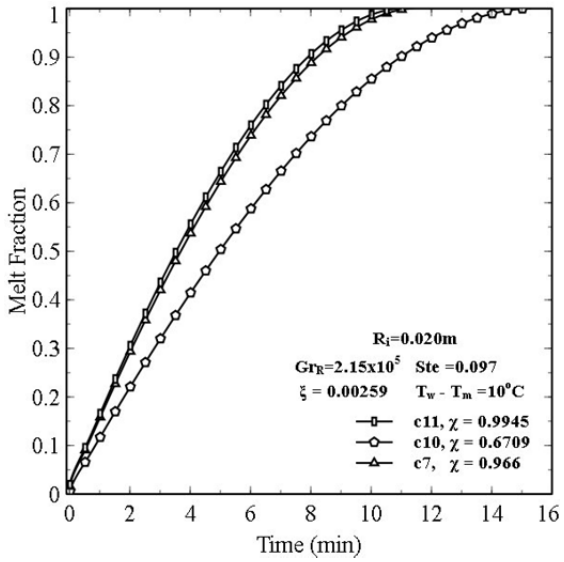

Figure 16 Effect of the shell material on the melt fraction

The heat rate was found to increase with the increase of the Grashof number. Also, the heat transfer rate is proportional to the heat transfer area; therefore, an increase in the available area for heat transfer causes an increase in the heat transfer rate. In order to investigate the role of Prandtl number (different phase change materials) under the same Grashof and Stefan numbers, cases 6 and 9 are compared. The material for case 9 is RT27. The Grashof and Stefan numbers were kept unchanged by manipulating the temperature difference and the pellet size.

Figure 15 shows the predicted liquid mass fraction as a function of dimensionless time for the aforementioned cases. A significant difference in the melt fraction rate is observed. Faster rate of melting is achieved when the Prandtl number is higher. At this point, the Rayleigh number ($Ra = GrPr$), which is one of the controlling parameters in the natural convection heat transfer mode, plays a significant role. For the same Grashof number, the convective energy transport mode of a PCM with larger Prandtl number will be enhanced and consequently its melting process will be faster compared to that in a PCM with smaller Prandtl number. The influence of the shell material thermal properties on the melt faction rate is presented in Figure 16.

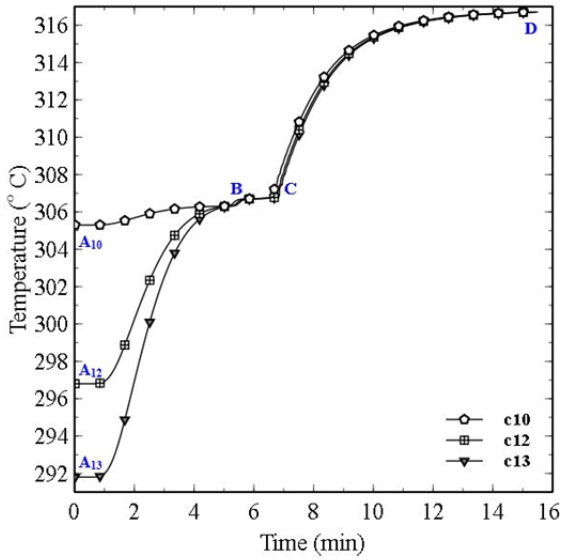

Figure 17 Effect of the initial temperature on the center point temperature history

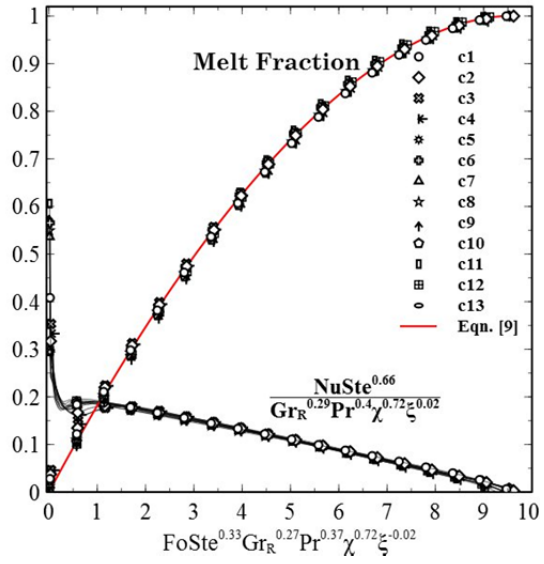

Figure 18 Melt fraction and Nusselt number as a function of controlling parameters

Three different shell materials have been chosen based on their thermal conductivity values in order to take into account the heat flow resistance at the shell wall. It can be observed from Figure 16 that there is no significant difference in the melt fraction rate between cases 7 and 11 which correspond to metallic shells (Nickel alloy and Zinc, respectively). However, a 34.1% increase in the total melting time is observed in the case 10, (low thermal conductivity material) as compared to cases 7 and 11. A low thermal conductivity wall generates a high heat flow resistance and consequently a high-temperature drop within the shell wall. Thermal energy requires more time to be transferred through the shell to start and continue the melting process.

The temperature history of the pellet center point is presented in Figure 17 for different initial temperatures of the system (1, 10 and 15℃ below the PCM melting temperature). Cases 10, 12 and 13 have been compared, and the difference in the heating dynamics is observed during the solid phase sensible heating process (A-B) because of the initial temperature value. However, no significant difference has been found during the phase change (B-C) and liquid sensible heating process (C-D).

In order to appropriately correlate the main results of this study and to develop applicable expressions regardless of any change in the system parameters, the dimensionless quantities that

characterize the natural convection-dominated melting process in a spherical enclosure have been arranged in the form $FoSte^{a}Gr_R^{b}Pr^{c}\chi^{d}\xi^{e}$. Figure 18 presents the melt fraction as a function of the previously described controlling parameter and it can be observed that all the curves practically merge into a single curve for the following exponents $a = 0.33$, $b = 0.27$, $c = 0.37$, $d = 0.72$ and $e = -0.02$. Based on that, the following correlation is proposed:

$$MF = 1 - \left[1 - \frac{FoSte^{0.33}Gr_R^{0.27}Pr^{0.37}\chi^{0.72}\xi^{-0.02}}{9.5}\right]^{1.8} \quad (9)$$

This correlation seems valid in a range encompassing the simulated cases:

$0.048 \leq Ste \leq 0.145$, $1.32x10^{4} \leq Gr_R \leq 4.21x10^{5}$, $8.90 \leq Pr \leq 35.0$, $0.6709 \leq \chi \leq 0.9945$, $0.00259 \leq \xi \leq 0.0259$.

A dimensionless quantity that includes the average Nusselt number, at the inner surface of the shell, in combination with the controlling parameters of the problem is proposed, as

$$\frac{NuSte^{f}}{Gr_R^{g}Pr^{h}\chi^{i}\xi^{j}}$$

The above quantity has been plotted, for each study case, as a function of the same dimensionless number used in Eqn. [9] and it is shown from Figure 18 that all the curves practically merge into a single curve for the following exponents: $f = 0.66$, $g = 0.29$, $h = 0.4$, $i = 0.72$ and $j = 0.02$.

2.4. Partially Filled Model[2]

Heretofore the discussion has been focused on the melting of $NaNO_3$ confined in a spherical shell whose internal volume was entirely filled with solid PCM initially. However because of the density differences between the liquid and solid PCM phases ($\rho_{sol} > \rho_{liq}$), it is fully expected that during the phase change process a volumetric expansion takes place. In the case of melting, the final volume of the liquid phase after completion of the process exceeds the volume originally occupied by the solid phase.

[2] The content of this section was published in: A. R. Archibold, J. Gonzalez-Aguilar, M. M. Rahman, D. Yogi Goswami, M. Romero and E. K. Stefanakos, "The melting process of storage materials with relatively high phase change temperatures in partially filled spherical shells," Applied Energy, vol. 116, pp. 243-252, 2014. Permission is included in Appendix B.

In order to accommodate the volume excess while melting, air space has been provided inside the capsule while the rest of the internal volume is filled with solid PCM. This additional feature in the mathematical model will take care about the assumption 6 defined in section 2.1 and extends the previously presented model. The inclusion of the air space also represents a more realistic physical representation of the encapsulated system towards the current commercially available manufacturing techniques for those systems.

The physical domain of the considered problem is presented in Figure 1b. A spherical nickel capsule with an internal radius, R_i and a wall thickness of 0.5 mm is partially filled with solid $NaNO_3$ and the remaining volume is occupied by air at 1 bar. The air space provides room for volumetric expansion during the phase change process. The problem has been modeled by solving the equations for the conservation of mass, momentum, and energy numerically using a control volume discretization approach [94] along with the enthalpy-porosity method [92] to track the melting front. The ideal gas equation of state is used to model the air density. The motion of the Air/PCM interface in the multiphase system was tracked by the Volume of Fluid (VOF) model. The model defines the volume fraction of the i^{th} fluid (α) which is defined as:

$$\alpha = \frac{volume\ of\ the\ phase\ in\ a\ cell}{volume\ of\ the\ cell} \tag{10}$$

and it takes the following values:

$$\begin{array}{cc} \alpha_i = 0 & if\ the\ cell\ is\ empty\ of\ the\ i^{th} fluid \\ \alpha_i = 1 & if\ the\ cell\ is\ full\ of\ the\ i^{th} fluid \\ 0 < \alpha_i < 1 & if\ the\ cell\ contains\ the\ fluid\ interface \end{array} \tag{11}$$

Based on that, the mass conservation equation is:

$$\frac{\partial}{\partial t}(\alpha_i \rho_i) + \nabla \cdot (\alpha_i \rho_i u_i) = 0 \tag{12}$$

where u_i is the velocity vector of the i^{th} fluid. The linear momentum conservation equation can be expressed as:

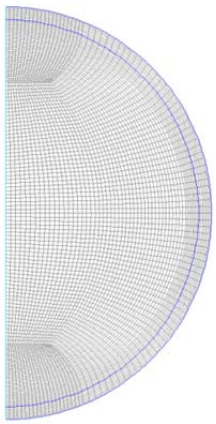

Figure 19 Grid distribution used in the analysis

$$\frac{\partial}{\partial t}(\alpha_i \rho_i u_i) + (u_i \cdot \nabla)(\alpha_i \rho_i u_i) = -\alpha_i \nabla P + \alpha_i \rho_i g + \alpha_i \eta \nabla^2 u_i \tag{13}$$

Finally, the energy conservation equation can be written as:

$$\frac{\partial}{\partial t}(\alpha_i \rho_i \hbar_i) + \nabla \cdot (\alpha_i \rho_i u_i \hbar_i) = \alpha_i \left(\frac{\partial P}{\partial t} + u_i \cdot \nabla P\right) + \alpha_i \nabla \cdot (\kappa_i \nabla T) \tag{14}$$

The computational domain was discretized using a structured longitude/latitude spherical grid consisting of 10446 quadrilateral cells with marked consideration at the PCM-Air interface and mesh parameters like maximum aspect ratio and element orthogonal quality. Figure 19 shows the grid distribution used to solve the completely and partially filled models. Commercially available software Ansys/Fluent v12 was employed for the calculations.

The governing equations were solved using the segregated solver. The energy and linear momentum equations were discretized using the First Order Upwind scheme. The Pressure Staggering Option (PRESTO) was used to discretize the pressure correction equation while the Semi-Implicit Method for Pressure-Linked Equations (SIMPLE) was used to discretize the continuity equation (Pressure-Velocity Coupling).

Validation has been performed by comparing the proposed numerical model with the experimental results reported by Assis et al. [29]. Figure 20 shows a comparison between the experimental data and the numerical results obtained from our simulations for the same problem.

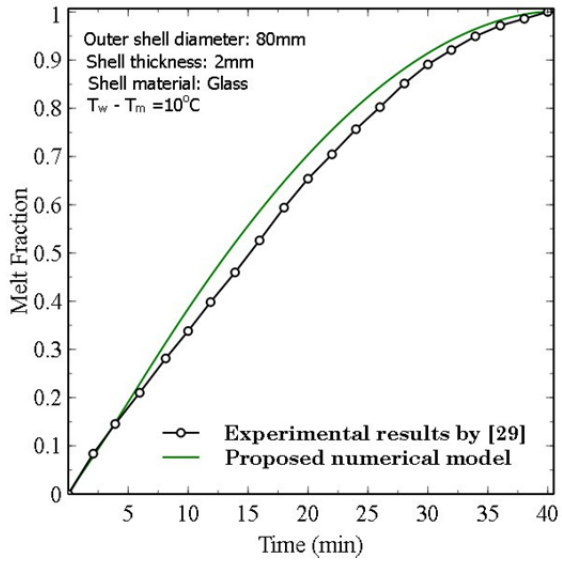

Figure 20 Validation case partially filled model

Table 3 Analyzed study cases in partially filled model

$case$	$R_i(m)$	$T_w - T_m$(°C)	Gr_R	Ste
1	0.010	5	$1.32\text{x}10^4$	0.048
2	0.015	5	$4.44\text{x}10^4$	0.048
3	0.02	5	$1.05\text{x}10^5$	0.048
4	0.025	5	$2.06\text{x}10^5$	0.048
5	0.015	10	$9.09\text{x}10^4$	0.097
6	0.015	15	$1.39\text{x}10^5$	0.145
7	0.015	20	$1.90\text{x}10^5$	0.194
8	0.0165	8	$9.09\text{x}10^4$	0.077

Reasonably good agreement was found between the numerically predicted melt fraction rate and the experimental results. Even though the PCM considered in the present study is different from the analyzed in the validation case with Prandtl numbers approximately close to 9.0 and 35 respectively, no differences in the melting dynamics between the two PCMs were found. The discussion of the validity of the validation exercises was provided in section 2.2. It should be pointed out that the shell material used in [29] was glass while in this study Nickel has been used. Apart from the anticipated faster melting rate obtained with the increase of the shell thermal conductivity, the melting dynamics of the two PCMs was preserved.

Eight different cases were analyzed in this study as summarized in Table 3. The effect of the Grashof number on the melting and heat transfer for a constant Stefan number was evaluated by considering the first four study cases, where the shell diameter was varied from 20 to 50 mm. Study cases 5 to 7 have been included in order to assess the role of the outer surface temperature on the melting process. The evolution of the predicted isotherms, streamline contours, and PCM solid and air fraction distributions, during the melting of case 2, are presented in the composite diagrams in Figure 21. The history of the process is depicted as a function of time.

The temperature distribution of the system is presented in the left half of each circle while the right half contains the molten PCM streamline contours and the PCM solid phase and the air fractions. As discussed previously, initially the heat is transferred by conduction through the capsule wall. After that, thermal energy travels faster through the air due to its higher thermal diffusivity as compared to the PCM. As a result, a counterclockwise buoyancy-induced recirculating flow is created in the air zone. This causes the skewed temperature contours observed in the top-left portion of Figure 21a. As a result of the diffusion-controlled heat transfer process within the PCM, melting is initiated in the peripheral portion of the PCM and an axisymmetric thin layer of molten PCM is created adjacent to the inner wall of the capsule (as seen at right side of Figure 21a). The heat flow at the interface between the air portion and the top solid PCM is not at the same rate. Consequently, the upper part of the sodium nitrate remains solid.

As the molten portion gets larger, the density of the fluid in the vicinity of the inner surface of the shell decreases due to the temperature gradient and flows up covering the top region of the solid fraction. The occurrence of the buoyancy-induced liquid flow that initiates natural convection within the melt layer was previously discussed in the section 2.3 and will be just mentioned without further elaboration. The streamline contours of the above-mentioned natural convection flow are observed at the right PCM side of all the plots in Figure 21. This recirculating flow enhances the heating rate towards the solid, increasing the melting in this zone, and the solid adopts an oblate spheroid-shape on its top (as seen in Figure 21b and Figure 21c).

As the melting process proceeds, the solid portion shrinks in size and the recirculating flow grows in physical extent (see Figure 21d to Figure 21f). Also, the sodium nitrate progressively fills up the pellet due to the volumetric expansion of the liquid phase, as shown in the right-hand side of Figure 21g and Figure 21h. Consequently, the air is compressed, increasing the pressure inside the pellet. In order to easily track the motion of the Air/PCM interface as a result of the thermal expansion, a horizontal line is included on the right side of all the presented plots of Figure 21, indicating the initial position of the interface and its displacement. For instance, the salt quantity inside the pellet should be carefully calculated in order to guarantee that the internal pressure does not exceed the shell mechanical strength.

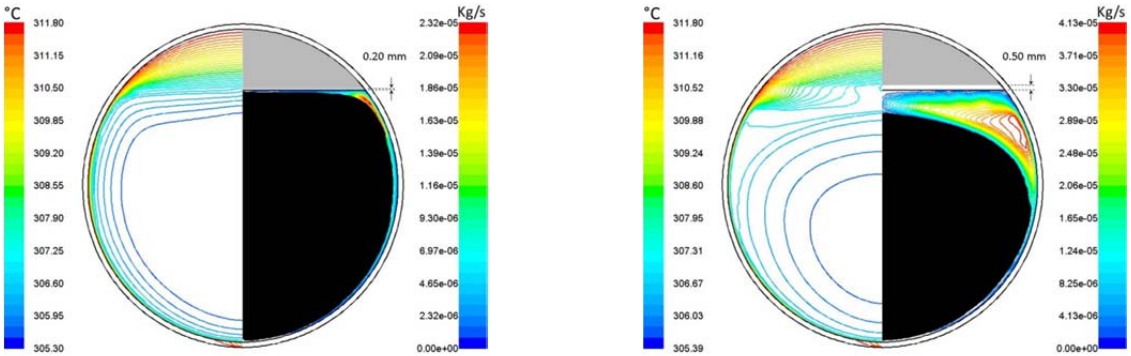

a) 16s

b) 100s

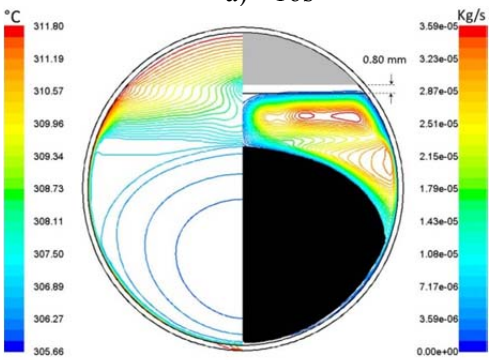

c) 184s

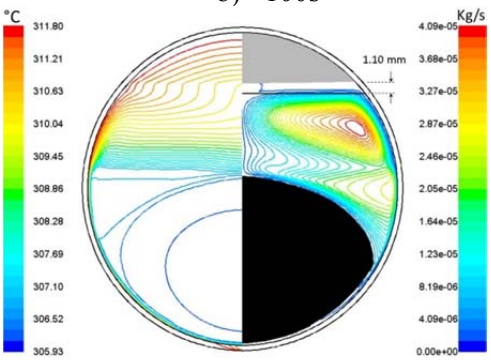

d) 268s

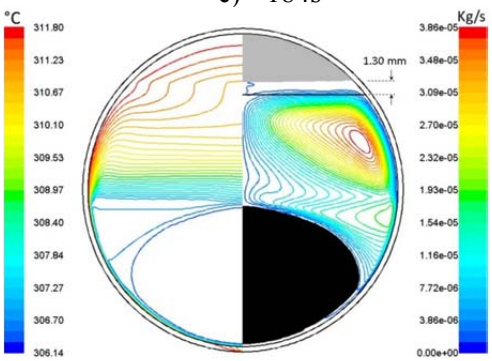

e) 352s

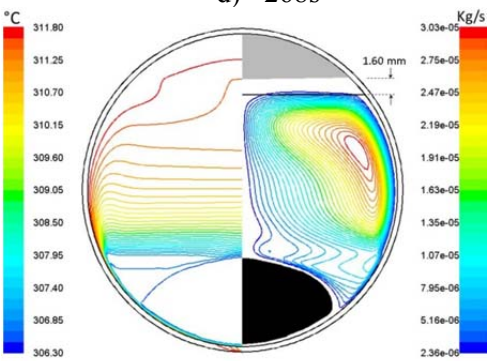

f) 520s

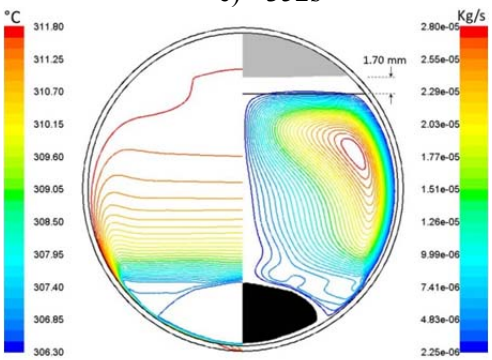

g) 604s

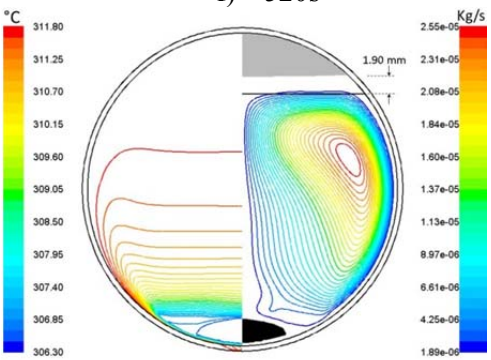

h) 720s

Figure 21 Predicted evolution of the melting process for study case 2

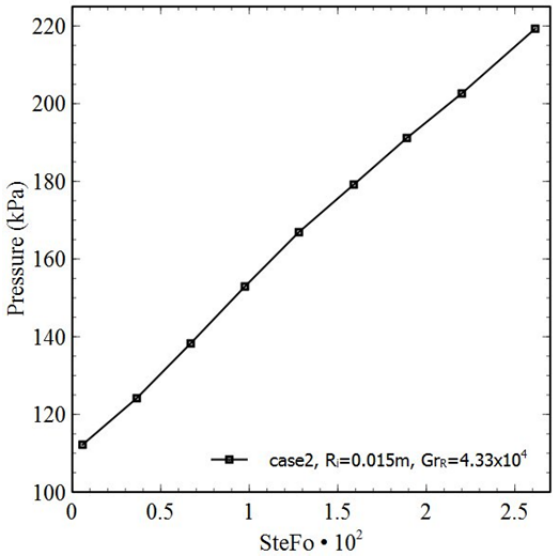

Figure 22 Internal pressure history for case 2

The pressure evolution inside the capsule is presented in Figure 22 for the study case 2. A linear profile is observed with a maximum pressure of 220 kPa. These observations suggest that the shell material and thickness need to meet the mechanical and thermal stresses induced by the pressure and temperature differences between the inner and outer wall surfaces.

Melt fractions for all the analyzed study cases are plotted as a function of combinations of Fourier, Stefan and Grashof numbers in Figure 23 in order to develop a generalized correlation. By manipulating the exponents of the Stefan and Grashof numbers, it was determined that all the melt fraction curves converge to a single location when the exponent of the Stefan number is 0.37, and the exponent of the Grashof number is 0.25. An equation for the generalized melt fraction (MF) curve can be written as:

$$MF = 1 - \left[1 - \frac{FoSte^{0.37} Gr_R^{0.25}}{2.8}\right]^{2.35} \quad (15)$$

A dimensionless group ($NuSte^{0.61}/Gr_R^{0.27}$) has been defined in order to correlate the heat transfer interactions during the analyzed phase change process. Figure 23 shows the corresponding variation with the Fourier, Stefan and Grashof numbers for all the study cases.

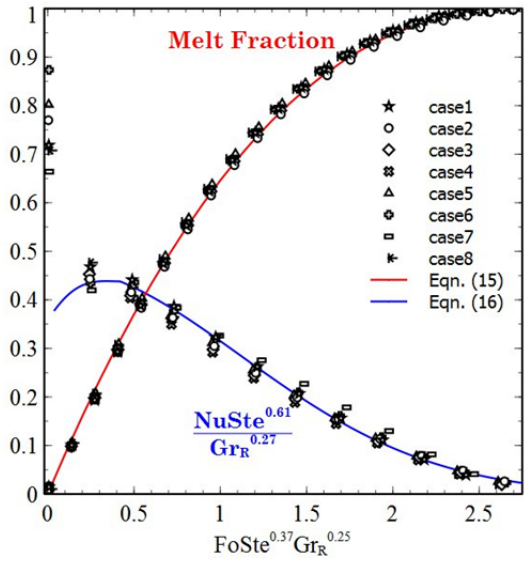

Figure 23 Melt fraction and Nusselt number correlations partially filled model

It may be observed that for the proposed exponents of the Stefan and Grashof numbers all the curves practically merge to a single line. The following piecewise correlation for the Nusselt number dimensionless group is proposed:

$$\frac{NuSte^{0.61}}{Gr_R^{0.27}} = \begin{cases} 0.29exp(-4.75\xi^{2.2}) + \sin(0.068 + 0.55\xi), & 0.04 \le \xi < 0.4 \\ 0.47exp(-0.4\xi^{2.0}), & 0.4 \le \xi \le 3.0 \end{cases} \quad (16)$$

where: $\xi = FoSte^{0.37}Gr_R^{0.25}$. The above correlations cover the range encompassing the cases simulated: $0.048 < Ste < 0.194$, $1.32\,x\,10^4 < GrR < 2.06\,x\,10^5$, $8.73 < Pr < 9.05$.

CHAPTER 3[3]: SOLIDIFICATION OF SODIUM NITRATE IN A SPHERICAL SHELL

The previous chapter presented results directly relevant to the natural convection induced melting process in the absence of thermal radiation. It was reported that natural convection exerts a strong influence on the melting of $NaNO_3$. However, thermal radiation may also contribute significantly to the net energy exchange process during phase change which would result in faster melting/freezing.

Experimental measurements of the $NaNO_3$ optical absorption properties, reported by [101], have shown the potential of this salt to absorb thermal radiation in the near infrared portion of the spectrum. The purpose of this chapter is to extend the previous mathematical model to include thermal radiation within the PCM and quantify its contribution to the overall energy transport. The influence of simultaneous conduction, convection and thermal radiation on the freezing dynamics of a non-opaque media, encapsulated in a closed spherical shell at relatively high temperatures, is examined. To accomplish that, a two-dimensional, axisymmetric, transient model has been solved numerically.

3.1. Heat Transfer Analysis

The considered system is schematically shown in a cross-sectional view in Figure 24. It consists of an opaque, gray and a diffuse spherical shell of inner radius R_i and wall thickness δ. Initially the shell inner volume is completely filled with liquid PCM at temperature T_o, which is higher than the storage material melting temperature T_m. At time $t > 0$, the outer boundary surface, whose emissivity was set to unity, is subjected to a convective boundary condition characterized by a heat transfer coefficient h_∞ and a free stream temperature T_∞, which is lower than T_m. The PCM is treated as a semitransparent, non-gray, medium being emitting and absorbing. Uniform and equal index of refraction of each phase has been assumed. The scattering of thermal radiation has been neglected in this study.

[3] The content of this chapter has been submitted to the Int. Journal of Heat and Mass Transfer. A. R. Archibold, D. Y. Goswami, M. M. Rahman and E. K. Stefanakos, "Multi-mode heat transfer analysis during freezing of an encapsulated storage medium," *International Journal of Heat and Mass Transfer*, 2014, In review. Permission is included in Appendix B.

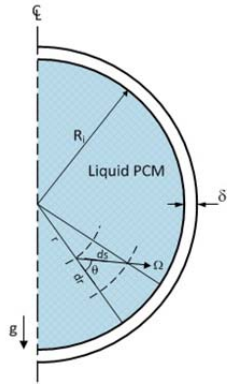

Figure 24 Schematic representation of the physical domain

Multiple physical assumptions have been considered in the mathematical model and attention will now be turned to discuss their applicability. Experimental observations on the freezing of a low-temperature PCM [77] and the natural convection heat transfer to a fluid contained in spherical containers [99] suggest that both the phase change process and the buoyancy induced fluid motion can be modeled as axisymmetric. It was also reported by [99] that for Rayleigh numbers below 10^7, laminar flow was found to exist. In the present study the range of the examined Rayleigh numbers was $7.92x10^4 \leq Ra \leq 2.0x10^7$. Therefore, the process has been modeled as axisymmetric and laminar flow has been assumed for the fluid motion within the liquid phase.

In order to account for natural convection, temperature dependent density within the liquid phase has been defined only in the body force terms of the momentum equations based on the Boussinesq approximation. The PCM is assumed to be a continuous, homogeneous and isotropic substance. The wall thickness used in all the study cases was 1 mm. The previously described problem was defined by the equations of continuity (Eqn.1), momentum (Eqns. 2 and 3) and energy. For a two-dimensional, viscous Newtonian flow with no viscous with no viscous dissipation in a polar and radial coordinate system, the energy equation may be written as:

$$\frac{\partial h}{\partial t} + \frac{1}{r^2}\frac{\partial}{\partial r}(r^2 \vartheta_r h) + \frac{1}{r\,sin\,\theta}\frac{\partial}{\partial \theta}(\vartheta_\theta sin\theta h) =$$

$$\alpha \nabla^2 h - \frac{1}{\rho c_p}\left(\frac{\partial \lambda}{\partial t} + \frac{1}{r^2}\frac{\partial}{\partial r}(r^2 \vartheta_r \lambda) + \frac{1}{r\,sin\,\theta}\frac{\partial}{\partial \theta}(\vartheta_\theta sin\theta \lambda)\right) - \nabla \cdot q_r \qquad (17)$$

The last term on the right-hand side of Eqn. 17 accounts for the thermal radiation contribution, and it is coupled with the radiation intensity via the equation of radiative transfer (RTE). For diffuse radiation and isotropic scattering in a spherically symmetric medium the RTE [102] can be written as:

$$\frac{\mu}{r^2}\frac{\partial[r^2 I(r,\mu)]}{\partial r}+\frac{1}{r}\frac{\partial[(1-\mu^2)I(r,\mu)]}{\partial \mu}+\kappa_a I(r,\mu)=\kappa_a I_b(T) \tag{18}$$

where $I(r,\mu)$ is the radiation intensity, which is a function of position and direction, μ is the cosine of the angle between the direction Ω of the beam and the extension of the radius vector r, $I_b(T)$ is the intensity of black body radiation at the temperature of the medium. In the discrete ordinate method, the RTE is approximated by discretizing the entire incident solid angle using a finite number of ordinate directions [103, 104, 105, 106]. Therefore, equation (18) is written for each ordinate and reduces to a discrete system of differential equations (Eqn. 19), sufficient to solve for radiation intensity (I_i) at every location within the medium.

$$\frac{\mu_i}{r^2}\frac{\partial[r^2 I_i]}{\partial r}+\frac{1}{r}\frac{\partial[(1-\mu^2)I]_{\mu=\mu_i}}{\partial \mu}+\kappa_a I_i=\kappa_a I_b \tag{19}$$

where the subscript i denotes the ordinate directions. Once the radiation intensity is known, the local radiative heat flux (q_r) can be determined based on the following expression:

$$q_r=2\pi\int_{-1}^{1} I(r,\mu)\mu d\mu=2\pi\sum_{i=1}^{n}\mu_i w_i I_i \tag{20}$$

3.2. Grid Independence and Validation of the Numerical Solution

Two different properties have been selected to evaluate the effect of mesh grid size on the solution of the model. The mass average solid fraction and the dimensionless temperature (Θ_n) of a node located at the horizontal axis of the domain have been plotted as functions of the dimensionless time (as seen in Figure 25) for different grid densities with $R_i=15mm$, $T_o-T_m=20℃$, and $T_m-T_\infty=20.5℃$. It may be seen from Figure 25 that for the given conditions, additional refining of the grid from 1400 to 10400 elements has no influence on the freezing rate. No significant difference is observed in the solidification dynamics with the freezing time approximately 28 minutes.

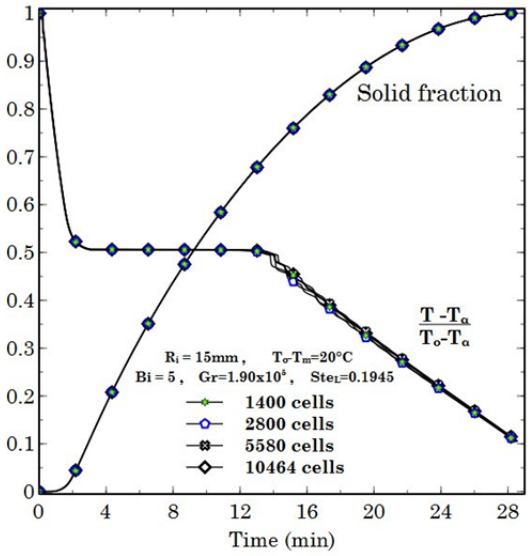

Figure 25 Influence of the grid size on the solidification rate and node temperature

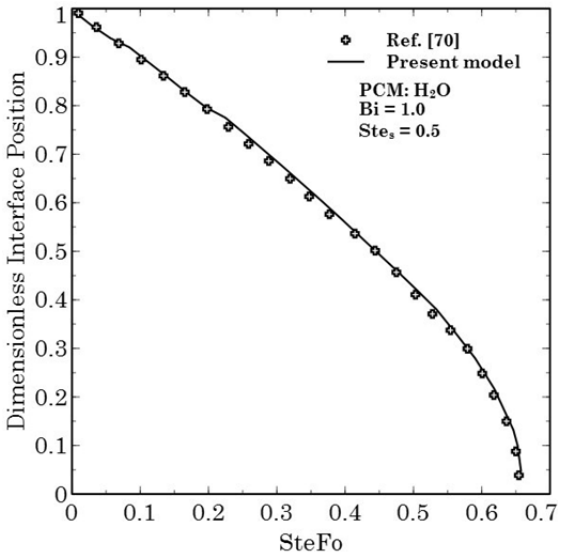

Figure 26 Evolution of the solid/liquid interface during single phase Stefan problem

The same trend is observed in the dimensionless temperature response during the liquid phase sensible cooling and phase transition process $0 \leq t \leq 13.1min$. However, some minor differences are observed at the beginning of the solid phase sensible cooling process with slightly faster temperature response with the increase of the element size. A grid distribution with 5580 elements and minimum and maximum element sizes as $0.29x0.15mm$ and $0.15x0.55mm$ (width x height) respectively, was found sufficient to achieve independence of the solution. The time step (t_{sp}) used in the calculations in this chapter is the same utilized in the computations in chapter 2 (0.005sec).

The proposed numerical model has been validated against the semi-analytical solution of the single phase Stefan problem, in the absence of thermal radiation, reported by Hill and Kucera [70]. A comparison is provided in Figure 26 which illustrates the variation of the dimensionless solid/liquid interface with respect to the dimensionless time for parametric values of the Stefan and Biot numbers equal to 0.5 and 1 respectively. Reasonably good agreement is observed between the numerical and the analytical results. However, as it was mentioned in chapter 1, the proposed model also incorporates the participating thermal radiation within the PCM during the phase change process, which is missing in the simplified Stefan problem where the heat of fusion is assumed to be removed by conduction only.

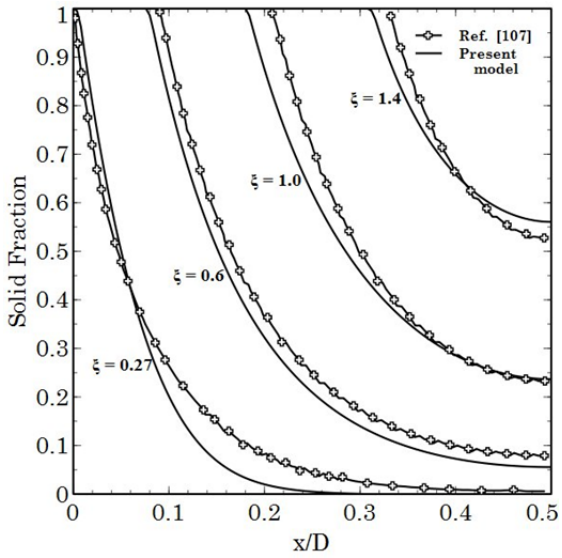

Figure 27 Solid fraction distribution along the slab

Therefore, a second validation test has been performed in order to verify the thermal response of the one-dimensional transient solidification problem of a semitransparent planar medium in the presence of simultaneous conduction and thermal radiation. Figure 27 shows the solid fraction distribution along the characteristic length of the slab for different dimensionless times (ξ). The figure also includes a comparison between the results reported by Parida et al. [107] and the predictions obtained from our simulation of the same problem. The general trends for both simulations are the formation of a mushy zone that extends into the slab early in the process and the propagation of the solid phase into the slab as the freezing proceeds. Reasonably good agreement is observed.

3.3. Results and Discussion

The parameters analyzed in the course of this investigation are the melt degree of superheat ($T_o - T_m$), the external heat transfer coefficient that characterizes the outer shell wall boundary condition, the size of the shell and thermal radiation heat transfer within the PCM. These parameters have been selected based on a practical point of view of the possible use of $NaNO_3$ for storage of thermal energy in concentrating solar power plants. Eight different study cases have been defined to identify the aforementioned parameters and are presented in Table 4.

Under the present conditions, the liquid phase degree of superheat will activate the natural convection energy transport and consequently affect the freezing dynamic of the PCM, at least during the early periods of the process, as reported by Sparrow and Broadbent [73] for the solidification in vertical cylinders. Four superheating conditions were considered, 1, 5, 10 and 20°C above the PCM melting temperature respectively. Study cases 1-3 and 5 represent this effect. As it was mentioned before, a uniform convective thermal boundary condition was imposed at the outer wall of the capsule in order to represent the discharging process in a packed bed system.

The Biot number ($Bi = h_\infty R_i/\kappa_{sol}$) has been used to characterize this effect where three different heat transfer coefficients (h_∞) have been evaluated and their, influence on the thermal behavior of the system was analyzed. Study cases 4-6 describe this effect. Three different shell sizes have been analyzed in this study with inner radius of 15, 25 and 35mm respectively. These conditions are represented by study cases 6-8. In order to account for the participating thermal radiation, the PCM has been modeled as a semitransparent, non-gray medium in all the study cases presented in Table 4. A seven-band model, based on the experimental results reported by Ramdas [101] has been used to account for the spectral dependence of the PCM optical properties.

Table 4 Geometrical and thermal parameters

$case$	$R_i(m)$	$T_o - T_m$(°C)	Gr_R	Bi	Ste_{Liq}
1	0.015	1	$8.77\text{x}10^3$	5	0.0096
2	0.015	5	$4.46\text{x}10^4$	5	0.048
3	0.015	10	$9.09\text{x}10^4$	5	0.096
4	0.015	20	$1.90\text{x}10^5$	1	0.195
5	0.015	20	$1.90\text{x}10^5$	5	0.195
6	0.015	20	$1.90\text{x}10^5$	10	0.195
7	0.025	20	$8.81\text{x}10^5$	16.67	0.195
8	0.035	20	$2.42\text{x}10^6$	23.34	0.195

A limiting case, in which the PCM has been treated as a non-attenuating and non-emitting medium with the shell inner surface emissivity equal to zero, has been also included in the analysis, as a reference case in which thermal radiation does not play any role. The shell size and thermal conditions of the limiting case have been selected to be exactly the same as that used in the study case 5. Further, in this section a discussion about the relevant radiative properties is also included.

The evolution of the solidification process at various time instants is presented in Figure 28. Each plot is composed of two separate halves divided by the symmetry line of the domain that is used as the ordinate in the defined radial and axial (Z) coordinate system. Isotherms are presented in the left half while the streamline contours and solid fraction are shown in the right half.

As the cooling process begins, a buoyancy-induced force drives the molten PCM located at the central core of the capsule upward. The ascending fluid transfers its heat to the adjacent cooler fluid near the inside wall. It is cooled down and descends nearby the inner shell wall. Hence an unsteady, clockwise circulating flow is formed in the melt layer which is characterized by the closed streamline maps observed on the right side of Figure 28a and 28b. This recirculation pattern delivers relatively hot liquid to the upper region of the capsule, where its presence retards the cooling process. During this short time scale (relative to the period to complete the PCM freezing), the hot fluid continuously arrives in this region, impinges on the inner wall and displaces the cooler fluid down.

Inspection of the temperature contours of Figures 28a and 28b reveals a stratified temperature field with the highest temperature in the upper zone. During its travel along the inner wall, the displaced fluid is being cooled by the outer wall and descends toward the lower portion of the capsule where the temperature drops below the melting point and therefore inward solidification begins.

A closer view of the right-hand side of Figures 28a and 28b illustrates the formation of the first PCM solid layer at the bottom of the shell. During this time scale, the buoyancy induced flow pattern in the melt layer is characterized by a thin layer of liquid PCM flowing downward and a large core of fluid moving upward. The thickness of the down-flow fell in the range of 12 to 18.7% of the inner radius of the shell at early times.

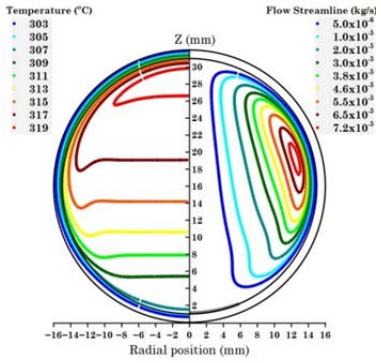

a) 60s

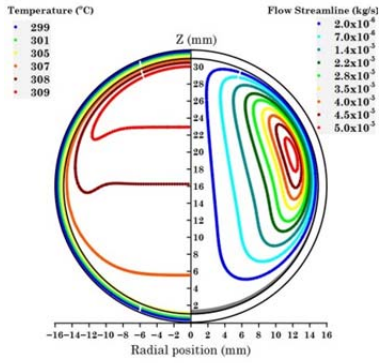

b) 120s

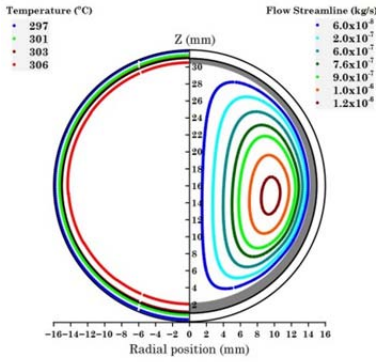

c) 240s

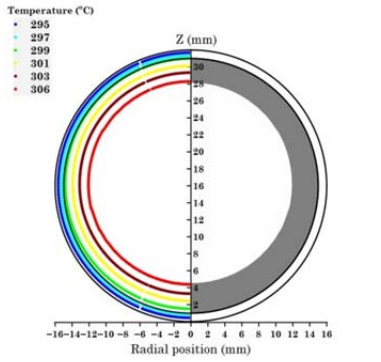

d) 600s

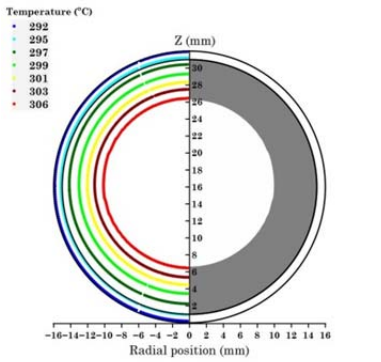

e) 900s

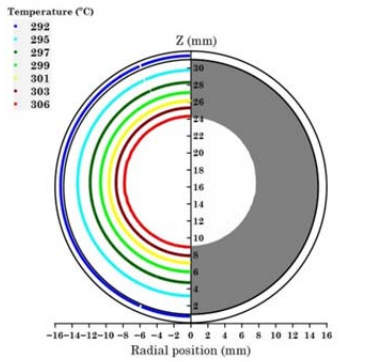

f) 1200s

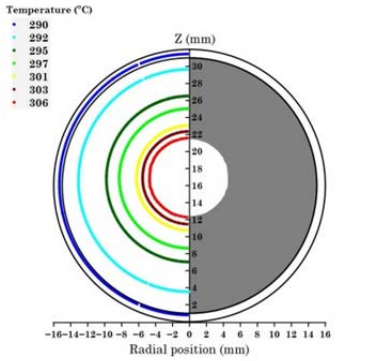

g) 1500s

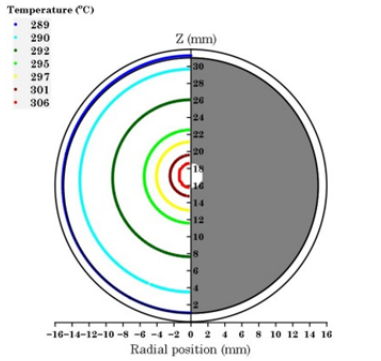

h) 1680s

Figure 28 Predicted evolution of the solidification process for case5

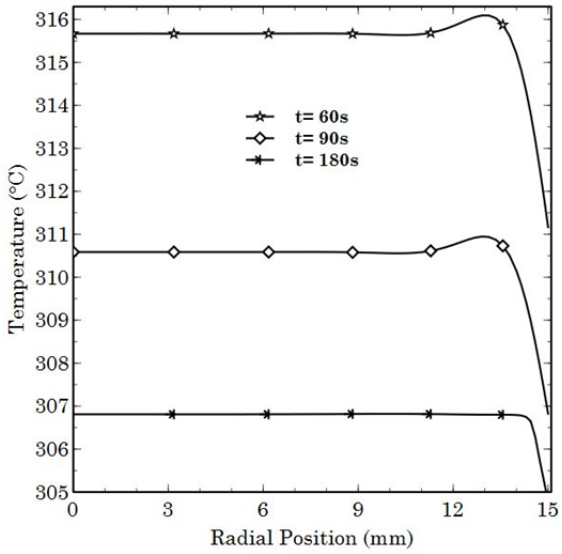

Figure 29 Temperature distribution along the shell horizontal radius

These findings are in agreement with the experimental observations of the natural convection flow inside spherical enclosures reported by Chow and Akins [99].

In order to complete the analysis of the physical events that characterize the early periods of freezing ($0 \leq t \leq 150s$) where free convection is believed to be the dominant heat transfer mode, the temperature profile at the horizontal radius is presented in Figure 29 for different times. Sharp temperature gradients are developed in the fluid adjacent to the inner wall while uniform temperature is observed across the thickness of the liquid layer. This trend is associated with the formation of the thermal boundary layer near the inner shell wall. Similar results were reported by Sparrow et al. [95] for the melting problem in vertical cylinders.

Inspection of the left-hand side of Figure 28c shows that the temperature gradient within the melt layer that was responsible for the natural convection motion is no longer in evidence, therefore, a reduction of the streamline contour intensity is also observed as compared with the previous time instant.

Another important observation of Figure 28c is that the temperature within the melt layer is slightly above the phase change temperature, meaning that during the first 240s of the process the temperature has dropped approximately 20°C. With the absence of the hot flow at the top of the shell, the inward solidification proceeds and solid PCM is observed in the vicinity of all the inner shell.

Figures 28d to 28h illustrate the freezing dynamics of the PCM with almost concentric ring shape for the isotherms as well as the solid/liquid interface. The absence of the temperature gradients within the melt layer is the reason why the streamlines maps are not included in Figures 28d to 28h.

To place these findings in perspective, the events that occur during the presented freezing process can be divided into two different time scales. A short time scale $0 \leq t \leq 150s$ in which natural convection plays a first order role, but is rapidly terminated because of the sharp decrease of the liquid core temperature. On the other hand, a second and larger time scale (relative to the period to complete the PCM freezing) that shows solid-phase isotherms close to the solution of the Laplace equation, where it is assumed that the leading energy transport mechanisms are conduction and radiation. In that context, the simultaneous interaction between the conductive and the radiative transfer provides a more effective mechanism to transport the liberated latent heat of fusion from the solid/liquid interface to the outer shell wall.

It has been previously reported by [51] that the presence of thermal radiation significantly improves the heating or cooling rates as compared with the pure conduction systems. Based on that, a spectral absorption coefficient has been defined for both solid and liquid PCM phases in order to account for the participating thermal radiation that may occur during the freezing process.

Figure 30 shows the experimental measurements of the near infrared transmittance of $NaNO_3$, reported by Ramdas [101] and the approximate seven band model that was used during the calculation process. For each band, a uniform absorption coefficient has been estimated while the contribution of scattering to the extinction of thermal radiation has been neglected. Even though in this chapter, emphasis has been placed on Sodium Nitrate as a PCM, no further difficulties are anticipated to analyze other PCMs in the presented model. In chapter 4, the influence of thermal radiation on melting and solidification of a PCM confined in spherical shell will be analyzed and discussed, at higher operating temperatures (+800℃).

Recent experimental contributions on the radiative properties of high-temperature eutectic systems reported by [108] can be utilized to extend and compare the results reported in this investigation.

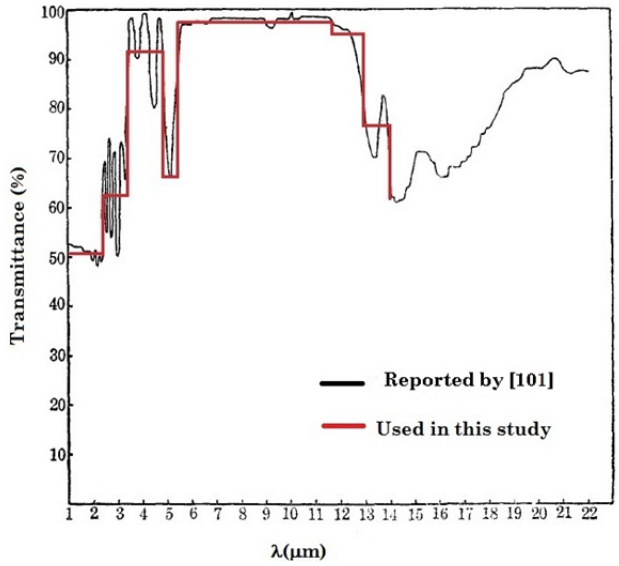

Figure 30 Spectral transmittance of Sodium Nitrate

The predicted variation of the solid fraction with time for the limiting case and the study case 5 is presented in Figure 31. It may be seen that faster solidification is achieved when thermal radiation is considered. The solidification time decreases 17% when thermal radiation is included in the model. A closer look of the solid fraction curves reveals that during the early times, the solid fraction is equal to zero, indicating the existence of the pure natural convection motions within the liquid PCM. As the freezing initiates, a small difference is observed between the curves with study case 5 predicting a slightly faster solidification. As the solid layer increases its size, the contribution of thermal radiation becomes more significant in the presence of conduction, resulting in a more pronounced difference.

The predicted energy transfer interactions at the inner shell wall are also included in Figure 31 and are displayed in broken lines. In order to appropriately correlate the heat transfer data, two different dimensionless parameters have been defined, the Nusselt number (Nu) which is estimated based on the conductive and the convective heat fluxes (q_{cd} and q_{cv}) and the dimensionless radiative flux (Ψ) which has been calculated based on the radiation heat flux (q_r). It should be noticed that the limiting case is only characterized by the Nusselt number because of the absence of thermal radiation while the case 5 accounts for all the energy transport modes.

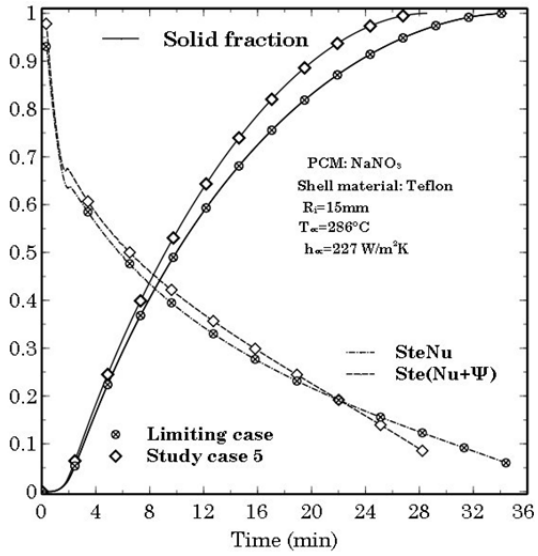

Figure 31 Influence of radiative energy transfer on the thermal dynamics of the process

Both curves are multiplied by the Stefan number in order to accommodate them in the solid fraction plot. It is believed that during the early times, the heat is transported mainly by conduction through the shell wall, because of the absence of natural convection. This short time scale characterizes the period to reach the required melt layer temperature difference that activates the unstable thermal condition where density gradients promote buoyancy-driven fluid motion. It should be pointed out that initially the liquid PCM is in a stagnant condition. Consequently, during this period, the total heat transfer sharply decreases with time.

Once the thermally unstable condition that develops the natural convection flow is properly achieved, the contribution from conduction to the total energy flux at the wall, is very weak, and the energy exchange process is mainly due to natural convection. It may be seen that during this time scale the total heat transfer increases with time. The change in slope in both of the curves is found to be coincident with the starting of the freezing process as may be seen from the solid fraction curves. The rapid decrease of the liquid core temperature to a value just above the PCM melting point terminates the above-mentioned time scale and brings the inward freezing with it.

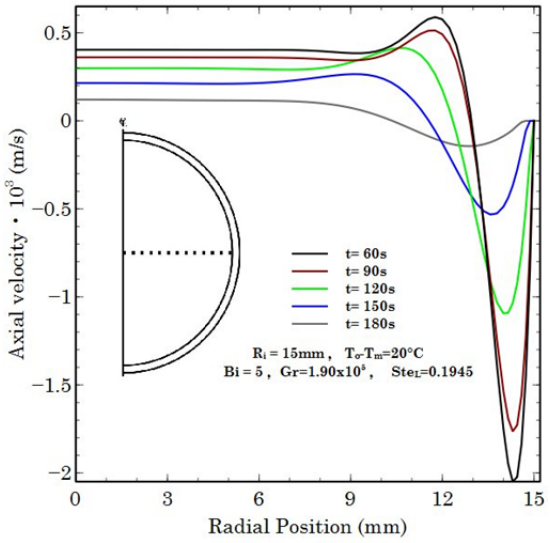

Figure 32 Velocity distribution along the horizontal radius of the shell for study case 5

The growing solid-phase resistance tends to impede the heat flow from the PCM to the outer wall and could be the responsible for the decrease of the total heat transfer at large times. As expected the contribution of thermal radiation enhances the energy interaction at the inner shell wall.

In order to provide a quantitative notion of the velocity magnitudes and the flow patterns developed in the melt layer during the early periods of the process, the velocity component in the vertical direction, along the horizontal radius of the capsule at different times is presented in Figure 32. The secondary figure has been included to show the locations where the velocity has been measured.

The flow structure is described as follows. A thin layer of fluid flows downward in the vicinity of the inner shell wall, where the maximum velocity is attained, and upward flow characterizes the fluid in the center of the capsule. As the driving temperature difference within the melt layer decreases with time (as seen in Figure 29) the natural convection flow loses its strength and consequently the velocities also decrease. A closer view of Figure 32 reveals that the thickness of both flows increases as the process proceeds. At 180s, the velocity magnitude was found to be significantly smaller as compared to the values at 60s. The effects of the initial superheating temperature on the solid fraction and the dimensionless energy transfer at the inner shell wall are presented in Figure 33. It may be seen from the bottom of the solid fraction curves that the larger the degree of superheating the longer to start the freezing.

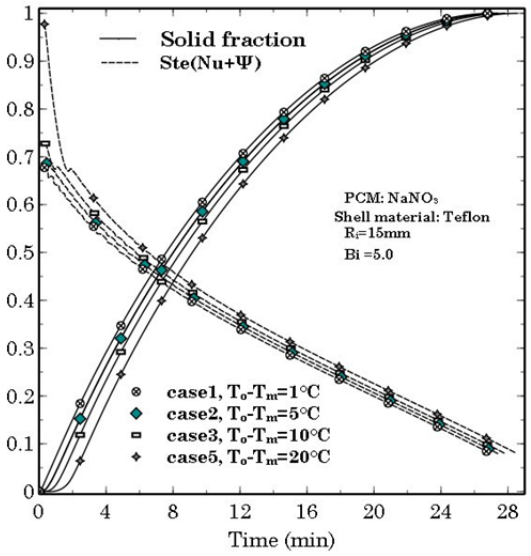

Figure 33 Influence of the liquid superheating on the thermal dynamics of the process

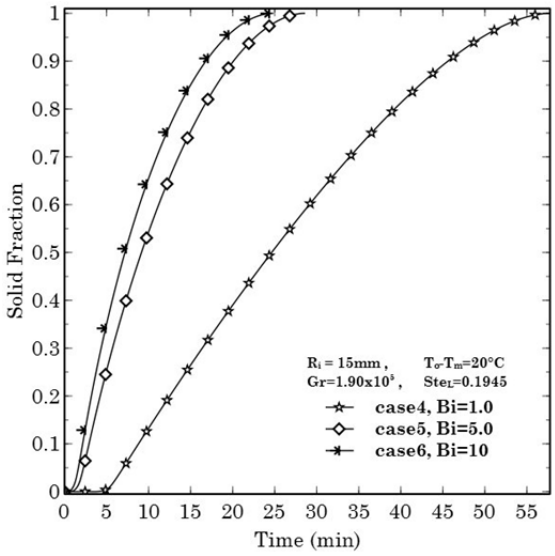

Figure 34 Influence of the Biot number on the solid fraction rate

Even though, the liquid superheat clearly affects the freezing dynamics early in the process. Once the energy transfer from the liquid phase to the solid/liquid interface has ceased, the remaining energy transport mechanisms are radiation and conduction within the solid phase which essentially remain unchanged under the analyzed thermal conditions of cases 1-3 and 5. This fact could be responsible for the small differences observed in all of the curves at the late stages of the process.

The influence of the external heat transfer coefficient on the solid fraction rate is depicted in Figure 34. The heat transfer coefficient values of 45.4, 226.7 and 453.5W/m^2K have been evaluated which correspond to Biot numbers equal to 1, 5 and 10 respectively. As expected a reduction in the solidification time was found with the increase of the Biot number. However, the time reduction was more pronounced in the case where Bi=1 as compared with the study cases where the Biot number was 5 and 10.

The effect of shell size on the solidification rate is presented in Figure 35. Three shell sizes have been analyzed with inner radius varying from 15 to 35mm. It may be observed that the smaller the capsule, the faster the solidification.

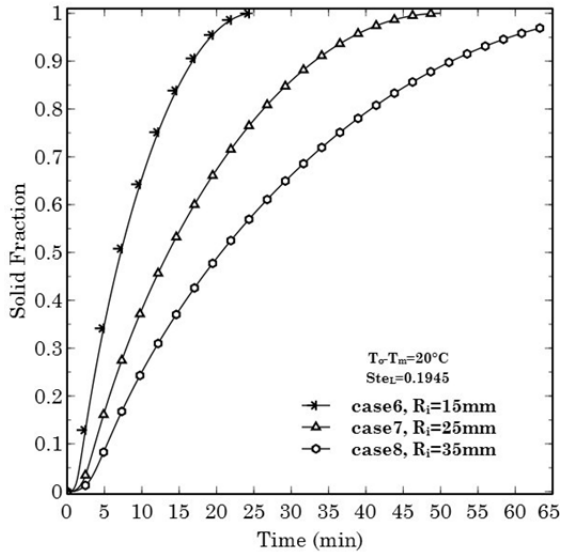

Figure 35 Influence of the shell size on the solid fraction rate

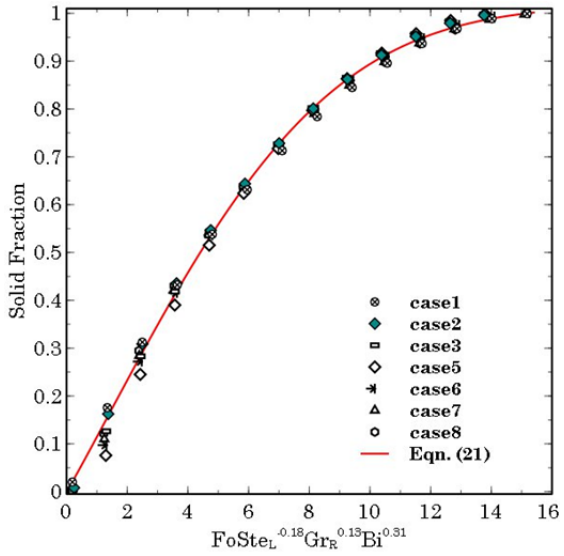

Figure 36 Solid fraction as a function of the controlling parameters

As shown in Figure 36, the predicted solid fraction for all the study cases, except for the study case 4, has been plotted as a function of a dimensionless group ($FoSte_L^a Gr_R^b Bi^c$) that takes into consideration the controlling parameters analyzed in this chapter. Equation (12) is proposed to correlate the solid fraction (SF) of the analyzed cases:

$$SF = 1.017erf[0.1\left(FoSte_L^a Gr_R^b Bi^c\right)^{1.04} \quad (21)$$

It was found that, for a=-0.18, b=0.13, c=0.31, all the data merged together in a single line. A small deviation from the proposed correlation is observed in the early stages of the process in study cases 5, 6 and 7 and it is related to the wide range considered for the Biot number, which controls the cooling rate at the beginning of the freezing. The proposed correlation seems valid in the following range of the controlling parameters: $0.0096 \leq Ste_L \leq 0.195$, $8.77x10^3 \leq Gr_R \leq 2.42x10^6$, $5 \leq Bi \leq 23.34$, $Pr \cong 9.0$.

CHAPTER 4[4]: MELTING AND FREEZING AT ELEVATED TEMPERATURES

The present chapter analyzes the interaction between the natural convection-driven melting and the radiation energy transport within the PCM solid and liquid phases at elevated temperatures ($>$ 800℃). It is presumed that under those operating conditions, radiative heat transfer becomes significant as compared to the other fundamental heat transfer modes. Consequently, the low thermal conductivity problem in the heat transfer during phase change can be overcome.

NaCl was selected as the PCM in this investigation because of its high latent heat of fusion and relatively low cost. Also, it's melting temperature ($800 - 802$℃) matches with the typical operating range of central receiver power plants. It has been reported by [109] that NaCl, is mostly transparent to thermal radiation in the wavelength range of interest ($1.5 \leq \lambda \leq 9.0\mu m$). Two approaches are used in this investigation to enhance the thermal radiation heat transfer in NaCl. In the first approach, the inner wall of the capsule has been lined with a high infra-red emissivity coating while in the second, highly absorptive nano particles were introduced into the PCM as dopants in order to increase the absorption of radiant energy. In the numerical model presented in this section, it is assumed that the additive particles dissolve into the PCM to form a homogeneous and isotropic substance. Based on that, the effect of the additive concentration on the system can be represented by changing the PCM absorption coefficient with the assumption that the higher the concentration, the larger the absorption value. Therefore, uniform and equal absorption and scattering coefficients have been defined for the solid and liquid phases of the PCM.

4.1. Formulation of the Melting Problem

The considered system is schematically shown in a cross-sectional view in Figure 24. It consists of an axisymmetric, two-dimensional representation of an opaque, gray and diffuse spherical shell of

[4] The content of this chapter has been submitted to the Applied Energy journal. A. R. Archibold, M. M. Rahman, D. Y. Goswami and E. K. Stefanakos, "The effects of radiative heat transfer during the melting process of a high temperature phase change material confined in a spherical shell," *Applied Energy*, 2014. In review. Permission is included in Appendix B.

inner radius R_i and thickness δ. The inner volume of the shell is completely filled with NaCl which can conduct heat as well as absorb, emit and scatter radiant energy. Initially, the PCM is solid at a temperature T_o and at a time t>0, the outer boundary surface is subjected to a uniform temperature T_w which is higher than the storage material melting temperature T_m. The contribution of the radiant energy transfer within the PCM is characterized by the absorption and the scattering coefficients κ_a and σ_s respectively, which are independent of temperature and the frequency in this study. A uniform and wavelength independent index of refraction ($n = 1.4$) for each PCM phase has been assumed in all the calculations based on the experimental measurements of Bloom and Peryer [110].

As described in section 3.1, the inclusion of participating thermal radiation in the mathematical model requires an additional term in the energy equation (as seen in Eqn. (17)). The extra term accounts for the radiative heat flux and is coupled with the radiation intensity through the equation of radiative transfer. The equation of radiative transfer for diffuse radiation and isotropic scattering in a spherically symmetric medium can be expressed as:

$$\frac{\mu}{r^2}\frac{\partial[r^2 I(r,\mu)]}{\partial r} + \frac{1}{r}\frac{\partial[(1-\mu^2)I(r,\mu)]}{\partial \mu} + (\kappa_a + \sigma_s)I(r,\mu) = \kappa_a I_b(T) + \frac{\sigma_s}{2}\int_{-1}^{1} I(r,\mu')d\mu' \qquad (22)$$

where $I(r,\mu)$ is the radiation intensity, which is a function of the position and direction, μ is the cosine of the angle between the direction Ω of the beam and the extension of the radius vector r, $I_b(T)$ is the intensity of a black body radiation at the temperature of the medium. The last term on the right hand side of equation (22) represents the variation in the radiation intensity in the medium, due to scattering from the incoming direction μ'. In the discrete ordinate method, the RTE is approximated by discretizing the entire incident solid angle using a finite number of ordinate directions and the corresponding weight factors [103, 104, 111, 106]. Therefore, the integrodifferential equation (22) is written for each ordinate and the integral term is replaced by a quadrature summed over each ordinate. Finally, the equation reduces to a discrete system of differential equations, sufficient to solve for the radiation intensity (I_i) at every location within the medium. The set of equations results in:

$$\frac{\mu_i}{r^2}\frac{\partial[r^2 I_i]}{\partial r}+\frac{1}{r}\frac{\partial[(1-\mu^2)I]_{\mu=\mu_i}}{\partial \mu}+(\kappa_a+\sigma_s)I_i=\kappa_a I_b+\frac{\sigma_s}{2}\sum_{i=1}^{n} w_i I_i \tag{23}$$

where the subscript i denotes the quadrature points (ordinate directions) and w_i is a weighting factor. Once the radiation intensity is known, the local radiative heat flux (q_r) can be determined based on the following expression:

$$q_r = 2\pi \int_{-1}^{1} I(r,\mu)\mu d\mu = 2\pi \sum_{i=1}^{n} \mu_i w_i I_i \tag{24}$$

In order to solve the governing equations, the control volume technique, which employs an implicit scheme based on the SIMPLE (Semi-Implicit Method for Pressure-Linked Equations) algorithm [94], was used. Commercially available software Ansys/Fluent v12 was employed for the calculations.

The second order upwind scheme was employed to discretize the momentum equations while the PRESTO (Pressure Staggering Option) scheme was adopted for pressure correction via the continuity equation. The energy equation was discretized using the First Order Upwind scheme. The under-relaxation factors for pressure, density, body force, momentum, liquid fraction update, energy and the radiative transfer equation were 0.4, 0.7, 0.7, 0.6, 0.8, 1 and 1 respectively. Scaled absolute residuals of 10^{-4}, 10^{-3} and 10^{-6} were set as the convergence criteria for continuity, velocity components and energy, respectively. The domain was discretized based on a structured grid consisting of 8616 cells with a refined mesh distribution in the vicinity of the inner shell wall. In order to obtain appropriate convergence of the solution, the Navier-Stokes equations were disabled during the early periods of the process until the first melt layer was created.

4.2. Validation of the Numerical Solution

The influence of the grid size on the accuracy of the numerical solution has been analyzed by the time dependent distribution of two properties within the domain. The mass average solid fraction and the center point dimensionless temperature (Θ_n) have been plotted (as seen in Figure 37) as a function of the dimensionless time (SteFo) for different grid sizes for the case with $R_i = 25mm$ and $T_w - T_m = 25$°C.

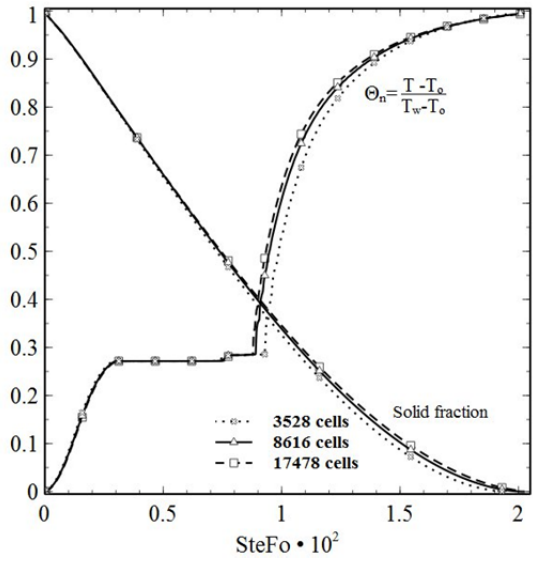

Figure 37 Influence of the grid size on the thermal variables of the model

From the solid fraction curves of Figure 37, it is observed that faster melting is predicted when a coarse grid is used. It is also shown that the solution tends to the same value when the element size decreases. Even though, the grid independence test has been performed in the capsule with $R_i = 0.025m$, its validity can be extended to the study cases with different capsule sizes, because of the fact that the grid element size was kept approximately constant in all the calculations. To do that, the base computational domain (capsule with $R_i = 0.025m$) has been subdivided into five different zones which have been geometrically parameterized based on the shell dimensions and then used to estimate the number of elements needed for the outer shell sizes. A grid distribution of 8616 cells, where the minimum and maximum element sizes are $0.33x0.22mm$ and $0.25x0.56mm$ (width x height) respectively, was found sufficient to achieve independence of the solution.

The accuracy of the numerical approach implemented to solve the radiative heat transfer equation has been tested by solving the problem reported by Viskanta and Merriam [51]. The problem consists of an absorbing, emitting and scattering gray medium confined in the space between two black, diffuse, concentric spherical surfaces. Uniform temperatures T_1 and T_2 are imposed on inner and outer surfaces respectively, with $T_1 > T_2$.

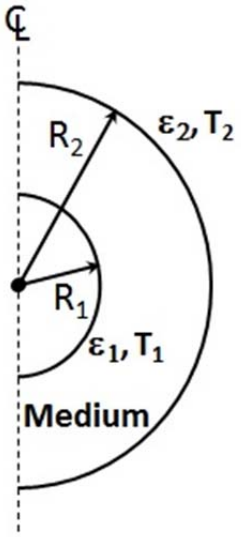

Figure 38 Schematic of the concentric spheres system

Table 5 Dimensionless total and radiative heat fluxes

τ_2	Inner wall		Outer wall	
	Ψ_1	Φ_1	Ψ_2	Φ_2
1	4.257[a]	0.807[a]	1.064[a]	0.202[a]
	4.252[b]	0.805[b]	1.063[b]	0.201[b]
2	6.070[a]	0.709[a]	1.517[a]	0.160[a]
	6.076[b]	0.733[b]	1.519[b]	0.159[b]
3	7.408[a]	0.618[a]	1.852[a]	0.127[a]
	7.462[b]	0.620[b]	1.865[b]	0.129[b]
4	8.440[a]	0.549[a]	2.110[a]	0.106[a]
	8.511[b]	0.551[b]	2.128[b]	0.107[b]
10	11.341[a]	0.322[a]	2.834[a]	0.052[a]
	11.455[b]	0.319[b]	2.864[b]	0.052[b]

a) Predictions from the present model
b) Values reported in ref. [51]

A schematic of this problem is shown in Figure 38. The steady-state, one-dimensional, axisymmetric energy conservation equation was solved numerically using the control volume technique, while the DOM [104, 102] was used to solve the RTE.

Numerically predicted dimensionless total (Ψ_n) and radiative (Φ_n) heat fluxes at each surface of the system for different optical depths (τ_2) obtained from our simulations of the same problem are presented in Table 5. It is shown that with the increase of the optical thickness (τ_2), the radiant heat flux decreases and the interaction between the two energy transport modes generates an increase of the conductive flux. In this system, a strongly absorbing medium is heated essentially at the inner surface increasing the emission of heat that needs to be transported by conduction because it cannot be absorbed within the medium.

The effect of the inner sphere radius on the temperature distribution of the system is depicted in Figure 39. The ratio between the cold and hot temperatures is plotted against a normalized distance between the spherical shells, It may be seen that, as ξ increases, the space between the shell decreases and the temperature variation across the system becomes more linear. In the figure, the numerical solutions reported by [51] are also displayed and show a reasonably good agreement with the present results.

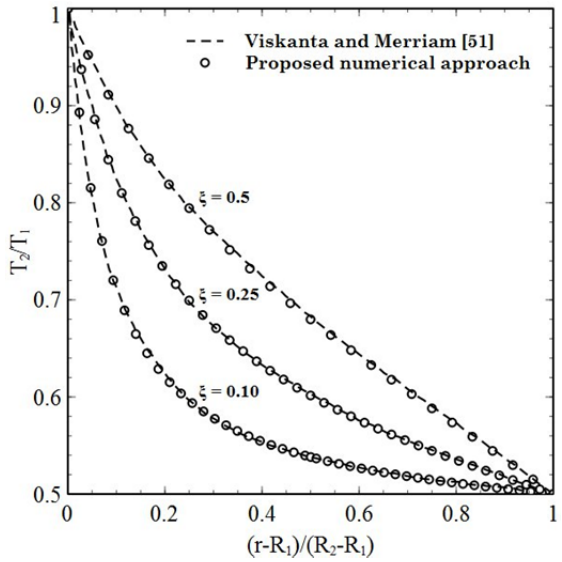

Figure 39 Effect of the geometric parameter ($\xi = R_1/R_2$) on the temperature distribution

The theoretical model was validated by experimental measurements of the temperature response of standard grade NaCl by the American Chemical Society (ACS), contained in a closed porcelain crucible during the sensible heating and phase change processes. A muffle furnace was used to thermally cycle the sample while continuous temperature measurements at the center of the sample and the wall of the porcelain crucible, were recorded. Material compatibility issues between the thermocouple probe and the salt were anticipated because of the presence of air at elevated thermal conditions. The corrosion of the thermocouples and consequently, its effect on the data reliability, was overcome by using ungrounded K-type thermocouples with an Inconel sheath.

In the numerical solution, the wall temperature profile obtained from the experiments was used as a transient boundary condition for the container outer surface. Based on that, the temperature response of the PCM at 10mm from the inner bottom surface of the crucible in the axial line has been calculated. Reasonably good agreement was found.

A detailed description of the experimental procedure and the comparison between the numerical and experimental results has been reported by Archibold et al. [112].

4.3. Results and Discussion for Melting

Ten different cases were analyzed in this study as summarized in Table 6. The effect of optical thickness (τ) by changing the absorption coefficient (κ_a), on the melting process for a constant capsule size, is considered in cases 1 to 4. It should be pointed out that the first case was chosen as the limiting case in which $\kappa_a = 0$ and the emissivity (ε) at the inner surface of the shell was also equal to zero. It may be noticed that the Planck number ($Pl = \kappa(\kappa_a + \sigma_s)/4n\sigma\bar{T}^3$) also varies in these study cases. In cases 5 and 6, the effects of optical thickness and Grashof number (Gr) are analyzed by manipulating the capsule size. In the present model it was assumed that the mean beam length is the inner radius of the shell, therefore the optical thickness can be calculated from the equation: $\tau = (\kappa_a + \sigma_s)R_i$, where σ_s is the scattering coefficient. Cases 7 and 8 have been included in order to evaluate the combined influence of the Grashof and Stefan numbers on the thermal performance of the system, as the outer wall temperature (T_w) changes. The effect of scattering albedo ($\omega = \sigma_s/[\kappa_a + \sigma_s]$) is analyzed in cases 9 and 10. The present study is mainly directed to the analysis of the energy interactions that can occur in an attenuating and emitting thermal storage medium.

Table 6 Analyzed parameters in melting with participating radiation

$case$	$R_i(m)$	ΔT(°C)	κ_a	σ_s	τ	Pl	Gr_R	Ste
1	0.02	25	0	0	0	0	$1.7\text{x}10^6$	0.063
2	0.02	25	25	0	0.5	0.03	$1.7\text{x}10^6$	0.063
3	0.02	25	100	0	2.0	0.13	$1.7\text{x}10^6$	0.063
4	0.02	25	200	0	4.0	0.25	$1.7\text{x}10^6$	0.063
5	0.025	25	200	0	5.0	0.25	$3.3\text{x}10^6$	0.063
6	0.03	25	200	0	6.0	0.25	$5.7\text{x}10^6$	0.063
7	0.02	20	100	0	2.0	0.13	$1.3\text{x}10^6$	0.050
8	0.02	15	100	0	2.0	0.13	$9.9\text{x}10^5$	0.038
9	0.02	25	10	15	0.5	0.03	$1.7\text{x}10^6$	0.063
10	0.02	25	10	90	2.0	0.13	$1.7\text{x}10^6$	0.063

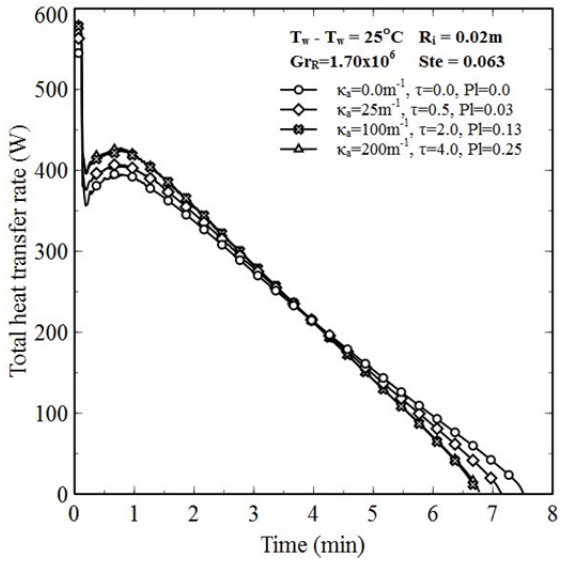

Figure 40 Influence of the absorption coefficient on the total heat rate at the inner wall

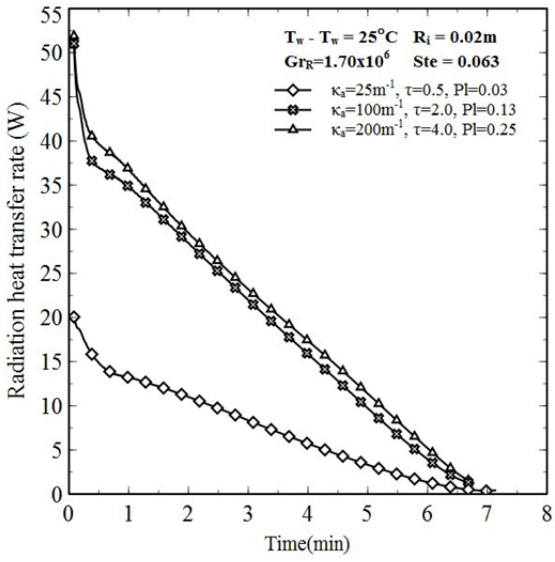

Figure 41 Influence of the absorption coefficient on the radiative heat rate at the inner wall

The timewise variation of the total and radiant heat transfer rates at the inner surface of the shell are depicted in Figure 40 and Figure 41. Four cases with different absorption coefficient values have been used to analyze the influence of the optical thickness on the heat transfer at the wall. It may be observed from the ordinate values of each figure that, the contribution of the radiant heat to the total energy exchange is one order of magnitude smaller. A possible explanation is that, under the investigated thermal conditions ($T_m/T_w = 0.977$) the contribution of the participating thermal radiation does not play a first order role during the melting process as the energy transfer by natural convection does.

Even though, the overall contribution of the radiant heat flux on the net energy transport process was found to be small, the increase of the medium optical thickness increases the radiant heat transfer distribution at the inner wall, particularly when the absorption coefficient changes from $25m^{-1}$ to $100m^{-1}$, as seen in Figure 41. These differences on the radiant heat flux are responsible for the trend observed in Figure 40, where the net heat rate distribution of the limiting case is slightly smaller than predicted for the study cases where thermal radiation was included. It should be noticed that the trend followed by all the curves in Figure 40 also characterizes the behavior of the heat transfer distribution during the melting process at lower temperatures (as seen in Figure 8).

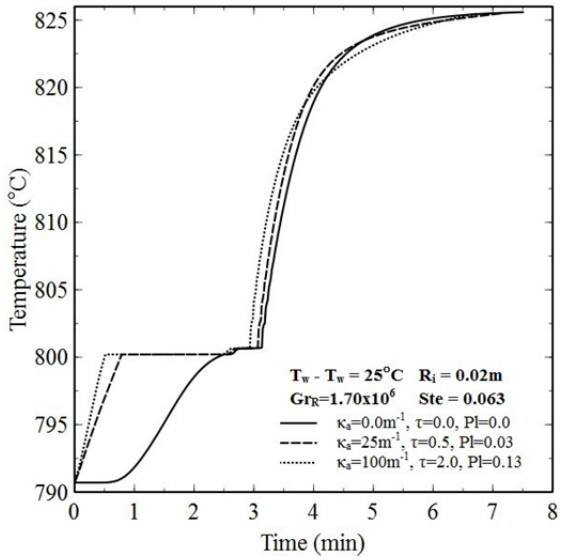

Figure 42 The effect of κ_a on the center point temperature response

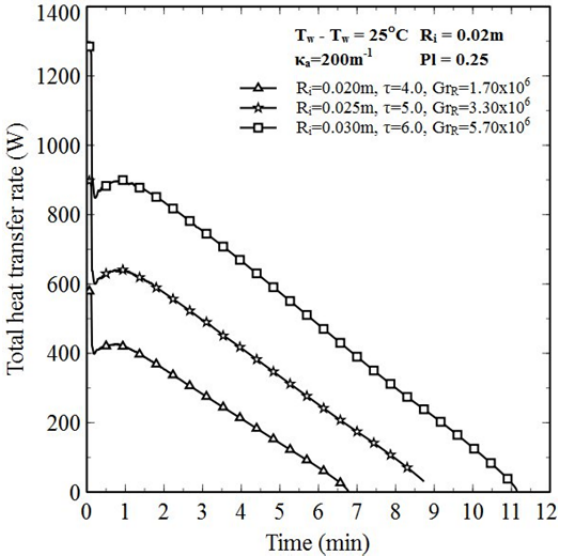

Figure 43 The effect of R_i on the total heat rate at the inner wall

Therefore, no attempt to describe the dynamics of Figure 40 is made, because it has been previously discussed in section 2.3.

Figure 42 depicts the average temperature of the center point of the capsule during the process. Each curve can be subdivided into three different zones: the solid phase sensible heating portion ($790.7℃ \leq T \leq 800.2℃$), the phase change ($800.2℃ \leq T \leq 800.7℃$) and liquid phase sensible heating ($800.7℃ \leq T \leq 825.7℃$). Special attention should be paid to the temperature response of the system during the solid phase heating. It can be observed that the time to reach 800.2℃ at the center point is 78.6% faster in case 3 ($\kappa_a = 100m^{-1}$) as compared to the study case with no radiation. The results show that the presence of radiation during this period significantly enhances the heating process, based on the fact that, during this period the process is characterized by radiation and conduction heat transfer with radiation being the dominant heat transfer mode.

Figure 43 illustrates the combined influence of the Grashof number and the optical thickness on the total heat transfer rate at the inner surface of the shell. Three different shell sizes have been analyzed ($R_i = 20, 25\ and\ 30mm$). As expected, by increasing the shell size, the total heat transfer rate increases. The larger the capsule, the larger the available heat transfer area for the energy transfer.

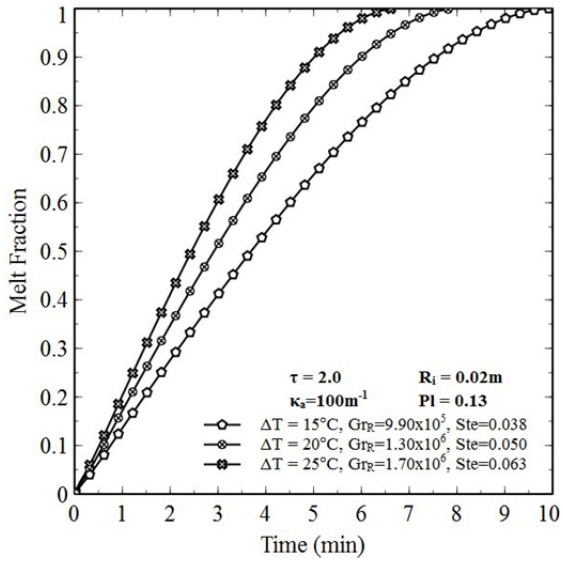

Figure 44 The effect of T_w on the melt fraction rate

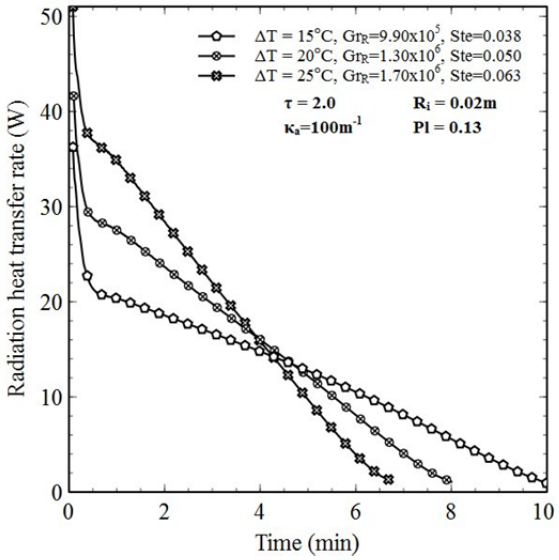

Figure 45 The effect of T_w on the radiant heat rate at the inner wall

Also, with the increase of the capsule size, the Grashof number increases as well, enhancing the contribution of natural convection. Simultaneously, the optical thickness of the medium becomes larger by increasing the path length over which radiation must travel. Under these conditions, the neighboring elements of the inner wall surface are mainly influenced by radiant energy interactions.

The effect of the shell outer surface temperature was examined by analyzing cases 3, 7 and 8. A 20 mm inner radius pellet was subjected to three different boundary condition values above the PCM melting temperature. The predicted liquid mass fraction of the aforementioned cases is depicted in Figure 44. As expected, faster melting was achieved with higher values of the shell outer wall temperature. The melting time was 20% shorter for Case 7 (T_w-T_m=20°C) and 33% shorter for Case 3 (T_w-T_m=25°C) when compared to the corresponding value of case 8 (T_w-T_m=15°C). The influence of the outer wall temperature on the radiant heat transfer rate at the shell inner wall is shown in Figure 45. During the period, $0 \leq t \leq 4.0$ min, the radiation heat transfer rate increases with an increase of the outer wall temperature. However, after this interval all the curves cross each other and an inverse trend is observed. The thermal equilibrium is reached sooner in the case with a high wall and PCM melting temperature difference (higher Stefan and Grashof numbers).

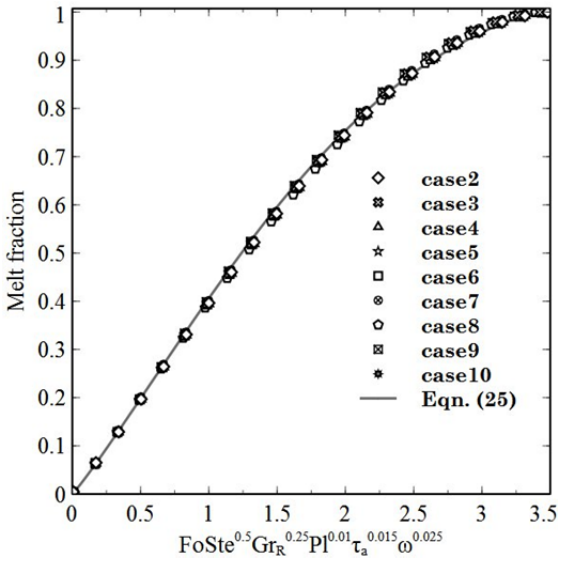

Figure 46 Melt fraction as a function of the controlling parameters

The predicted melt fraction for all the analyzed study cases has been plotted as a function of the controlling parameters in Figure 46. A dimensionless group that includes the Fourier, Grashof, Stefan and Planck numbers, as well as the absorption optical thickness, ($\tau_a = \kappa_a R_i$) and single scattering albedo has been created and used as the abscissa in the graph. The following equation is proposed to be used to correlate the melt fraction of all the analyzed cases:

$$MF = 1.07erf\left[0.35\left(FoSte^{a}Gr_R^{b}Pl^{c}\tau_a^{d}\omega^{e}\right)^{1.08}\right] \tag{25}$$

It was found that for $a = 0.5,\ b = 0.25,\ c = 0.01,\ d = 0.015\ and\ e = 0.025$, all the data merged together in a single line. A dimensionless group that includes the contribution of thermal radiation at the inner wall of the shell has been defined as:

$$\frac{NuSte^{a}}{Gr_R^{b}Pl^{c}\tau_a^{d}\omega^{e}} \tag{26}$$

The above quantity includes the modified Nusselt number which has been calculated based on the predicted total heat transfer rate at the inner wall. The aforementioned group has been plotted, for each study case, as a function of the same dimensionless number used in Eqn. (25) in Figure 47. All the results practically merge into a single curve for the exponents:

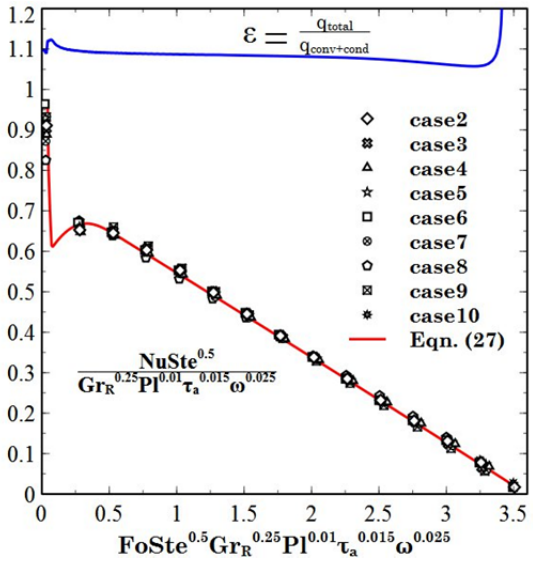

Figure 47 Nusselt number as a function of the controlling parameters

$a = 0.5,\ b = 0.25,\ c = 0.01,\ d = 0.015\ and\ e = 0.025$. The following piecewise correlation for the Nusselt number dimensionless group is proposed:

$$\frac{NuSte^a}{Gr_R^b Pl^c \tau_a^d \omega^e} = \begin{cases} 1.472 - 11.89\xi & 0.04 \le \xi < 0.08 \\ 0.5exp(-2.5\xi^{2.4}) + \sin(0.07 + 0.55\xi), & 0.08 \le \xi < 0.52 \\ 0.753 - 0.205\xi - 0.0012\xi^2, & 0.52 \le \xi \le 3.5 \end{cases} \quad (27)$$

where: $\xi = FoSte^a Gr_R^b Pl^c \tau_a^d \omega^e$. The range of validity of the above correlations can be defined as: $0.038 < Ste < 0.063$, $9.9\,x\,10^5 < Gr_R < 5.7\,x\,10^6$, $0.03 < Pl < 0.25$, $0.5 \le \tau_a \le 6.0$, and $0.6 \le \omega \le 0.9$.

In order to quantify the contribution of the participating thermal radiation during the melting process, an enhancement factor (ϵ) has been defined as the ratio between the total and the combined conduction and convection heat transfer rates. This quantity may be used to take into consideration the influence of thermal radiation in the thermal modeling of storage tanks containing encapsulated PCMs. In these models, the effective thermal conductivity method is commonly used to estimate the energy transfer process between the heat transfer fluid and the PCM capsule. Figure 47shows the enhancement factor for case 3.

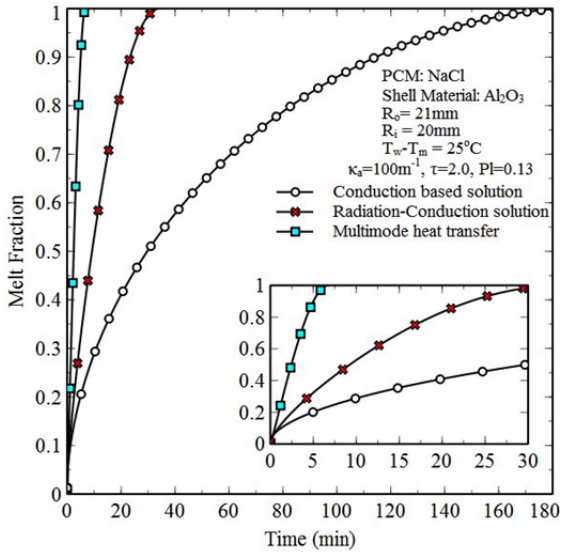

Figure 48 Predicted melting rate in the absence of free convection

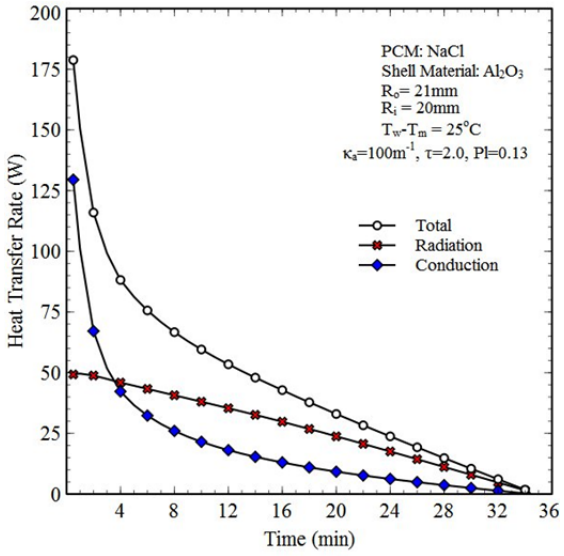

Figure 49 Heat transfer distribution at the inner wall in the absence of free convection

In order to extend the discussion about the relative significance of thermal radiation over conduction in the absence of natural convection, separate calculations have been performed to predict the melting process of NaCl confined in a spherical capsule. In the calculations, heat transfer during phase change has been analyzed considering heat conduction as the sole energy transport mode as well as the simultaneous radiation and conduction. Figure 48 shows the predicted melting rate for both models under the same operating conditions. Also, in the figure, the results from the natural convection dominated process (study case 3) have been included in blue color. A secondary graph has been included in Figure 48 with a smaller range in the abscissa in order to facilitate the comparison between the models with faster melting times.

It may be seen that, for the same shell size, thermal boundary conditions and PCM, the simultaneous interaction of thermal radiation with conduction decreases the melting time by a factor of five as compared with the pure conduction solution. The same reduction level is observed when natural convection participates in the process, and it is compared with the combined radiation and conduction model. Figure 49 depicts the time wise variation of the radiative and conductive energy transport contributions at the shell inner wall for the combined radiation and conduction model.

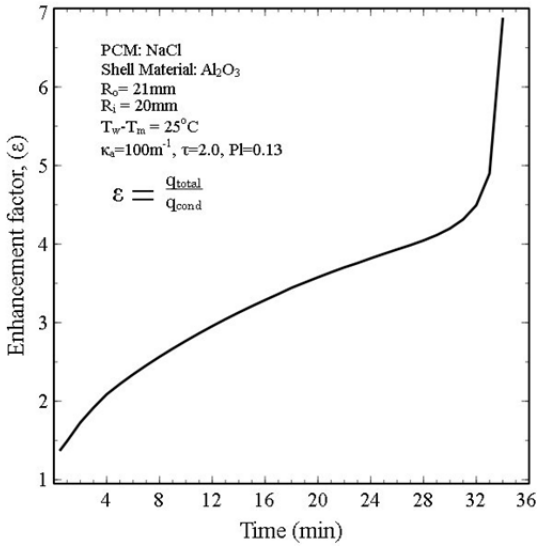

Figure 50 Enhancement factor during melting in the absence of free convection

As expected, at the wall and at t=0, the conductive heat is maximum because of the highest temperature difference within the system. As the temperature gradient decreases with time, the energy transferred to the wall by conduction also reduces. The monotonic decrease with time that characterizes the pure conduction melting is observed. On the other hand, radiative heat transfer is characterized by a linear distribution during the process that rapidly exceeds the contribution of conduction until the end of the process. Figure 50 shows the enhancement factor that the participating thermal radiation exerts over the pure conduction solution, at the inner shell wall. The factor (ϵ) has been calculated based on the values reported in Figure 49, for the combined radiation-conduction model. It may be observed that higher values are obtained as compared with the same factor in the presence of natural convection.

In order to graphically illustrate the melting process when natural convection is present along with conduction and radiation, the predicted solid fraction, streamlines and temperature contours for study case 5 are presented in composite diagrams illustrated in Figure 51. A 2-D, coordinate system has been used to locate each plot in the figure and provide a quantitative measure of the location and shape of the melting interface. The predicted solid/liquid interface evolution of the combined radiation and conduction model is presented in Figure 51h. The classical concentric ring shape solution is observed which may be applicable in situations where the gravity is not present.

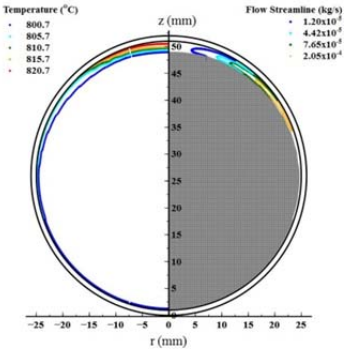

a) 20s

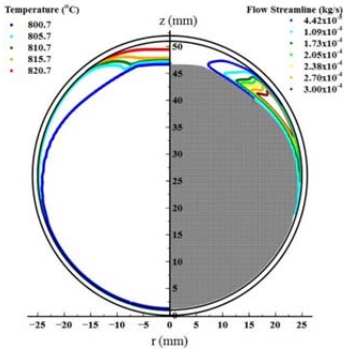

b) 40s

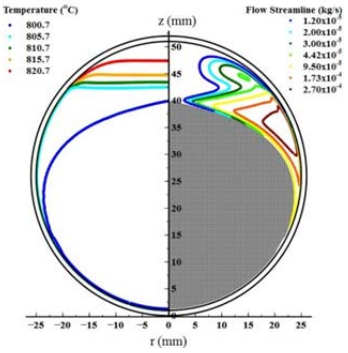

c) 80s

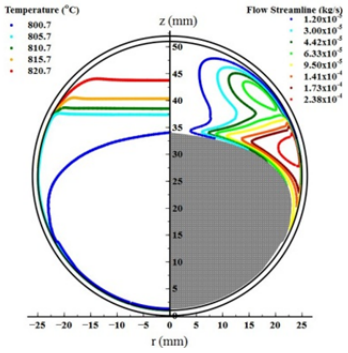

d) 120s

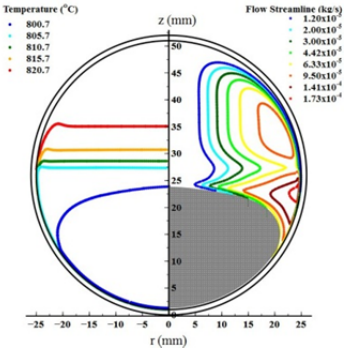

e) 220s

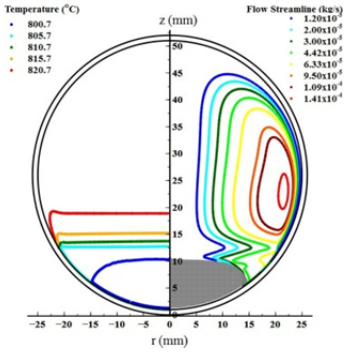

f) 400s

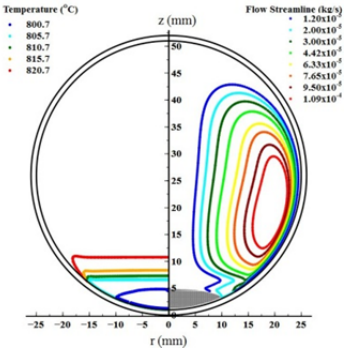

g) 480s

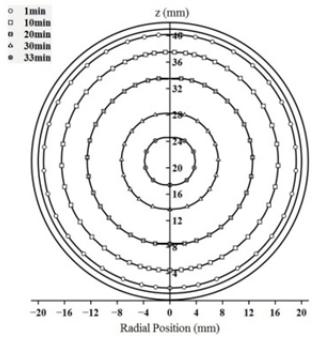

h)

Figure 51 Predicted evolution of the melting process for study case 5

4.4. Results and Discussion for Solidification

Simultaneous conduction, convection and thermal radiation have been analyzed during the freezing of a non-opaque, gray phase change material (PCM) encapsulated in a closed spherical container and heated to relatively high temperatures (782≤T≤822℃). In contrast to the conventional conduction-dominated model of the single phase Stefan problem, in the present study the influence of the participating thermal radiation and the buoyancy induced natural convection within the melt layer is highlighted and analyzed. The effect of the shell size has also been analyzed.

A two-dimensional, axisymmetric, transient model has been solved numerically. The considered system is schematically shown in a cross sectional view in Figure 52. It consists of an opaque, gray and a diffuse spherical shell of inner radius R_i and wall thickness δ. Initially, the shell internal volume is completely filled with liquid PCM, at temperature $T_o = 822$℃, which is higher than the storage material melting temperature T_m. At time t>0, the outer boundary surface, whose emissivity was set to unity, is subjected to a convective boundary condition characterized by a heat transfer coefficient h_∞ and a free stream temperature $T_\infty = 782$℃, which is lower than T_m. The PCM is treated as a semitransparent, gray, medium being emitting and absorbing. Temperature dependent density within the liquid PCM has been considered only in the body force terms of the momentum equations to account for natural convection in the melt layer. The scattering of thermal radiation has been neglected. The melting of NaCl takes place in the interval between 801℃ and 802℃.

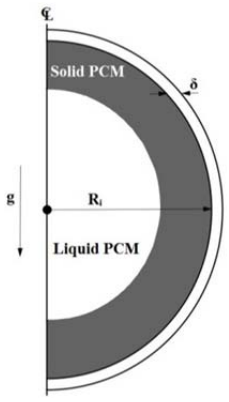

Figure 52 Schematic representation of the NaCl freezing model

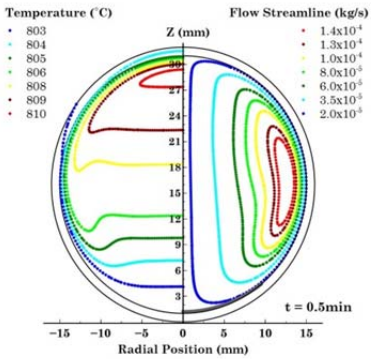

a) 30s

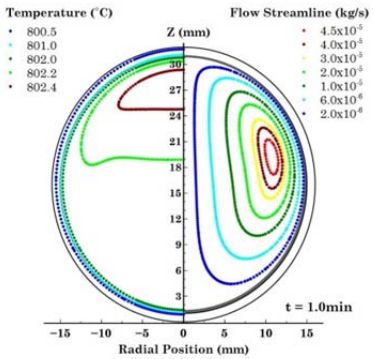

b) 60s

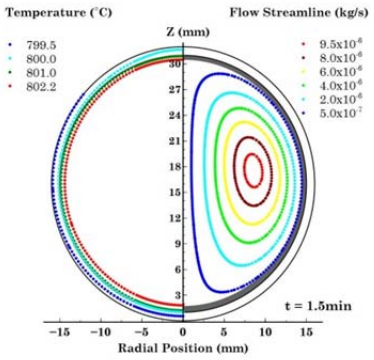

c) 90s

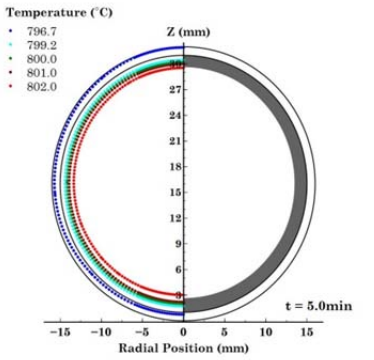

d) 300s

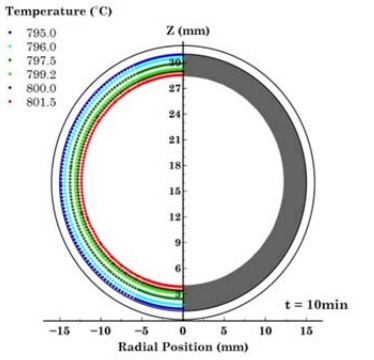

e) 600s

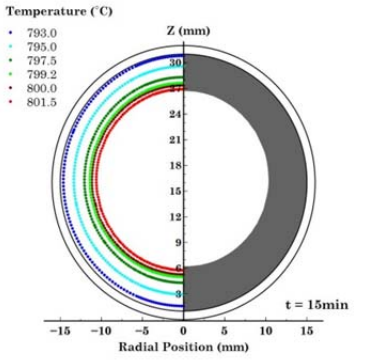

f) 900s

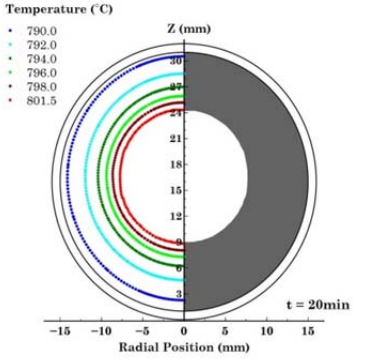

g) 1200s

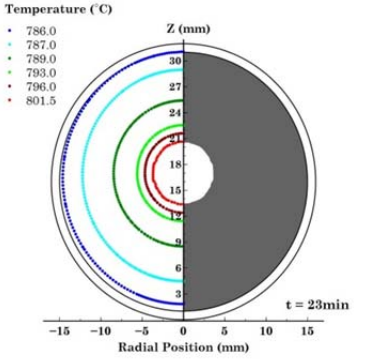

h) 1380s

Figure 53 Evolution of the NaCl freezing process

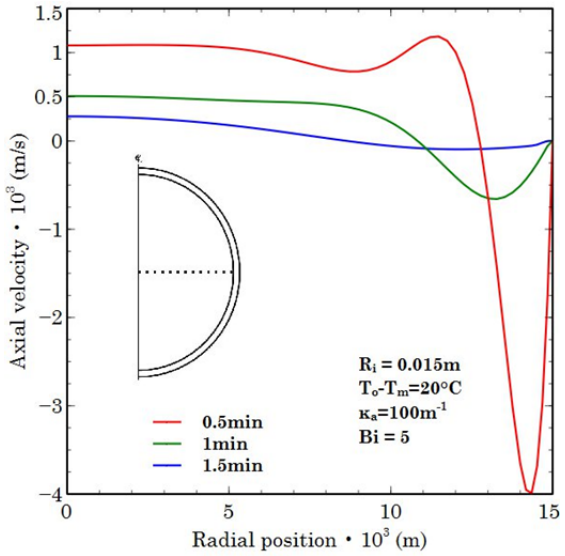

Figure 54 Velocity distribution along the horizontal radius at elevated temperatures

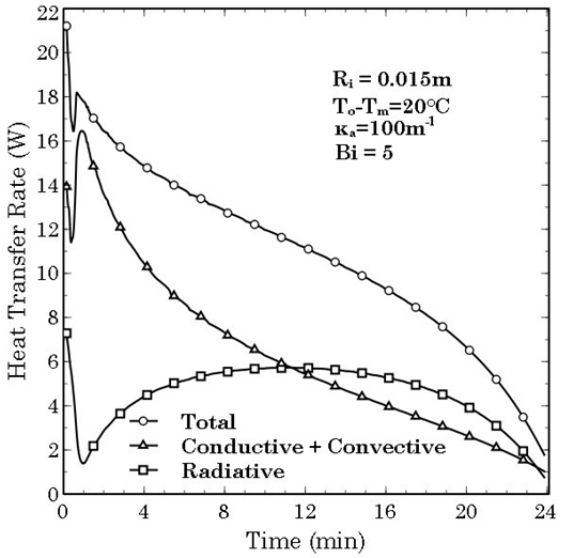

Figure 55 Heat transfer distribution at the inner shell wall at elevated temperatures

Predictions of the evolution of the solidification process at various time instants are presented in Figure 53. Moreover, the vertical velocity component along the horizontal radius of the capsule during early times is presented in Figure 54.

In the following discussion, the information presented in Figure 53 and Figure 54 is used to describe the trend followed by the time wise variation of the radiative and conductive-convective heat transfer through the shell inner wall, shown in Figure 55. During the first 30s, the combined conduction-convection heat transfer decreases, suggesting that the heat is mainly transported by conduction through the shell wall. As discussed in section 3.3, the reason is that; initially the melt layer is stagnant and it takes some time to develop a thermally unstable condition that drives the buoyancy induced flow.

Once this condition is developed, heat is transferred from the melt layer to the outer wall by free convection through the recirculating flow. Consequently, the combined conduction-convection heat transfer rate is expected to increase during this period. From Figure 55, it can be observed that, during the period from 30s to 60s the energy contribution from conduction and convection increases. The evidence that support the aforementioned trend is the circulating flow represented by the streamline contours at the right-hand side of Figures 53a and 53b.

Additionally, the high-velocity magnitudes reported in Figure 54 during the same period (30s-60s) may be used to support the trend. Essentially, during this time scale, natural convection heat transfer dominates the energy transfer through the shell wall by the fluid motion, thereby arresting the decrease of the temperature gradient in the vicinity of the inner wall.

After 60s, the temperature near the inner wall reaches the phase change temperature and the first layer of solid PCM is created. Consequently, the temperature gradients that originally induced the buoyancy flow are no longer present. As a result, the combined conduction-convection heat transfer rate is characterized by monotonic decrease with time, associated with the pure conduction behavior of the single phase Stefan problem. Figure 54 shows that, after 60s, the velocity magnitude across the liquid core is close to zero. Also the left hand side of Figure 53c, illustrates the concentric ring shape temperature contours in the vicinity of the inner wall.

Attention will now be turned to describe the trend followed by the radiative heat transfer rate. Initially, the radiation transfer rate starts from a maximum value, because, the initial temperature of the system is the highest in the process. The emissive power at the inner surface of the shell is a function of temperature. As discussed previously, the temperature at the vicinity of the inner shell quickly decreases to a value close to the PCM melting temperature within the first 60s. Consequently, the sharp decrease of the radiation transfer rate observed during this period is fully expected.

After 60s and until the end of the freezing, the inward solidification changes the process dynamics by incorporating an absorbing media that continuously increases its path length (solid phase) and an emitting media that continuously shrinks in size (liquid phase). By definition, the ability of a path length to attenuate radiation of a given wavelength is the optical thickness (τ). Under the analyzed conditions (uniform medium with absorption coefficient independent of temperature) the optical thickness depends directly on the extinction coefficient and the thickness of the medium. Since the extinction coefficient for the whole PCM is uniform ($100m^{-1}$) then the absorption of radiation intensity along the path is controlled by the thickness of the region, in this case, the solid phase.

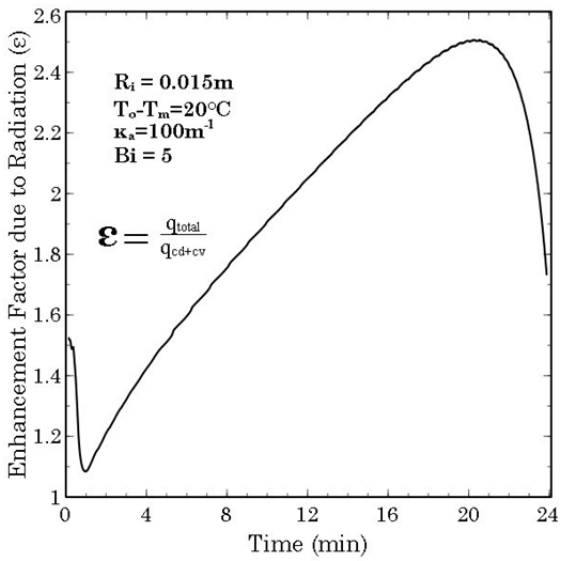

Figure 56 Enhancement factor during freezing of NaCl

Consequently, if the thickness of the solid phase is smaller than the attenuation distance (distance traveled by radiation intensity before being absorbed or scattered within the medium), then the thermal radiation can pass through it and reach the inner surface of the shell. Therefore, the increase of the radiation heat transfer rate with the time, from 1minute to 10 minutes is fully expected.

As the solidification process proceeds, the solid phase increases its size, and the medium becomes optically thick. Consequently, the thermal radiation emitted from the liquid phase is attenuated within the solid phase at some point before it reaches the inner surface of the shell. Therefore, the radiation heat transfer rate, at that location, decreases with time. It should be noticed that, even though the radiation heat transfer rate decreases with time during this period, its absolute value is higher than the contribution from conduction.

Figure 56 shows the enhancement factor of radiation heat transfer over the combined conduction-convection energy transports at the inner shell wall. It may be observed that, except for the early periods of the process where natural convection is the dominant heat transfer mechanism and the latest stages where the thermal radiation that arrives at the inner surface decreases, the enhancement factor continuously increases from 1.1 to 2.5.

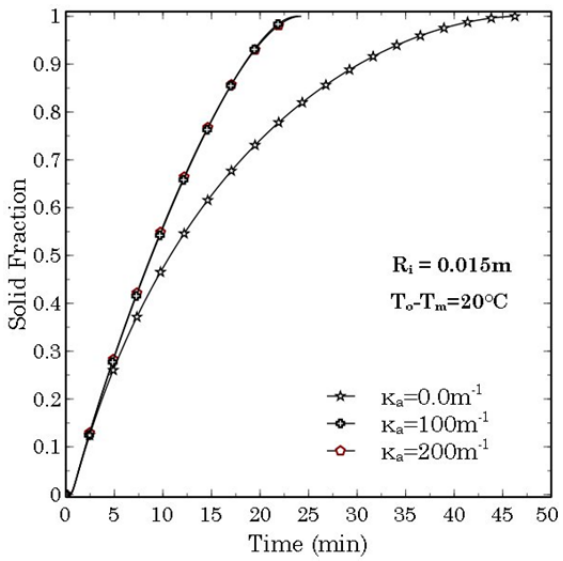

Figure 57 Influence of the absorption coefficient on the solid fraction rate

The influence of the PCM absorption coefficient (κ_a) on the freezing rate is presented in Figure 57. It can be inferred from the figure that, the solidification time decreases 48.4% as the absorption coefficient increases from 0 to $100m^{-1}$. A fraction of the emitted radiation intensity from the liquid layer is attenuated by absorption in the solid medium path length which results in faster cooling of the liquid PCM and therefore faster freezing. No significant difference was observed in the melt fraction rate when the absorption coefficient changes from 100 to $200m^{-1}$.

CHAPTER 5: MULTI CAPSULE MODEL

5.1. Introduction

In previous chapters, primary attention was directed to analyze the influence of energy transport mechanisms on melting and solidification of a confined storage material at different operating temperatures. Chapter 2 outlined the heat transfer analysis during melting of a storage material, in partially and completely filled capsules. The corresponding analysis during the freezing process was analyzed and discussed in chapter 3. Chapter 4 treated the role of thermal radiation in melting and solidification of a PCM at elevated temperatures (+800℃). However, the aforementioned analysis was limited to the thermal characterization of a single constituent storage module rather than an entire storage system.

A practical scenario of the analyzed thermal storage system consists of an arranged porous bed of capsules held in a cylindrical container through which a heat transfer fluid flows and transports energy to or from the PCM material contained within the capsules. Figure 58 shows a sectional view of the system.

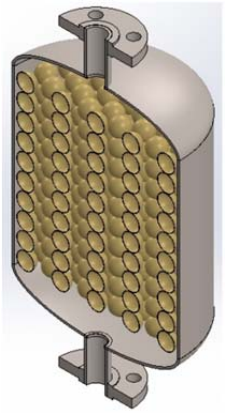

Figure 58 Schematic representation of the packed bed heat exchanger

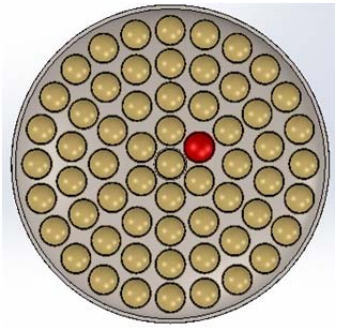

Figure 59 Radial section of the system showing the concentric distribution

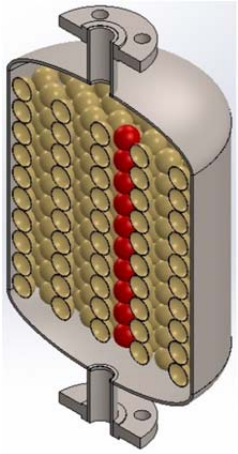

Figure 60 Axial section of the system showing the vertical distribution

In addition to experimental studies, numerical analysis based on the enthalpy method, apparent heat capacity technique and dispersion model have been widely used in the study of melting and freezing of an energy storage material confined in this type of heat exchangers. Some of them are listed in the following references [113, 16, 114, 115, 116]. However, the missing characteristic in all of them is the precise consideration of the simultaneous energy transport modes inside the capsule that control the PCM melting or solidification, due to forced convective energy flow from the heat transfer fluid at the outer capsule wall.

A simplified model for the thermal assessment of a packed bed heat exchanger by including simultaneous conduction, natural convection and thermal radiation within the energy storage material, as well as, forced convection at the outer shell surface is presented in this chapter. The influence of the inlet mass flow rate and inner shell surface emissivity on the melting dynamics of the process was analyzed.

5.2. Physical Situation and Model Assumptions

The following assumptions are made to simplify the mathematical model. (1) The capsules are oriented concentrically and vertically along the radial and axial directions (as seen in Figures 59 and 60). (2) Fluid flow distribution is uniform along the radial direction of the system. (3) Axial heat conduction due to contact between the capsules is negligible. This assumption follows from the fact that the capsules have a point contact.

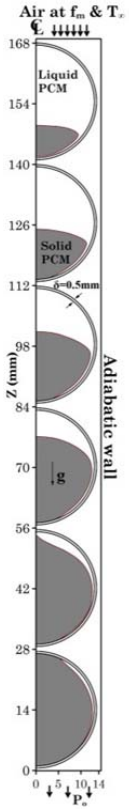

Figure 61 Schematic of the multi-ball model.

Also, a uniform separation distance of 1mm between the capsules was assumed. (4) The heat loss from the storage tank to the surroundings is assumed to be negligible. Thus, an insulated boundary condition was assumed at the side wall of the domain.

Since the capsules and HTF mass flow rate were assumed to be evenly distributed along the radial direction, a single capsule column may be considered as a representative case of the whole system. Consequently, the mass flow rate (f_m) that characterizes the inlet boundary condition in the simplified model is a fraction of the total mass flow rate in the bed, and is defined in Eqn. 28.

$$f_m = \frac{\dot{m}}{n_r} \tag{28}$$

where $\dot{m}$ is the total mass flow rate of the complete system and n_r is the number of capsules contained in a radial cross sectional view of the bed. In this context, two-dimensional axisymmetric flow conditions were assumed for the analysis. Figure 61 shows schematic of the system.

It consists of six, 1inch inner-diameter, spherical capsules vertically aligned along the symmetry line of the domain. The capsules are initially filled with solid $NaNO_3$ at a temperature $T_o = 286℃$. Uniform mass flow rate ($f_m = 3x10^{-4}kg/s$) and free stream temperature ($T_\infty = 326℃$) characterize the thermal boundary condition at the domain inlet, while the atmospheric pressure (P_o) was defined at the outlet surface. Teflon PTFE (Polytetrafluoroethylene) was selected as the shell material for all the capsules with 0.5mm thickness.

It should be pointed out that the velocity distribution of the HTF determines the convective component of the thermal energy transfer within the boundary layer at the outer surface of each capsule. Therefore, the nature of the flow has a significant effect on the external convective heat transfer rate. The ability to model the external convective energy transport is one of the key contributions of this model as compared to the previously reported models where the boundary condition at the outer shell surface is either a constant temperature or uniform heat flux.

5.3. Computational Details of Multi-Capsule Model

The numerical computations presented in this investigation were performed in commercially available software ANSYS/Fluent, using the finite volume approach to solve for the continuity, linear momentum and energy partial differential equations. The combined heat transfer problem, including the solid/liquid phase change was solved using the SIMPLE algorithm. A first order implicit discretization scheme was used for the transient terms while the convective and diffusive terms were discretized using a second order upwind scheme.

According to Eisfeld and Schnitzlein [117], the transition from laminar to turbulent flow regime in packed bed heat exchangers exists for the particle Reynolds number (Re_p) between 10 to 300.

$$Re_p = \frac{\rho \bar{v} d_p}{\eta} \tag{29}$$

where ρ and η are the fluid density and viscosity. $\bar{v}$ is the average superficial velocity of the HTF though the bed and d_p is the equivalent particle diameter, defined as the ratio between the bed volume and the total capsule surface area. The Reynolds number is written in terms of the mass flow rate.

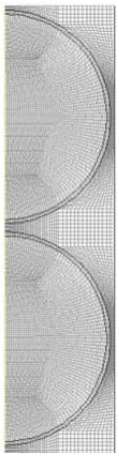

Figure 62 Grid distribution multi-ball model

$$Re_v = \left(\frac{4\dot{m}}{\pi\eta D_{tk}^2}\right)\frac{D_o}{6(1-\varepsilon)} \tag{30}$$

where D_{tk} is the diameter of the cylindrical container, ε the void fraction of the packed bed and D_o is the outer diameter of the capsule. For the flow conditions analyzed in this chapter, the Reynolds number was found to be in the range between 80 and 200. Therefore, in order to model the transitional flow of the HTF, the Reynolds-averaged Navier-Stokes (RANS) approach was used.

The realizable k-epsilon model proposed by [118] was employed while the enhanced wall treatment option was adopted. A second order upwind discretization scheme was used for the turbulent kinetic energy and dissipation rate. The PRESTO scheme was adopted for pressure correction via the continuity equation. The under relaxation factors for pressure, density, body forces, linear momentum, turbulent kinetic energy, turbulent dissipation rate, turbulent viscosity, liquid fraction update and energy were 0.3, 1.0, 1.0, 0.7, 0.8, 0.8,1.0, 0.9, and 1.0, respectively.

The solution of the problem was checked for convergence at each time step. Figure 62 shows the grid distribution for the first two capsules of the computational domain. The system was discretized in 30336 quadrilateral elements with maximum aspect ratio of 6.0. A finer near wall mesh capable of resolving the viscous sub-layer was implemented in the vicinity of the insulated and outer surface walls.

5.4. Validation of the Multi-Capsule Model

The numerical model was validated by the experimental results reported by [96]. A schematic of the experimental set up is presented in Figure 63. Atmospheric air at a volumetric flow rate of 110m^3/hr and 27℃ is forced to pass through a heated section by a centrifugal blower. The heated section consists of six electrical heaters that dissipate 36KW of heat and delivers hot air to the packed bed cylindrical section where 770 spherical capsules filled with Sodium Nitrate were randomly packed. Thermocouples were placed along the radial and axial directions of the test section. It should be pointed out that along the center line of the bed; thermocouples at four different bed heights (L/D=0.2, 0.4, 0.6 and 0.8 from bottom to top of the bed) were located inside the capsules. The temperature readings at two of those locations are presented in Figure 64.

The common stages that characterize the temperature history during melting are observed, e.g. solid phase sensible heating where the temperature increases with time followed by a sharp change in slope with and almost horizontal trend indicating phase change and the liquid phase sensible heating where temperature increases with time. The temperature history predicted by the numerical solution is also depicted in Figure 64. Reasonable agreement is observed.

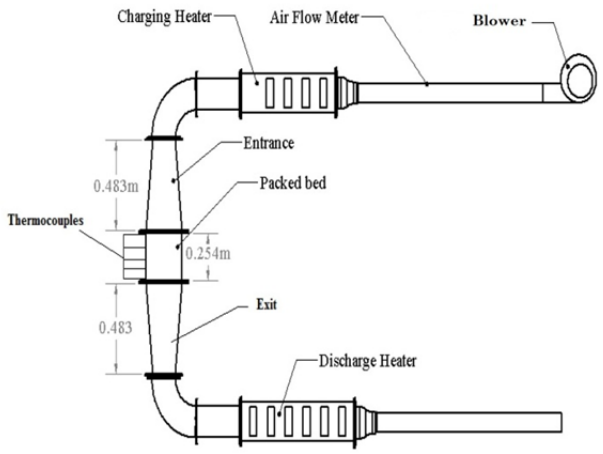

Figure 63 Schematic of the experimental set up. Taken from ref. [96]

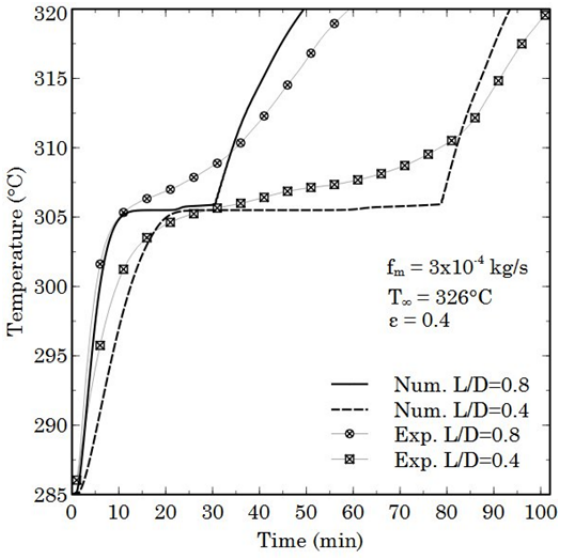

Figure 64 Comparison between numerical results and experimental measurements

5.5. Results and Discussion

The multi-capsule model was used to predict the melting dynamics of NaCl under different thermal conditions. Simultaneous conduction, natural convection and thermal radiation heat transfer were included in the model, and the influence of mass flow rate and inner surface emissivity on the melting rate is presented in Figures 65 and 66. Each figure also includes a secondary graph showing the effect of each parameter on the freezing time. A non-linear effect of both parameters on the melting time is observed with faster melting as the surface emissivity and inlet mass flow rate increase.

It is observed that, the melting time decreases 9.2%, 17% and 23% in the cases where the inner surface emissivity increases from 0.1 to 0.3, 0.6 and 1.0 respectively. On other hand, the melting time decreases 25%, 36% and 42% in the cases where the inlet mass flow rate increases from 0.0005kg/s to 0.001 kg/s, 0.0015 kg/s and 0.002 kg/s respectively. The emissive power at the inner surface as well as the convective heat transfer between the HTF and the capsule are responsible for this trend.

Figure 67 presents the evolution of the melting process. Each plot illustrates the temperature distribution on the left side and the streamline contours on the right side, for both the PCM and the air that is flowing outside the capsules. Also the solid fraction is depicted on the right hand side of each plot.

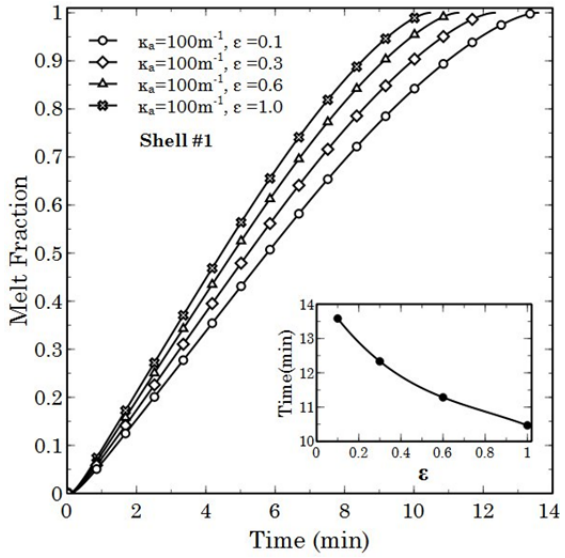

Figure 65 Influence of the absorption coefficient on the melt fraction rate

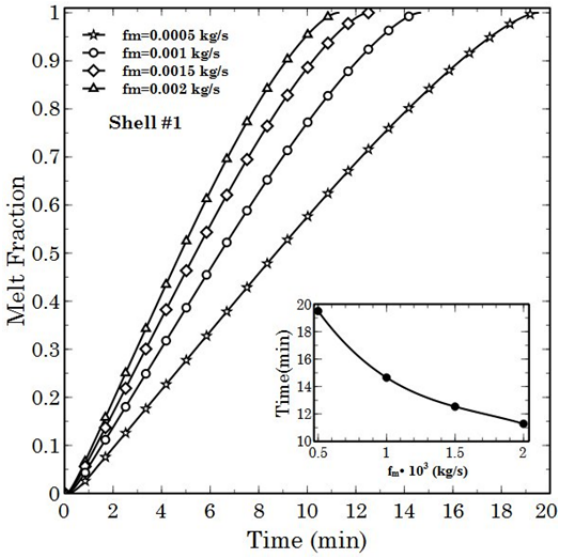

Figure 66 Influence of the mass flow rate on the melt fraction rate

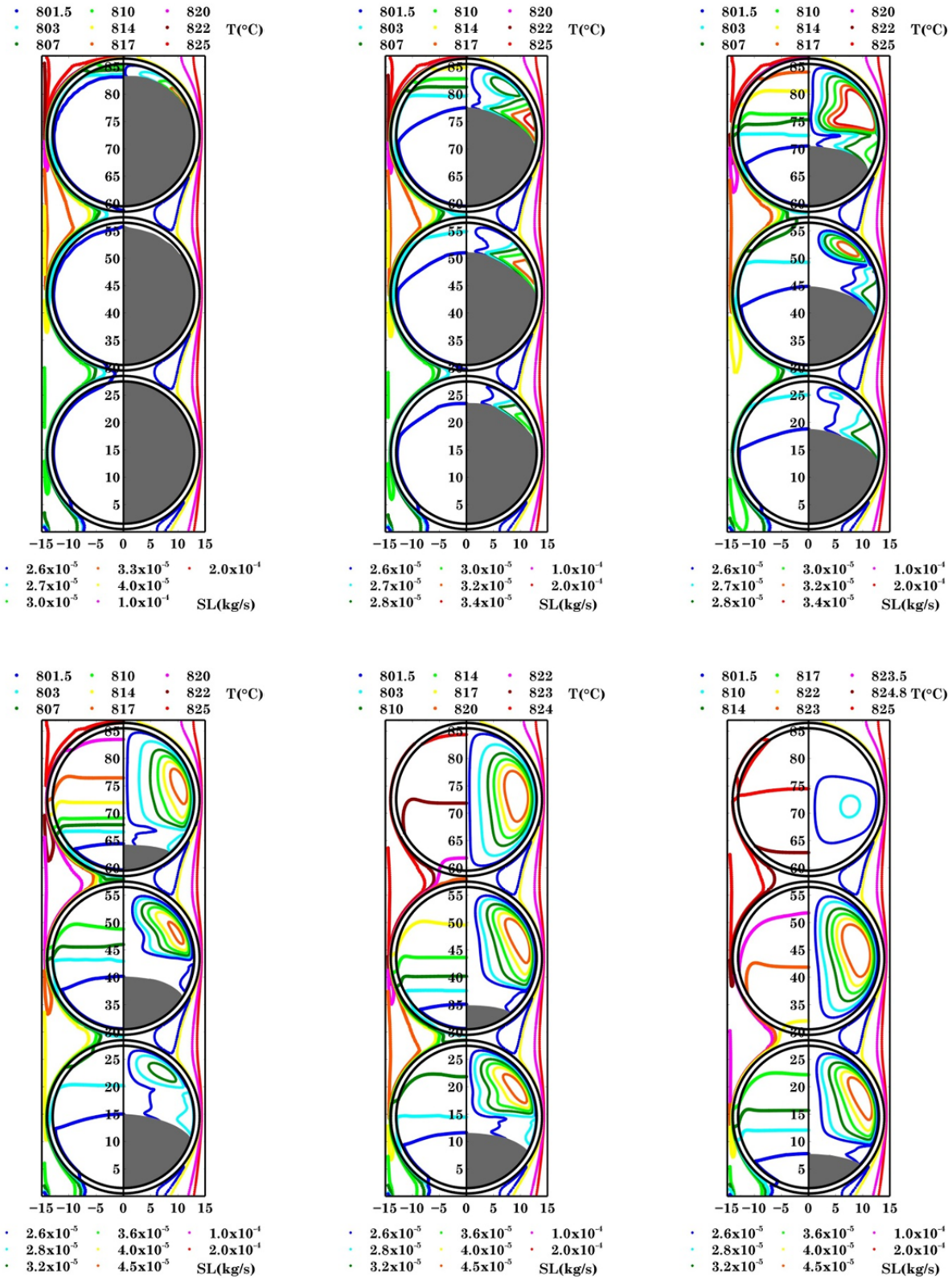

Figure 67 Evolution of the melting process for NaCl

CHAPTER 6: CONCLUSIONS AND RECOMMENDATIONS

6.1. Conclusions for Chapter 2

- It was found that the Grashof and the Stefan numbers strongly enhance the melt fraction rate of $NaNO_3$. For a fixed Grashof number ($2.6x10^4$), faster melting is achieved when the Stefan number is changed from 0.072 to 0.122. The melting time decreases 24.7% and 40.8% when the Stefan number increases from 0.072 to 0.097 and 0.122 respectively. Also, increasing the Grashof number from $2.69x10^4$ to $4.21x10^5$ for a fixed Stefan number enhances the melt fraction rate.
- A strong influence of the Prandtl number on the melt fraction rate was found under constant Grashof and Stefan numbers.
- It was found that when the shell material parameter (χ) is in the range of 0.966-0.994 there is no significant difference in the total time to complete melting, under the analyzed conditions. However a 34.1% increase in the melting time is observed for χ=0.67 as compared to the previous range.
- Under the analyzed thermal conditions, the sub-cooling parameter plays no significant role in the melting process for the analyzed conditions (1 to 15℃ below the PCM melting temperature).
- A counter-clockwise recirculating cell is formed in the top portion of the shell that causes a more intensive melting in the upper part of the solid phase. The location of the eye of the recirculation pattern was found to be dependent on the Grashof number and moves toward the inner surface of the shell as natural convection is intensified.

6.2. Conclusions for Chapter 3

- In the presence of all the fundamental heat transfer mechanisms, it was found that the contribution of thermal radiation on the solidification process of $NaNO_3$ is to reduce the solidification time by 17% as compared with the limiting case where thermal radiation has been intentionally neglected.
- The presence of natural convection induces the initial formation of an asymmetrical solid PCM layer from the bottom of the capsule. It is believed that this factor is responsible for the slight variation in the solid layer thickness along the shell symmetry line, with the smallest layer thickness at the top and the greatest layer thickness at the bottom.
- As the Biot number decreases from 5.0 to 1.0, the freezing time increases from 28.5 to 57.8min. However, a significantly smaller difference in the freezing times was observed when the Biot number decreases from 10 to 5.
- For a fixed thermal boundary condition, the solidification time decreases by 21.23% to 60.92% as R_i decreases from 35mm to 25mm and 15mm respectively.

6.3. Conclusions for Chapter 4

- The contribution of radiant energy exchange at the inner shell wall is one order of magnitude smaller than the convective transport process. This is valid for a NaCl with $\kappa_a = 100m^{-1}$ encapsulated in a spherical capsule with $R_i = 25mm$ and subjected to a constant temperature boundary condition at the outer surface, $T_w - T_m = 25℃$.
- For a fixed capsule size and temperature difference ΔT, the total heat transfer rate at the inner surface of the shell increases by increasing the medium optical thickness. It was found that, the presence of thermal radiation reduces the melting time by 10% as compared to the case with no radiation. However, a significant contribution of radiant heat transfer was found during the solid phase heating process, even for small optical thicknesses.

The time to reach 800.2℃ from 790.7℃ at the center point is 78.6% faster when $\kappa_a = 100\text{m}^{-1}$ as compared to the case with no radiation. No further improvements were obtained when the absorption coefficient increased from 100 to 200m^{-1}.

- For a fixed absorption coefficient and temperature difference ΔT, the increase of the capsule size significantly increases the melting time and radiant heat transfer at the inner surface of the shell. The melting time for the capsule with $R_i = 0.030\text{m}$ is 27.2% and 64.5% higher as compared to that for the shells with $R_i = 0.025\text{m}$ and $R_i = 0.020\text{m}$ respectively.
- The increase of the outer wall temperature significantly enhances the melting process. The melting time was 20% shorter for T_w-T_m=20°C and 33% shorter for T_w-T_m=25°C as compared to the corresponding value for T_w-T_m=15°C.

6.4. Conclusions for Chapter 5

- The melting time decreases by 9.2%, 17% and 23% when the inner surface emissivity increases from 0.1 to 0.3, 0.6 and 1.0 respectively.
- The melting time decreases by 25%, 36% and 42% as the inlet mass flow rate increases from 0.0005 kg/s to 0.001 kg/s, 0.0015 kg/s and 0.002 kg/s respectively.

6.5. Recommendations for Future Research

The following topics may be outlined as recommendations for future research.

- Modeling of thermal and pressure induced stresses in the shell for mechanical design of packed bed heat exchangers.
- Thermal modeling of different PCMs and capsule shapes, such us cylinders or rectangular containers. And the comparison with the results obtained for spherical shells.
- The influence of time and position dependent wall boundary conditions on melting and freezing dynamics.

REFERENCES

[1] A. L. Avila-Marin, J. Fernandez-Reche and F. M. Tellez, "Evaluation of the potential of central receiver solar power plants: Configuration, optimization and trends," *Applied Energy,* vol. 112, pp. 274-288, 2013.

[2] O. Behar, A. Khellaf and K. Mohammedi, "A review of studies on central receiver solar thermal power plants," *Renewable and sustainable energy reviews,* vol. 23, pp. 12-39, 2013.

[3] M. Medrano, A. Gil, I. Martorell, X. Potau and L. F. Cabeza, "State of the art on high-temperature thermal energy storage for power generation. Part 2-Case studies," *Renewable and Sustainable Energy Reviews,* vol. 14, pp. 56-72, 2010.

[4] U.S. Department of Energy, Energy Efficiency and Renewable Energy, "Sunshot VisionStudy," *U.S. DOE, Washington, DC, Report No. DOE/GO-102012-3037,* pp. 97-124, 2012.

[5] G. J. Kolb, C. K. Ho, T. R. Mancini and J. A. Gary, "Power tower technology roadmap and cost reduction plan," *Sandia National Laboratories, Livermore, CA, Technical Report No. SAND2011-2419,* 2011.

[6] J. Stekli, L. Irwin and R. Pitchumani, "Technical challenges and opportunities for concentrating solar power with thermal energy storage," *Journal of Thermal Science and Engineering Applications,* vol. 5, p. 021011, 2013.

[7] K. Nithyanandam and R. Pitchumani, "Cost and performance analysis of concentrating solar power systems with integrated latent thermal energy storage," *Energy,* vol. 64, pp. 793-810, 2014.

[8] J. E. Pacheco, S. K. Showalter and W. J. Kolb, "Development of a molten-salt thermocline thermal storage system for parabolic trough plants," *Journal of Solar Energy Engineering,* vol. 124, pp. 153-159, 2002.

[9] Electric Power Research Institute (EPRI), "Solar thermocline storage systems: Preliminary Design Study," *Electric Power Research Institute, Palo Alto, CA, Report No. 1019581,* 2010.

[10] Z. Yang and S. V. Garimella, "Molten-salt thermal energy storage in thermoclines under different environmental boundary conditions," *Applied Energy,* vol. 87, pp. 3322-3329, 2010.

[11] S. Kuravi, J. Trahan, D. Y. Goswami, M. M. Rahman and E. K. Stefanakos, "Thermal energy storage technologies and systems for concentrating solar power plants," *Progress in Energy and Combustion Science,* vol. 39, pp. 285-319, 2013.

[12] M. Liu, W. Saman and F. Bruno, "Review on storage materials and thermal performance enhancement techniques for high temperature phase change thermal storage systems," *Renewable and Sustainable Energy Reviews,* vol. 16, pp. 2118-2132, 2012.

[13] L. F. Cabeza, C. Sole, A. Castell, E. Oro and A. Gil, "Review of solar thermal storage techniques and associated heat transfer technologies," *Proceedings of the IEEE,* vol. 100, pp. 525-538, 2012.

[14] Y. Dutil, D. R. Rousse, N. B. Salah, S. Lassue and L. Zalewski, "A review on phase-change materials: mathematical modeling and simulations," *Renewable and Sustainable Energy Reviews,* vol. 15, pp. 112-130, 2011.

[15] A. Gil, M. Medrano, I. Martorell, A. Lazaro, P. Dolado, B. Zalba and L. F. Cabeza, "State of the art on high temperature thermal energy storage for power generation. Part 1- Concepts, materials and modellization," *Renewable and Sustainable Energy Reviews,* vol. 14, pp. 31-55, 2010.

[16] K. Nithyanandam, R. Pitchumani and A. Mathur, "Analysis of a latent thermocline storage system with encapsulated phase change materials for concentrating solar power," *Applied Energy,* vol. 113, pp. 1446-1460, 2014.

[17] A. Felix Regin, S. Solanki and J. Saini, "An analysis of a packed bed latent heat thermal energy storage system using PCM capsules: Numerical investigation," *Renewable Energy,* vol. 34, pp. 1765-1773, 2009.

[18] N. Wakao and T. Funazkri, "Effect of fluid dispersion coefficients on particle-to-fluid mass transfer coefficients in packed beds: correlation of Sherwood numbers," *Chemical Engineering Science,* vol. 33, pp. 1375-1384, 1978.

[19] J. Beek, "Design of packed catalytic reactors," *Advances in Chemical Engineering,* vol. 3, pp. 203-271, 1962.

[20] S. Paterson, "Propagation of a boundary of fusion," *Proceedings of the Glasgow Mathematical Association,* vol. 1, no. 1, pp. 42-47, 1952.

[21] P. B. Grimado and B. A. Boley, "A numerical solution for the symmetric melting of spheres," *International Journal for Numerical Methods in Engineering,* vol. 2, pp. 175-188, 1970.

[22] F. Moore and Y. Bayazitoglu, "Melting within a spherical enclosure," *Journal of Heat Transfer,* vol. 104, pp. 19-23, 1982.

[23] S. K. Roy and S. Sengupta, "Gravity-assisted melting in a spherical enclosure: effects of natural convection," *International Journal of Heat and Mass Transfer,* vol. 33, pp. 1135-1147, 1990.

[24] P. A. Bahrami, "Natural melting within a spherical shell," *NASA, Ames Research Center, Technical Memorandum 102822,* pp. 1-22, June 1990.

[25] S. Fomin and T. Saitoh, "Melting of unfixed material in spherical capsule with non-isothermal wall," *International journal of heat and mass transfer,* vol. 42, pp. 4197-4205, 1999.

[26] M. Bareiss and H. Beer, "An analytical solution of the heat transfer process during melting of an unfixed solid phase change material inside a horizontal tube," *International Journal of Heat and Mass Transfer,* vol. 27, pp. 739-746, 1984.

[27] J. Khodadadi and Y. Zhang, "Effects of buoyancy-driven convection on melting within spherical containers," *International Journal of Heat and Mass Transfer,* vol. 44, pp. 1605-1618, 2001.

[28] A. Regin, S. Solanki and J. Saini, "Experimental and numerical analysis of melting of PCM inside a spherical capsule," in *Proceedings of the 9th AIAA/ASME Joint Thermophysics and Heat Transfer Conference*, San Francisco, California, June 5-8, 2006.

[29] E. Assis, L. Katsman, G. Ziskind and R. Letan, "Numerical and experimental study of melting in a spherical shell," *International Journal of Heat and Mass Transfer,* vol. 50, pp. 1790-1804, 2007.

[30] F. Tan, "Constrained and unconstrained melting inside a sphere," *International Communications in Heat and Mass Transfer,* vol. 35, pp. 466-475, 2008.

[31] F. Tan, S. Hosseinizadeh, J. Khodadadi and L. Fan, "Experimental and computational study of constrained melting of phase change materials (PCM) inside a spherical capsule," *International Journal of Heat and Mass Transfer,* vol. 52, pp. 3464-3472, 2009.

[32] S. Hosseinizadeh, A. Darzi and F. Tan, "Numerical investigations of unconstrained melting of nano-enhanced phase change material (NEPCM) inside a spherical container," *International Journal of Thermal Sciences,* vol. 51, pp. 77-83, 2012.

[33] W. Zhao, A. F. Elmozughi, A. Oztekin and S. Neti, "Heat transfer analysis of encapsulated phase change material for thermal energy storage," *International Journal of Heat and Mass Transfer,* vol. 63, pp. 323-335, 2013.

[34] T. S. Saitoh, H. Hoshina and K. Yamada, "Theoretical analysis and experiment on combined close-contact and natural convection melting in thermal energy storage spherical capsule," in *Proceedings of the IEEE Energy Conversion Engineering Conference*, Honolulu, HI, Jul 27 - Aug1, 1997.

[35] T. S. Saitoh, H. Kato and H. Hoshina, "Theoretical analysis for combined close-contact and natural convection melting in ice storage spherical capsule," in *Proceedings of the IEEE Energy Conversion Engineering Conference*, Washington, DC, Aug 11-16, 1996.

[36] S. Hosseinizadeh, A. Rabienataj Darzi, F. Tan and J. Khodadadi, "Unconstrained melting inside a sphere," *International Journal of Thermal Sciences,* vol. 63, pp. 55-64, 2013.

[37] M. Rizan, F. Tan and C. Tso, "An experimental study of n-octadecane melting inside a sphere subjected to constant heat rate at surface," *International Communications in Heat and Mass Transfer,* vol. 39, pp. 1624-1630, 2012.

[38] S. Wang, A. Faghri and T. L. Bergman, "A comprehensive numerical model for melting with natural convection," *International Journal of Heat and Mass Transfer,* vol. 53, pp. 1986-2000, 2010.

[39] H. Shabgard, T. Bergman, N. Sharifi and A. Faghri, "High temperature latent heat thermal energy storage using heat pipes," *International Journal of Heat and Mass Transfer,* vol. 53, pp. 2979-2988, 2010.

[40] J. Dumore, H. Merk and J. Prins, "Heat transfer from water to ice by thermal convection," *Nature,* vol. 172, pp. 460-461, 1953.

[41] C. R. Vanier and C. Tien, "Free convection melting of ice spheres," *AIChE Journal,* vol. 16, pp. 76-82, 1970.

[42] Y. Hao and Y.-X. Tao, "Heat transfer characteristics of melting ice spheres under forced and mixed convection," *Journal of heat transfer,* vol. 124, pp. 891-903, 2002.

[43] P. Konakov, "On the regularities of composite heat transfer," *International Journal of Heat and Mass Transfer,* vol. 2, pp. 136-149, 1961.

[44] E. Sparrow, C. Usiskin and H. Hubbard, "Radiation heat transfer in a spherical enclosure containing a participating, heat-generating gas," *Journal of Heat Transfer,* vol. 83, pp. 199-206, 1961.

[45] E. A. Dennar and M. Sibulkin, "An Evaluation of the differential approximation for spherically symmetric radiative transfer," *Journal of Heat Transfer,* vol. 91, pp. 73-76, 1969.

[46] Y. Chou and C. Tien, "A modified moment method for radiative transfer in non-planar systems," *Journal of Quantitative Spectroscopy and Radiative Transfer,* vol. 8, pp. 919-933, 1968.

[47] T. W. Tong and P. S. Swathi, "Radiative heat transfer in emitting-absorbing-scattering spherical media," *Journal of Thermophysics and Heat Transfer,* vol. 1, pp. 162-170, 1987.

[48] I. L. Ryhming, "Radiative transfer between two concentric spheres separated by an absorbing and emitting gas," *International Journal of Heat and Mass Transfer,* vol. 9, pp. 315-324, 1966.

[49] R. Viskanta and A. Crosbie, "Radiative transfer through a spherical shell of an absorbing-emitting gray medium," *Journal of Quantitative Spectroscopy and Radiative Transfer,* vol. 7, pp. 871-889, 1967.

[50] G. Jia, Y. Yener and J. Cipolla Jr, "Radiation between two concentric spheres separated by a participating medium," *Journal of Quantitative Spectroscopy and Radiative Transfer,* vol. 46, pp. 11-19, 1991.

[51] R. Viskanta and R. Merriam, "Heat transfer by combined conduction and radiation between concentric spheres separated by radiating medium," *Journal of Heat Transfer,* vol. 90, pp. 248-256, 1968.

[52] H.-S. Chu and L.-C. Weng, "Transient combined conduction and radiation in anisotropically scattering spherical media," *Journal of thermophysics and heat transfer,* vol. 6, pp. 553-556, 1992.

[53] R. Viskanta and P. Lall, "Transient cooling of a spherical mass of high-temperature gas by thermal radiation," *Journal of Applied Mechanics,* vol. 32, pp. 740-746, 1965.

[54] S. Thynell and M. Özisik, "Radiation transfer in an isotropically scattering homogeneous solid sphere," *Journal of Quantitative Spectroscopy and Radiative Transfer,* vol. 33, pp. 319-330, 1985.

[55] J. Tsai and M. Özisik, "Transient, combined conduction and radiation in an absorbing, emitting, and isotropically scattering solid sphere," *Journal of Quantitative Spectroscopy and Radiative Transfer,* vol. 38, pp. 243-251, 1987.

[56] C. Siewert and J. Thomas, "On coupled conductive-radiative heat transfer problems in a cylinder," *Journal of Quantitative Spectroscopy and Radiative Transfer,* vol. 48, pp. 227-236, 1992.

[57] Y. Bayazitoglu and P. Suryanarayana, "Transient radiative heat transfer from a sphere surrounded by a participating medium," *ASME Transactions Journal of Heat Transfer,* vol. 111, pp. 713-718, 1989.

[58] S. Thynell, "Interaction of conduction and radiation in anisotropically scattering, spherical media," *Journal of thermophysics and heat transfer,* vol. 4, pp. 299-304, 1990.

[59] M. Abrams and R. Viskanta, "The effects of radiative heat transfer upon the melting and solidification of semitransparent crystals," *Journal of Heat Transfer,* vol. 96, pp. 184-190, 1974.

[60] R. Raj, A. Prasad, P. R. Parida and S. C. Mishra, "Analysis of solidification of a semitransparent planar layer using the lattice Boltzmann method and the discrete transfer method," *Numerical Heat Transfer, Part A: Applications,* vol. 49, pp. 279-299, 2006.

[61] P. Lapka and P. Furmanski, "Numerical modelling of solidification processes of semitransparent materials using the enthalpy and the finite volume methods," *Heat and Mass Transfer,* vol. 44, pp. 937-957, 2008.

[62] E. Sparrow and J. Broadbent, "Freezing in a vertical tube," *Journal of Heat Transfer,* vol. 105, pp. 217-225, 1983.

[63] A. R. Archibold, M. M. Rahman, D. Y. Goswami and E. K. Stefanakos, "Numerical solution of heat transfer during solidification of an encapsulated phase change material," in *Proceedings of the ASME 2013 International Mechanical Engineering Congress & Exposition*, Nov. 15-21, San Diego, CA, 2013.

[64] S. H. Cho and J. E. Sunderland, "Phase change of spherical bodies," *International Journal of Heat and Mass Transfer,* vol. 13, pp. 1231-1233, 1970.

[65] Y.-P. Shih and T.-C. Chou, "Analytical solutions for freezing a saturated liquid inside or outside spheres," *Chemical Engineering Science,* vol. 26, pp. 1787-1793, 1971.

[66] R. Pedroso and G. Domoto, "Inward spherical solidification- solution by the method of strained coordinates," *International Journal of Heat and Mass Transfer,* vol. 16, pp. 1037-1043, 1973.

[67] D. Riley, F. Smith and G. Poots, "The inward solidification of spheres and circular cylinders," *International Journal of Heat and Mass Transfer,* vol. 17, pp. 1507-1516, 1974.

[68] K. Stewartson and R. Waechter, "On Stefans problem for spheres," *Proceedings of the Royal Society of London. A. Mathematical and Physical Sciences,* vol. 348, pp. 415-426, 1976.

[69] A. Soward, "A unified approach to Stefans problem for spheres and cylinders," *Proceedings of the Royal Society of London. A. Mathematical and Physical Sciences,* vol. 373, pp. 131-147, 1980.

[70] J. M. Hill and A. Kucera, "Freezing a saturated liquid inside a sphere," *International journal of heat and mass transfer,* vol. 26, pp. 1631-1637, 1983.

[71] M. Prud'homme, D. L. Nguyen and T. H. Nguyen, "A heat transfer analysis for solidification of slabs, cylinders, and spheres," *Journal of Heat Transfer,* vol. 111, pp. 699-705, 1989.

[72] L. C. Tao, "Generalized numerical solutions of freezing a saturated liquid in cylinders and spheres," *AIChE Journal,* vol. 13, pp. 165-169, 1967.

[73] E. Sparrow and J. Broadbent, "Freezing in a vertical tube," *Journal of Heat Transfer,* vol. 105, pp. 217-225, 1983.

[74] E. Sparrow and Y. Ohkubo, "Numerical predictions of freezing in a vertical tube," *Numerical Heat Transfer, Part A: Applications,* vol. 9, pp. 79-95, 1986.

[75] S. W. McCue, B. Wu and J. M. Hill, "Classical two-phase Stefan problem for spheres," *Proceedings of the Royal Society A: Mathematical, Physical and Engineering Science,* vol. 464, pp. 2055-2076, 2008.

[76] K. Ismail and J. Henríquez, "Solidification of PCM inside a spherical capsule," *Energy conversion and management,* vol. 41, pp. 173-187, 2000.

[77] C. Chan and F. Tan, "Solidification inside a sphere-an experimental study," *International communications in heat and mass transfer,* vol. 33, pp. 335-341, 2006.

[78] A. Regin, S. Solanki and J. Saini, "Solidification of phase change material inside a cylindrical capsule," in *Proceedings of 18th National and 7th ISHMT-ASME Heat and Mass Transfer Conference*, Guwahati, India, 2006.

[79] E. Assis, G. Ziskind and R. Letan, "Numerical and experimental study of solidification in a spherical shell," *Journal of Heat Transfer,* vol. 131, p. 024502, 2009.

[80] J. Yang and C. Zhao, "Solidification analysis of a single particle with encapsulated phase change materials," *Applied Thermal Engineering,* vol. 51, pp. 338-346, 2013.

[81] S. Chan, D. Cho and G. Kocamustafaogullari, "Melting and solidification with internal radiative transfer-a generalized phase change model," *International Journal of Heat and Mass Transfer,* vol. 26, pp. 621-633, 1983.

[82] S. Chan and K. Hsu, "The mushy zone in a phase change model of a semitransparent material with internal radiative transfer," *Journal of heat transfer,* vol. 110, pp. 260-263, 1988.

[83] C. Yao, B. Chung and G.-X. Wang, "Mushy zone equilibrium solidification of a semitransparent layer subject to radiative and convective cooling," *International journal of heat and mass transfer,* vol. 45, pp. 2397-2405, 2002.

[84] H.-L. Yi, C.-H. Wang, H.-P. Tan and Y. Zhou, "Radiative heat transfer in semitransparent solidifying slab considering space-time dependent refractive index," *International Journal of Heat and Mass Transfer,* vol. 55, pp. 1724-1731, 2012.

[85] J. Miranda Fuentes, K. Johannes, F. Kuznik, M. Cosnier and J. Virgone, "Melting with convection and radiation in a participating phase change material," *Applied Energy,* vol. 109, pp. 454-461, 2013.

[86] B. Webb and R. Viskanta, "Radiation-induced melting with buoyancy effects in the Liquid," *Experimental Heat Transfer An International Journal,* vol. 1, pp. 109-126, 1987.

[87] Y. Touloukian, R. Kirby, E. Taylor and T. Lee, "Thermophysical Properties of Matter-the TPRC Data Series. Volume 13. Thermal Expansion-Nonmetallic Solids," 1977.

[88] C. Lan and S. Kou, "Effects of rotation on heat transfer, fluid flow and interfaces in normal gravity floating-zone crystal growth," *Journal of crystal growth,* vol. 114, no. 4, pp. 517-535, 1991.

[89] G. J. Janz, C. B. Allen, N. P. Bansal, R. M. Murphy and R. P. T. Tomkins, "Physical properties data compilations relevant to energy storage, 2. Molten salts: Data on single and multi-component salt systems," National Bureau of Standars, Department of Commerce. Report No. NSRDS-NBS 61, Part II, Washington, DC, 1979.

[90] T. Bauer, D. Laing and R. Tamme, "Characterization of sodium nitrate as phase change material," *International Journal of Thermophysics,* vol. 33, no. 1, pp. 191-104, 2012.

[91] L. R. White and H. T. Davis, "Thermal conductivity of molten alkali nitrates," *The Journal of Chemical Physics,* vol. 47, no. 12, pp. 5433-5439, 1967.

[92] V. R. Voller and C. Prakash, "A fixed grid numerical modelling methodology for convection-diffusion mushy region phase-change problems," *International Journal of Heat and Mass Transfer,* vol. 30, no. 8, pp. 1709-1719, 1987.

[93] A. D. Brent, V. R. Voller and K. T. J. Reid, "Enthalpy-Porosity technique for modeling convection-diffusion phase change: Application to the melting of a pure metal," *Numerical Heat Transfer, Part A Applications,* vol. 13, no. 3, pp. 297-318, 1988.

[94] S. V. Patankar, Numerical heat transfer and fluid flow, Taylor & Francis Group, 1980.

[95] E. Sparrow, S. Patankar and S. Ramadhyani, "Analysis of melting in the presence of natural convection in the melt region," *Journal of Heat Transfer,* vol. 99, pp. 520-526, 1977.

[96] T. Alam, J. Dhau, D. Goswami, M. Rahman and E. Stefanakos, "Experimental investigation of a packed-bed latent heat thermal storage system with encapsulated phase change material," in *Proceedings of the ASME 2014 International Mechanical Engineering Congress & Exposition*, Nov. 14-20, Montreal, Canada, 2014.

[97] C. J. Ho and R. Viskanta, "Heat transfer during inward melting in a horizontal tube," *International journal of heat and mass transfer,* vol. 27, no. 5, pp. 705-716, 1984.

[98] B. J. Jones, D. Sun, S. Krishnan and S. V. Garimella, "Experimental and numerical study of melting in a cylinder," *International Journal of Heat and Mass Transfer,* vol. 49, pp. 2724-2738, 2006.

[99] M. Chow and R. Akins, "Pseudosteady-state natural convection inside spheres," *Journal of Heat Transfer,* vol. 97, pp. 54-59, 1975.

[100] J. Hutchins and E. Marschall, "Pseudosteady-state natural convection heat transfer inside spheres," *International journal of heat and mass transfer,* vol. 32, no. 11, pp. 2047-2053, 1989.

[101] A. Ramdas, "The infra-red absorption spectra of sodium nitrate and calcite," in *Proceedings of the Indian Academy of Sciences, Vol. XXXVIII, No. 3, Sec. A*, 1953.

[102] S. Chandrasekhar, Radiative transfer, New York: Dover Publications, 1960.

[103] R. Viskanta and M. Mengüc, "Radiation heat transfer in combustion systems," *Progress in Energy and Combustion Science,* vol. 13, pp. 97-160, 1987.

[104] W. Fiveland, "Discrete-ordinates solutions of the radiative transport equation for rectangular enclosures," *ASME Transactions Journal of Heat Transfer,* vol. 106, pp. 699-706, 1984.

[105] K. Sen and S. J. Wilson, Radiative Transfer in Curved Media: Basic and Mathematical Methods for Radiative Transfer and Transport Problems in Participating Media of Spherical and Cylindrical Geometry, World Scientific, 1990.

[106] R. Siegel and J. Howell, Thermal radiation heat transfer, Taylor & Francis Group, 2002.

[107] P. Parida, R. Raj, A. Prasad and S. Mishra, "Solidification of a semitransparent planar layer subjected to radiative and convective cooling," *Journal of Quantitative Spectroscopy and Radiative Transfer,* vol. 107, pp. 226-235, 2007.

[108] P. Myers, D. Y. Goswami and E. K. Stefanakos, "Molten salt spectroscopy for quantification of radiative absorption in novel metal chloride-enhanced thermal storage media," in *Proceedings of the ASME 2014 International Mechanical Engineering Congress & Exposition*, Nov. 14-20, Montreal, Canada, 2014.

[109] Y. Touloukian and D. DeWitt, "Thermophysical properties of matter-The TPRC data series. Volume 8. Thermal radiative properties-nonmetallic solids.," 1972.

[110] H. Bloom and B. Peryer, "Molten salts mixtures. 8. Refractive index of molten salt mixtures and their molar refractivities," *Australian Journal of Chemistry,* vol. 18, pp. 777-778, 1965.

[111] K. Sen and S. J. Wilson, Radiative transfer in curved media: basic and mathematical methods for radiative transfer and transport problems in participating media of spherical and cylindrical geometry, World Scientific, 1990.

[112] A. R. Archibold, A. Bhardwaj, M. M. Rahman, D. Y. Goswami and E. L. Stefanakos, "Thermal assessment of a latent leat energy storage module using a high temperature phase change material with enhanced radiative properties," in *Proceedings of the ASME 2014 International Mechanical Engineering Congress & Exposition*, Nov. 14-20, Montreal, Canada, 2014.

[113] H. Peng, H. Dong and X. Ling, "Thermal investigation of PCM-based high temperature thermal energy storage in packed bed," *Energy Conversion and Management,* vol. 81, pp. 420-427, 2014.

[114] N. A. M. Amin, M. Belusko and F. Bruno, "An effectiveness-NTU model of a packed bed PCM thermal storage system," *Applied Energy,* vol. 134, pp. 356-362, 2014.

[115] S. Bellan, J. Gonzalez-Aguilar, M. Romero, M. M. Rahman, D. Yogi Goswami, E. K. Stefanakos and D. Couling, "Numerical analysis of charging and discharging performance of a thermal energy storage system with encapsulated phase change material," *Applied Thermal Engineering,* vol. 71, no. 1, pp. 481-500, 2014.

[116] A. Regin, S. Solanki and J. Saini, "An analysis of a packed bed latent heat thermal energy storage system using PCM capsules: Numerical investigation," *Renewable Energy,* vol. 34, no. 7, pp. 1765-1773, 2009.

[117] B. Eisfeld and Schnitzlein, "The influence of confining walls on the pressure drop in packed beds," *Chemical Engineering Science,* vol. 56, pp. 4321-4329, 2001.

[118] T.-H. Shih, W. Liou, A. Shabbir, Z. Yang and J. Zhu, "A new k-epsilon eddy viscosity model for high Reynolds number turbulent flows: Model development and validation," *Computers and Fluids,* vol. 24, pp. 227-238, 1995.

APPENDICES

Appendix A: List of Symbols

c_p	specific heat at constant pressure (J/kg K)
ΔT	temperature difference (°C) $(T_w - T_m)$
Fo	Fourier number $(\kappa/\rho\ c_p)(t/R_i^2)$
g	gravitational acceleration (m/s^2)
Gr_R	Grashof number $(g\beta\Delta T R_i^3 \rho^2/\eta^2)$
$\hbar$	heat transfer coefficient $(W/m^2\ K)$ $(\hbar = q_t/A\Delta T)$
h	sensible enthalpy (J/kg)
h_∞	external heat transfer coefficient $(W/m^2\ K)$
L	latent heat of fusion (J/kg)
n	index of refraction
Nu	Nusselt number $(q_{cd} + q_{cv})R_i/\kappa(T_m - T_\infty)$
P	pressure (Pa)
Pl	Planck number $\kappa(\kappa_a + \sigma_s)/4n\sigma\bar{T}^3$
Pr	Prandtl number of the fluid ($\eta c_p/k$)
q_t	total heat transfer rate at the inner shell wall (W)
q_{cd}	conductive heat flux at the inner shell wall (W/m^2)
q_{cv}	convective heat flux at the inner shell wall (W/m^2)
q_r	radiative heat flux at the inner shell wall (W/m^2)
R_i	inner radius of the capsule (m)
Ra	Rayleigh number (GrPr)
Ste_L	liquid phase Stefan number $(c_{p_L}(T_o - T_m)/L)$
Ste_s	solid phase Stefan number $(c_{p_s}(T_m - T_\infty)/L)$
t	time (s)
T	temperature (°C)
$\bar{T}$	reference temperature (°C) $(T_w + T_m/2)$
T_∞	free stream temperature (°C)
υ	velocity (m/s)

Greek Symbols

α	thermal diffusivity (m^2/s)
β	thermal expansion coefficient (1/K)
χ	shell material parameter $(1 - \kappa_{pcm}/\kappa_{shell})$
δ	shell wall thickness (m)
η	dynamic viscosity (kg/m s)
κ	thermal conductivity (W/m K)
κ_a	absorption coefficient (m^{-1})
λ	latent heat (J/kg)
Θ_n	dimensionless temperature at the center point, $\Theta_n = (T - T_o)/(T_w - T_o)$
Θ	dimensionless temperature $(T - T_i)/(T_w - T_i)$
ρ	density (kg/m^3)
σ	Stefan-Boltzmann constant, $\sigma = 5.67x10^{-8}\ W/m^2K^4$
σ_s	scattering coefficient (m^{-1})
τ	optical thickness, $\tau = (\kappa_a + \sigma_s)R_i$

φ dimensionless irradiation
ξ dimensionless stream line value
ω scattering albedo, $\omega = \sigma_s/(\kappa_a + \sigma_s)$

Subscripts

m melting
o initial
r radial direction
s solid
w wall
θ angular direction
Ψ dimensionless radiative flux at the inner shell wall $q_r/\sigma(T_m^4 - T_\infty^4)$

Appendix B: Copyright Permission

The information below is Copyright permission to reuse Elsevier published material in Chapters 2, 3 and 4, respectively. The information was taken from:

http://www.elsevier.com/journal-authors/author-rights-and-responsibilities#author-use

Author Rights

Elsevier supports the need for authors to share, disseminate and maximize the impact of their research. We take our responsibility as stewards of the online record seriously, and work to ensure our policies and procedures help to protect the integrity of scholarly works.

Author's rights to reuse and post their own articles published by Elsevier are defined by Elsevier's copyright policy. For our proprietary titles, the type of copyright agreement used depends on the author's choice of publication:

For subscription articles: These rights are determined by a copyright transfer, where authors retain scholarly rights to post and use their articles.

For open access articles: These rights are determined by an exclusive license agreement, which applies to all our open access content.

In both cases, the fundamental rights needed to publish and distribute an article remain the same and Elsevier authors will be able to use their articles for a wide range of scholarly purposes.

Details on how authors can reuse and post their own articles are provided below.

Help and support
For reuse and posting not detailed below, please see our posting policy, or for authors who would like to:

- Include material from other sources in your work being published by Elsevier, please visit: Permission seeking guidelines for Elsevier authors.
- Obtain permission to re-use material from Elsevier books, journals, databases, or other products, please visit: Obtaining permission to reuse Elsevier material
- Or if you are an Elsevier author and are contacted by a requestor who wishes to re-use all or part of your article or chapter, please also refer them to our Obtaining Permission to Re-Use Elsevier Material page.
- See our FAQ on posting and copyright queries.
- Contact us directly, please email our Permissions Help Desk.

Definitions | Author Posting | Author Use

How authors can use their own journal articles

Authors can use their articles for a wide range of scholarly, non-commercial purposes as outlined below. These rights apply for all Elsevier authors who publish their article as either a subscription article or an open access article.

We require that all Elsevier authors always include a full acknowledgement and, if appropriate, a link to the final published version hosted on Science Direct.

For open access articles these rights are separate from how readers can reuse your article as defined by the author's choice of Creative Commons user license options.

Authors can use either their accepted author manuscript or final published article for:	
✓	Use at a conference, meeting or for teaching purposes
✓	Internal training by their company
✓	Sharing individual articles with colleagues for their research use* (also known as 'scholarly sharing')
✓	Use in a subsequent compilation of the author's works
✓	Inclusion in a thesis or dissertation
✓	Reuse of portions or extracts from the article in other works
✓	Preparation of derivative works (other than for commercial purposes)

*Please note this excludes any systematic or organized distribution of published articles.

ABOUT THE AUTHOR

Antonio Ramos was born in Barranquilla, Colombia on November 15, 1979. After completion of the military service, in December 1997, he enrolled as a full time student at Universidad del Norte. He received his bachelor's degree in 2003 and completed his master's program in 2005 at the same institution. In the fall of 2010, he joined the Clean Energy Research Center at the University of South Florida and started his doctoral program in Mechanical Engineering.

Antonio Ramos and Milena Perez were married April 2, 2004 in Barranquilla, Colombia. They have three daughters, Paula, Mary and Natalia.